Quadrupole Moments of Strongly Deformed Shapes in ^{154}Er

Thesis submitted in accordance with the requirements of The University of Liverpool for the degree of Doctor in Philosophy by

John Peter Revill

24th January 2013

UNIVERSITY OF
LIVERPOOL

Abstract

The quadrupole moments of strongly deformed, ultrahigh-spin bands in the nucleus ^{154}Er have been measured for the first time, providing a calibration for recent measurements made for similar bands in ^{157}Er and ^{158}Er using the same method.

High-spin states up to ~ 52 $\hbar$ have been populated using the fusion-evaporation reaction ^{110}Pd(^{48}Ti,4nγ)^{154}Er at a beam energy of 215 MeV, in an experiment performed at the ATLAS facility at Argonne National Laboratory, USA, using the Gammasphere detector array.

Two new ultrahigh-spin bands, believed to be triaxially deformed, have been observed in ^{154}Er in addition to the known triaxial strongly deformed (TSD) band and superdeformed (SD) axially symmetric prolate band. The quadrupole moments, Q_t, of three of these bands have been measured using the Doppler-shift attenuation method (DSAM), with values of 11.0 ± 0.6 eb for the known TSD band, 19.5 ± 1.5 eb for the SD band and 10.0 ± 0.9 eb for one of the new bands.

Cranked Nilsson-Strutinsky (CNS) calculations are compared with results and possible nucleon configurations are discussed. A configuration similar to that of the yrast SD band of the isotone ^{152}Dy is assigned to the ^{154}Er SD band. Based on their Q_t, the triaxial bands appear more consistent with configurations corresponding to a TSD shape with a negative γ deformation parameter. The Q_t of ~ 11 eb is consistent with previous results for the four TSD bands in ^{157,158}Er. These results challenge theoretical calculations that predict positive-γ TSD shapes to be energetically favoured over negative-γ shapes.

Whence and what art thou, execrable shape …?

—Milton, *Paradise Lost*, Book ii

Contents

List of Figures

List of Tables

Acknowledgements

I am indebted to my supervisors Eddie Paul and Paul Nolan, Xiaofeng Wang and Mark Riley at Florida State University, John Simpson at STFC Daresbury, the staff at Argonne National Laboratory, Ingemar Ragnarsson at Lund for his invaluable theoretical input, and all the members of our collaboration.

Thank you to the members of the Nuclear Structure group at the University of Liverpool, in whose company it has been a pleasure to work and with whom I have had many enlightening discussions (not always about nuclear physics).

Thank you to my family and friends.

Finally, I am very grateful to the STFC for funding my postgraduate research studentship.

Chapter 1

Introduction

This thesis describes the measurement of physical properties of the nucleus erbium-154 (^{154}Er). These properties are, more specifically, those of the nucleus when it adopts certain strongly deformed shapes that occur (with only a very low probability) when it is given a large amount of angular momentum (spin).

Strongly deformed nuclei are a well-established phenomenon. They were first observed in the 1960s in actinide nuclei at low spin [1] and were later predicted to occur in the lighter $A \sim 150$ region at high spin. This was confirmed in 1984 by Nyakó et al. with the observation of an experimental signal consistent with a strongly deformed shape in ^{152}Dy [2]. Since then, dozens of nuclei with these *superdeformed* (SD) states have been observed. The term 'superdeformed' refers specifically to nuclei that have a long-to-short axis ratio of 2:1 (i.e. nuclei that are twice as long as they are wide) and are symmetric about the long axis, making them resemble a rugby ball.

However, in the last few decades, evidence has mounted for the existence of rather different, *triaxial* strongly deformed (TSD) states in some nuclei. Whereas a

superdeformed nucleus has a long axis and two short axes of equal length, a triaxial nucleus has a long, a short and an intermediate axis and so resembles, to extend the analogy, a rugby ball squashed at its sides, or a kiwi fruit. Strongly deformed triaxial shapes have long been proposed [3], but the first compelling evidence for them was discovered by Ødegård et al. in ^{163}Lu [4]. Several series of states linked by cascades of gamma rays (referred to as *bands*) were observed with features characteristic of a predicted 'wobbling' excitation that is unique to triaxial nuclei.

Triaxial bands have now been identified in a number of nuclei in this region of the nuclear chart, including $^{161-165,167}$Lu [4–8], ^{168,170,174}Hf [9–11], ^{160}Yb [12], ^{160,161,163}Tm [13, 14] and $^{154,157-160}$Er [15–17]. These are consistent with triaxial shapes that are predicted by a range of theoretical models to become energetically favoured at high spin.

However, recent measurements of the *quadrupole moment* (a measure of the asymmetry of charge distribution within the nucleus) of four TSD bands in ^{157}Er and ^{158}Er suggest that the nuclear shape corresponding to these bands is indeed triaxial, but with rotation occurring around the intermediate axis rather than the short axis as predicted [18]. Hence, by making the same measurements in ^{154}Er, we hope to elucidate this rather perplexing result.

The atomic nucleus, measuring $\sim 10^{-15}$ m, cannot be observed directly with any microscope. Instead, its properties must be deduced indirectly using a range of probes. This can involve, for example, creating a nucleus in an excited state and measuring the radiation it emits as it decays, or firing particles at the nucleus and observing the physical properties of scattered particles.

For the work presented in this thesis, we have created the nucleus of interest in an excited state with high spin and measured the energies of gamma rays (hence-

forth written as 'γ rays') emitted by the nucleus as it loses angular momentum and decays down to its ground state. The details of the reaction used to create the nuclei and the apparatus used to measure the emitted γ rays are given in Section 3.1.

Deducing the shape of the nucleus from the γ rays it emits involves a complex series of measurements and calculations. Synonymous with the nuclear shape is its deformation (see Chapter 2 for a description of nuclear deformation parameters). The further a nucleus is from a non-deformed, spherical shape, the higher its quadrupole moment will be. A high quadrupole moment in turn leads to shorter *lifetimes*. The lifetime is the average time for which a nucleus remains in a quantum state before decaying to a less excited state, which in the scope of this analysis involves the emission of a γ ray.

Thus, in order to determine the nuclear shape, we design an experiment that allows us to measure the length of time between γ-ray emissions and thereby work backwards to calculate the deformation parameters of the nucleus when it was in the state that decayed. The way in which this was done is described in Section 3.2.

The nucleus ^{154}Er is interesting for a number of reasons. On the nuclear chart, it straddles two regions where the two types of deformation mentioned, SD and TSD, prevail (Fig. 1.1). Accordingly, it had (prior to this work) two known bands, which were believed to be variously of SD and TSD character based on their measured moments of inertia.

Measuring the quadrupole moments, Q_t, of these two bands should allow us to calibrate the results of the ^{157,158}Er measurements, obtained using the Doppler-shift attenuation method (DSAM). The calculation of nuclear lifetimes from γ-ray energies uses certain theoretical quantities relating to the slowing down of the nucleus within the layers of material in which it is created. These quantities – the *stopping*

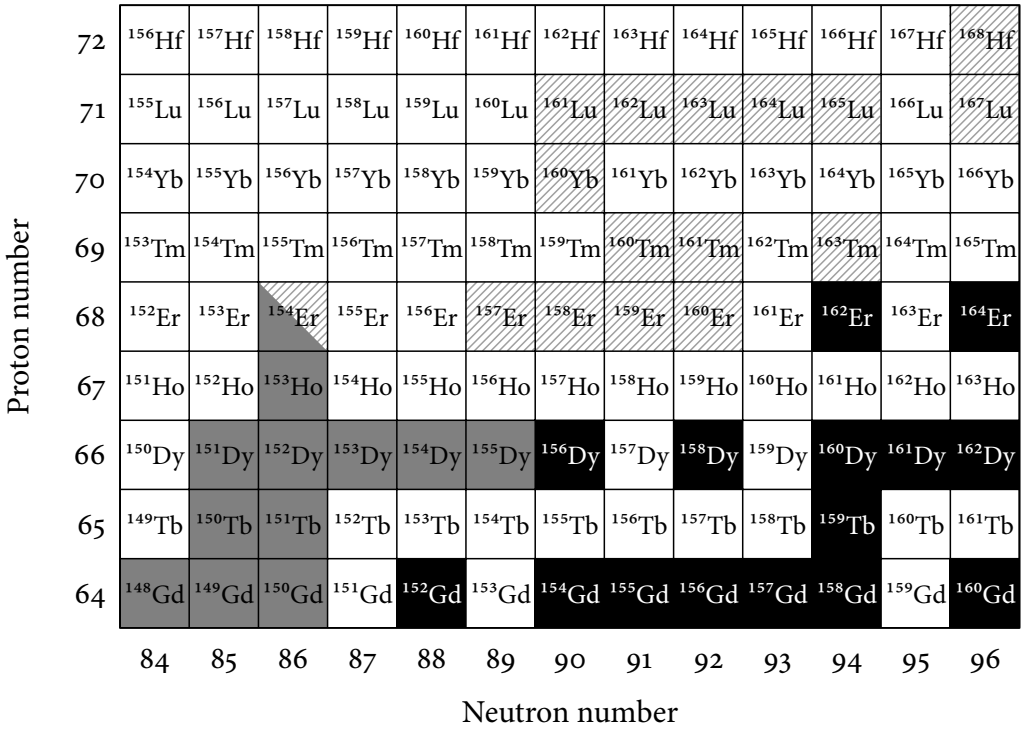

Figure 1.1 The neutron-deficient rare-earth region of the nuclear chart indicating nuclei with known strongly deformed bands. Solid grey denotes superdeformed bands, while hatched lines denote triaxial strongly deformed bands. Black indicates stable nuclei.

powers of the material – are a large source of error, and have indeed caused some difficulty in this analysis (see Section 3.2). The theoretical description of SD bands is now relatively well-established and their quadrupole moments can be predicted with some certainty. How well the experimental quadrupole moment for the SD band in ^{154}Er agrees with its predicted value therefore indicates the accuracy of the theoretical stopping powers used in the DSAM analysis.

Additionally, the coexistence of SD and TSD bands allows us to better compare and contrast the underlying microscopic behaviour of the nucleus' constituent nucleons (neutrons and protons) that lead to the two types of macroscopic deforma-

tion. Details of the theoretical models used to interpret this behaviour are given in Chapter 2, while a comparison of the latest theoretical predictions with the experimental findings is given in Chapter 5.

Lastly, we hoped that the data provided by this experiment would lead to the identification of additional strongly deformed bands in the nucleus that had not been identified thus far because the likelihood of their being populated was so low. We have indeed discovered two such bands in ^{154}Er, and we present these in Chapter 4. The method we used for obtaining them is described in Section 3.3.

Fig. 1.2 is a *level scheme* containing all the states and γ-ray transitions between them known in ^{154}Er prior to this work [15, 19, 20]. The widths of the transitions, represented by arrows, are proportional to the intensity with which they are observed experimentally, while their lengths indicate their energy in thousands of electron volts (keV). The height of a state is thus a measure of its excitation energy, and the γ rays below it are the ways by which the nucleus can lose this excitation energy and decay to its ground state. At this point, it should perhaps be noted that although the experiment involves creating a nucleus at high spin and observing its decay, it is often more convenient talk about the nucleus in terms of how it *builds up* its spin from a state of low excitation.

The main part of the ^{154}Er level scheme consists of low-deformation *oblate* (discus-shaped) states that carry most of the intensity. These states, and their transitions, will be referred to as 'normally-deformed' (ND) in this thesis. To the left of these states are two 'floating' bands - the two known strongly deformed bands. Their placement is approximate, since the transitions that link them to the ND states have not been observed. Their spins, and the point at which they feed into the main level scheme, have been inferred by Lagergren et al. [15] from ND transi-

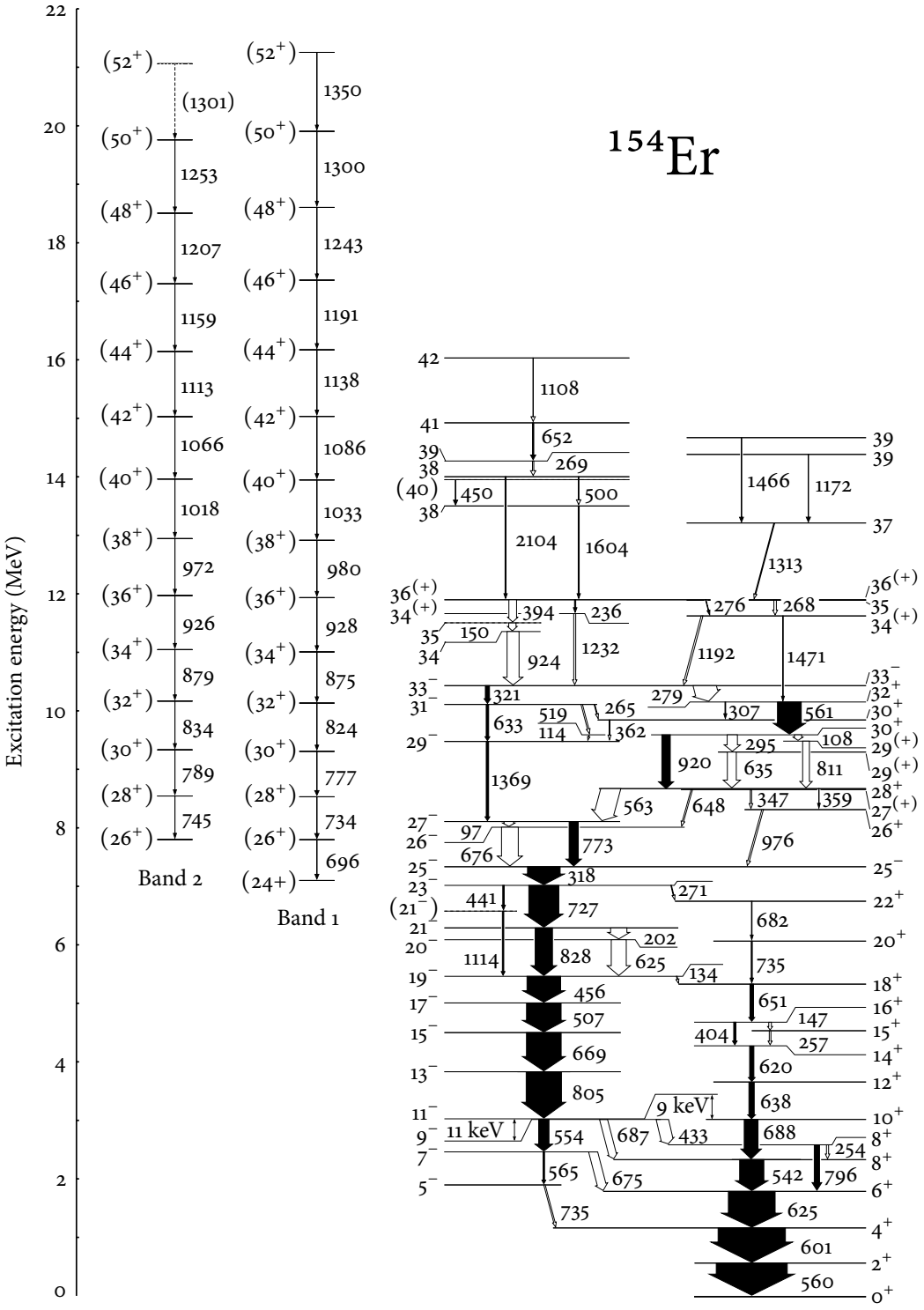

Figure 1.2 The known level scheme of ^{154}Er prior to this work [15, 19, 20]. Levels are labelled by spin and parity, I^{π}, and γ-ray energies are in units of keV.

tions observed in coincidence with in-band transitions.

There is a striking difference in appearance between the ND and strongly deformed bands. With the exception of the first few states up to spin $I = 6$, the former are rather disorganised, while the latter are regularly spaced with a gradual, almost constant increase in transition energy with spin. These are manifestations of two different kinds of excitation – *single-particle* and *collective* – for which nuclei in this region are an ideal testing ground. Single-particle excitations involve the interactions between individual nucleons (protons and neutrons), which in a nucleus with many nucleons can lead to a complex system of quantum states. Collective excitations, such as rotation and vibration, involve the nucleus as whole and tend to result in a simple arrangement of states like those in our strongly deformed bands. However, the interaction between the two kinds of excitation will be crucial in understanding the underlying structure of these bands.

Chapter 2

Theory

A theoretical description of the nucleus that accounts for all the interactions between individual nucleons rapidly becomes intractable as the number of nucleons is increased. This has led to the development of theoretical models that simplify calculations by using approximations of certain properties of the nuclear system. In this chapter, we discuss models of increasing sophistication leading up to the Cranked Nilsson-Strutinsky (CNS) model that was used to produce the theoretical results in Chapter 5.

The levels shown in Fig. 1.2 illustrate the existence of discrete quantum states with specific angular momentum and excitation energy. This is as opposed to the situation in a classical system, for example a spinning top, which experiences a continuous range of angular momenta and energies. We shall see that these discrete levels arise naturally from a quantum-mechanical treatment of the nucleons.

2.1 Nuclear models

2.1.1 The shell model

A successful nuclear model must recreate the *shell structure* of nuclei observed experimentally. This idea posits that nucleons occupy discrete energy levels that are clustered in shells separated by energy gaps, analogous to the way electrons orbiting an atom occupy electron shells. In the case of electrons, the occupation of these shells gives rise to trends in the chemical properties of atoms across the periodic table. Similarly, the variation in certain physical properties of nuclei across the nuclear chart is consistent with the existence of 'magic numbers' of neutrons and protons (N and Z, respectively) that correspond to filled shells.

For example, the neutron separation energy (the energy required to remove a neutron from the nucleus) shows a sudden drop after a magic number [21], suggesting that nuclei added beyond this number occupy a higher, less tightly-bound shell. The magic numbers for nuclei near stability are

$$2,\ 8,\ 20,\ 28,\ 50,\ 82,\ 126. \tag{2.1}$$

The grouping of orbitals, together with the discrete orbitals themselves, appear if each nucleon is treated as if it is moving in a potential energy well. This potential serves as an approximation of the net attractive force resulting from the other nucleons, and as such it is referred to as a *mean field* potential.

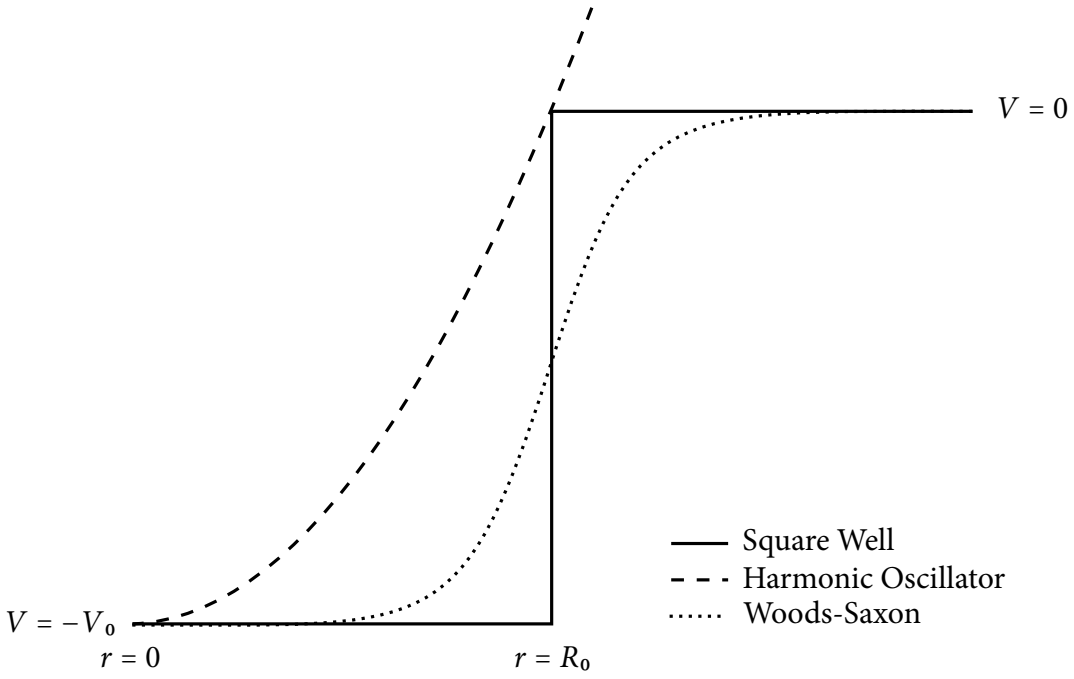

Figure 2.1 Three possibilities for the nuclear potential: a simple square well potential with $V(r) = -V$, $r \leq R$; $V(r) = 0$, $r > R$; a Simple Harmonic Oscillator of the form given in Eq. 2.2; a more realistic Woods-Saxon potential, similar to the Nilsson potential given in Eq. 2.6, of the form $V(r) = -V_0[1 - (r/R_0)^2]$.

2.1.2 The Simple Harmonic Oscillator potential

We begin with a simple potential, the Harmonic Oscillator (Fig. 2.1), of the form

$$V_{\text{osc}}(\mathbf{r}) = \tfrac{1}{2}k\mathbf{r}^2 = \tfrac{1}{2}m\omega^2\mathbf{r}^2, \tag{2.2}$$

where $\mathbf{r}$ is the three-dimensional position coordinate, k is the classical spring constant, m is mass and ω is the harmonic oscillator frequency. We incorporate this into the nuclear Hamiltonian, the quantum-mechanical operator that describes the

energy of the system, which is of the form

$$H(\mathbf{r}) = -\frac{\hbar}{2m}\nabla^2 + V(\mathbf{r}), \tag{2.3}$$

where the first term is the particle's kinetic energy. The energy eigenvalues corresponding to the solutions to the Hamiltonian are given by

$$E_N = (N + \tfrac{3}{2})\hbar\omega, \quad N \geq 0 \tag{2.4}$$

where the integer N is the oscillator quantum number. An important property of the orbitals, the *parity* π, emerges at this point. For the Simple Harmonic Oscillator, $\pi = (-1)^N$, where $\pi = 1$ is positive parity and $\pi = -1$ negative parity. In physical terms, the parity signifies whether the particle's wavefunction is symmetric or antisymmetric with respect to a reflection of spatial coordinates through the origin, corresponding to positive and negative parity, respectively.

The energy eigenvalues and their corresponding N are shown on the left of Fig. 2.2. The levels are *degenerate*, meaning that multiple eigenstates have the same energy. The number of degenerate states gives the occupancy of each level, i.e. the number of nucleons that can fill the level. This is limited by the Pauli exclusion principle, which states that no two particles can have the same quantum numbers. The quantum numbers that define the harmonic oscillator orbitals are l, the angular momentum quantum number, and n, which counts the total number of orbitals with a given l. Their allowed values are governed by the rules

$$2(n-1) + l = N, \quad N \geq 0, \quad 0 \leq l \leq N. \tag{2.5}$$

The nl orbitals that make up each N shell are given in Fig. 2.2, using the conventional lettering system for l values ($s = 0$, $p = 1$, $d = 2$, $f = 3$, $g = 4$, $h = 5$, $i = 6$). The parity of the orbitals is now given by $\pi = (-1)^l$ (Eq. 2.5 ensures that this is consistent with $(-1)^N$).

Further degeneracy is present due to the fact that nucleons have an intrinsic angular momentum $\mathbf{s}$, which has magnitude ½. The quantities l and s sum together to the total angular momentum j. The vectors $\mathbf{l}$ and $\mathbf{s}$ can be both aligned or anti-aligned, and so $j = l \pm \frac{1}{2}$, resulting in the nlj orbitals listed on the right of Fig. 2.2. (We see will why these orbitals are split in the next section.)

Still further degeneracy results from the fact that each j-value has *magnetic substates* with quantum number m. This is the projection of j along the quantisation axis of the nucleus, and can have the values $j,\ j-1, \ldots -j$. Thus each nlj orbital has $2j+1$ substates which, following the Pauli principle, can only contain $2j+1$ nucleons.

In this way, we obtain the final occupancy numbers for the Harmonic Oscillator potential levels. The running total of these (Fig. 2.2) gives the Harmonic Oscillator magic numbers. As can be seen, only the first three empirical magic numbers are reproduced correctly.

2.1.3 Modified Harmonic Oscillator

The Modified Harmonic Oscillator (MHO) or Nilsson potential introduces additional terms to the Harmonic Oscillator potential that make it more realistic, giving

$$V_{\mathrm{MHO}} = V_{\mathrm{osc}} - \kappa\hbar\omega_0 \left[2\mathbf{l}\cdot\mathbf{s} + \mu(\mathbf{l}^2 - \langle \mathbf{l}^2 \rangle_N) \right]. \tag{2.6}$$

where ω_0 is defined as

$$\hbar\omega_0 = 41A^{-1/3}\left(1 \pm \frac{N-Z}{3A}\right) \text{ MeV}, \tag{2.7}$$

using a plus sign for neutrons and a minus sign for protons [22]. The last term in Eq. 2.6, in $\mathbf{l}^2$, flattens out the bottom of the potential, bringing it closer to a square well potential (Fig. 2.1). The degeneracy of the Harmonic Oscillator shells is partly broken, with higher-l orbitals being brought down lower in energy (Fig. 2.2, centre).

The second term on the right of Eq. 2.6 is an $\mathbf{l}\cdot\mathbf{s}$ or spin-orbit term, arising from the coupling between the intrinsic and orbital angular momenta. This further breaks the degeneracy of the orbitals into their $j = l + \frac{1}{2}$ and $j = l - \frac{1}{2}$ components, which are respectively lowered and raised in energy (Fig. 2.2, right). The parameters κ and μ are adjustable and can be fit to experimental data. For calculations in the present work, $A \sim 150$ parameters were used [24].

Following these modifications, we see that new groups of orbitals separated by energy gaps are formed. The total occupancy at these new shells closures corresponds to the empirically observed magic numbers. The first term on the right of Eq. 2.6 is, for a spherical nucleus, simply $\frac{1}{2}m\omega_0^2\mathbf{r}^2$. However, we deal extensively in this thesis with deformed (i.e. non-spherical) nuclei for which the potential is not the same in all directions (or *anisotropic*). The next section details how the V_{osc} term in the Nilsson potential accounts for axially-deformed nuclei.

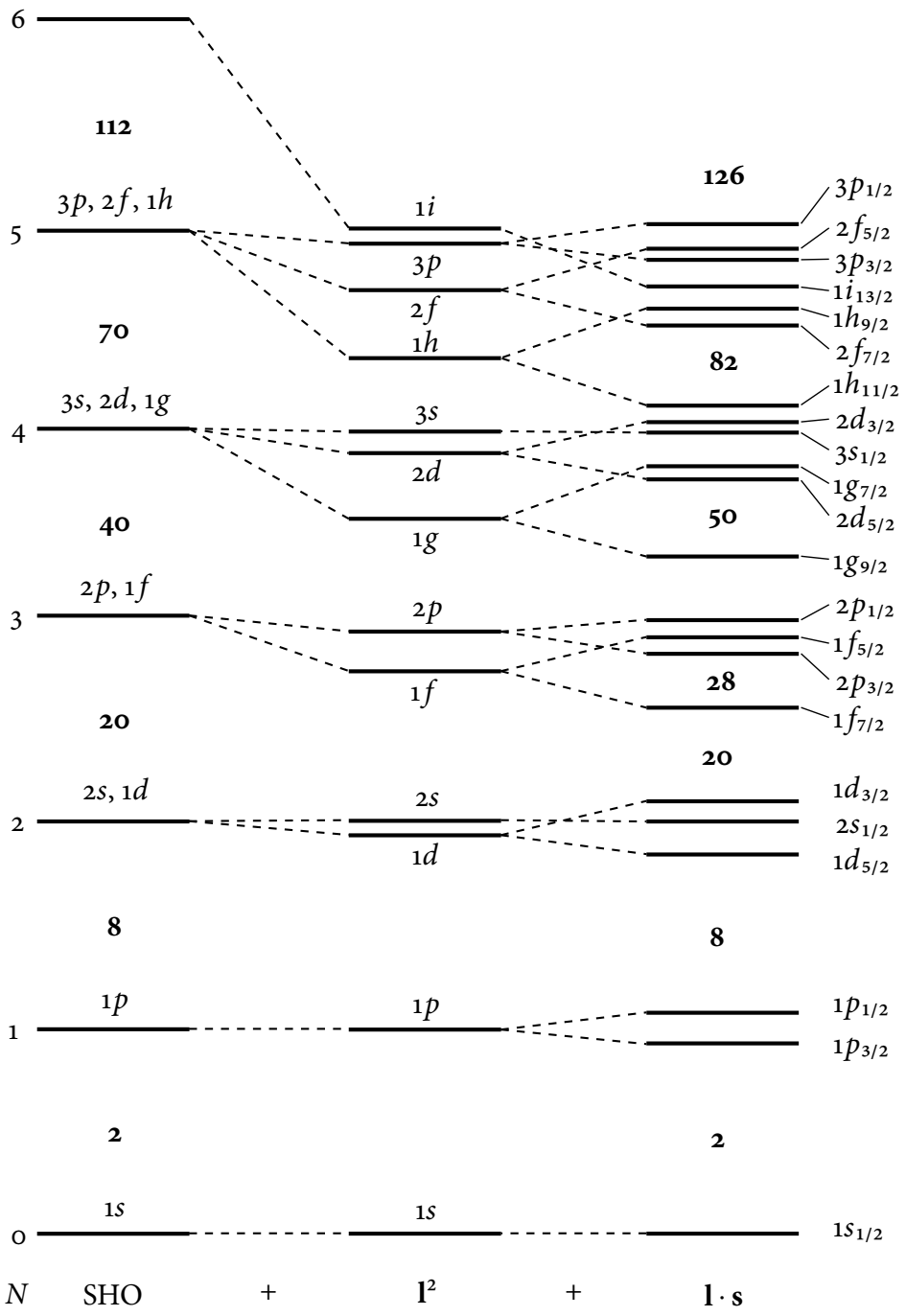

Figure 2.2 The effect of adding $\mathbf{l}^2$ and $\mathbf{l} \cdot \mathbf{s}$ terms to the Simple Harmonic Oscillator (SHO) potential on level energy and degeneracy. Magic numbers are shown in bold. Adapted from Ref. [23].

2.1.4 Anisotropic Harmonic Oscillator

The Anisotropic Harmonic Oscillator (AHO) potential has separate oscillator frequencies for the symmetry axis, z, and perpendicular axes, x and y, since the nuclear radius is no longer the same along these axes in a deformed nucleus. Thus the potential becomes

$$V_{\text{osc}} = \tfrac{1}{2}m\left[\omega_{\perp}^2(x^2 + y^2) + \omega_z^2 z^2\right]. \tag{2.8}$$

We can parametrise the deformation by transforming into a 'stretched' coordinate system [25], defined by

$$\xi = x\sqrt{\frac{m\omega_x}{\hbar}}; \qquad \eta = y\sqrt{\frac{m\omega_y}{\hbar}}; \qquad \zeta = z\sqrt{\frac{m\omega_z}{\hbar}}, \tag{2.9}$$

where $\omega_x = \omega_y = \omega_{\perp}$. Then, if we define the quantities

$$\rho^2 = \xi^2 + \eta^2 + \zeta^2; \qquad \cos\theta_{\text{t}} = \zeta/\rho, \tag{2.10}$$

the potential can be rewritten as [25]

$$V_{\text{osc}} = \tfrac{1}{2}\hbar\omega_{\perp}\xi^2 + \tfrac{1}{2}\hbar\omega_{\perp}\eta^2 + \tfrac{1}{2}\hbar\omega_z\zeta^2 \tag{2.11}$$

$$= \tfrac{1}{2}\hbar\omega_0(\varepsilon_2)\rho^2\left[1 - \tfrac{2}{3}\varepsilon_2 P_2(\cos\theta_{\text{t}})\right], \tag{2.12}$$

where P_2 is the second Legendre polynomial and ε_2 is the deformation parameter, which we use in this thesis for theoretical descriptions of the nucleus. The value of ω_0, defined for a spherical shape in Eq. 2.7, must be adjusted slightly as a function

of ε_2 to conserve the volume of the nuclear shape. Higher-order deformations of the form $\varepsilon_\lambda \rho^2 P_\lambda(\cos\theta_t)$ may be added to the potential, and indeed we use a value of $\varepsilon_4 = \frac{1}{6}\varepsilon_2^2$ for the calculations in Chapter 5.

As ε_2 is increased or decreased from zero, the energies of the orbitals change (see Figs. 2.3 and 2.4). At certain deformations, orbitals of similar character approach each other in energy and undergo a mixing of their wavefunctions. Beyond this deformation, the character of the wavefunctions has been exchanged. Effectively, this means that the *nlj* quantum numbers used so far are not conserved as deformation is varied – they are not 'good' quantum numbers. For this reason, we use the asymptotic quantum numbers,

$$[Nn_z\Lambda]\Omega^\pi,$$

where N is the oscillator shell as before, n_z is the number of oscillation quanta along the deformation axis z, Λ is the projection of l along z, Ω the projection of j and π is the parity. Λ and Ω are illustrated in Fig. 2.5. Σ, the projection of s along z, is equal to $\pm\frac{1}{2}$ and so $\Omega = \Lambda \pm \frac{1}{2}$ (Σ is omitted from the label since it can be deduced from Ω and Λ).

As can be seen in Figs. 2.3 and 2.4, the deformation breaks the degeneracy of the spherical orbitals. As ε_2 becomes more negative, Nilsson orbitals with higher values of Ω are brought down in energy, while those with lower Ω are raised in energy. In the positive-ε_2 direction, the opposite is true.

The reasons for this can be understood intuitively if one considers the physical trajectories of the orbitals around the deformed nucleus. Negative ε_2 represents an oblate, 'discus' shape flattened along the z axis. A Nilsson orbital with a given j

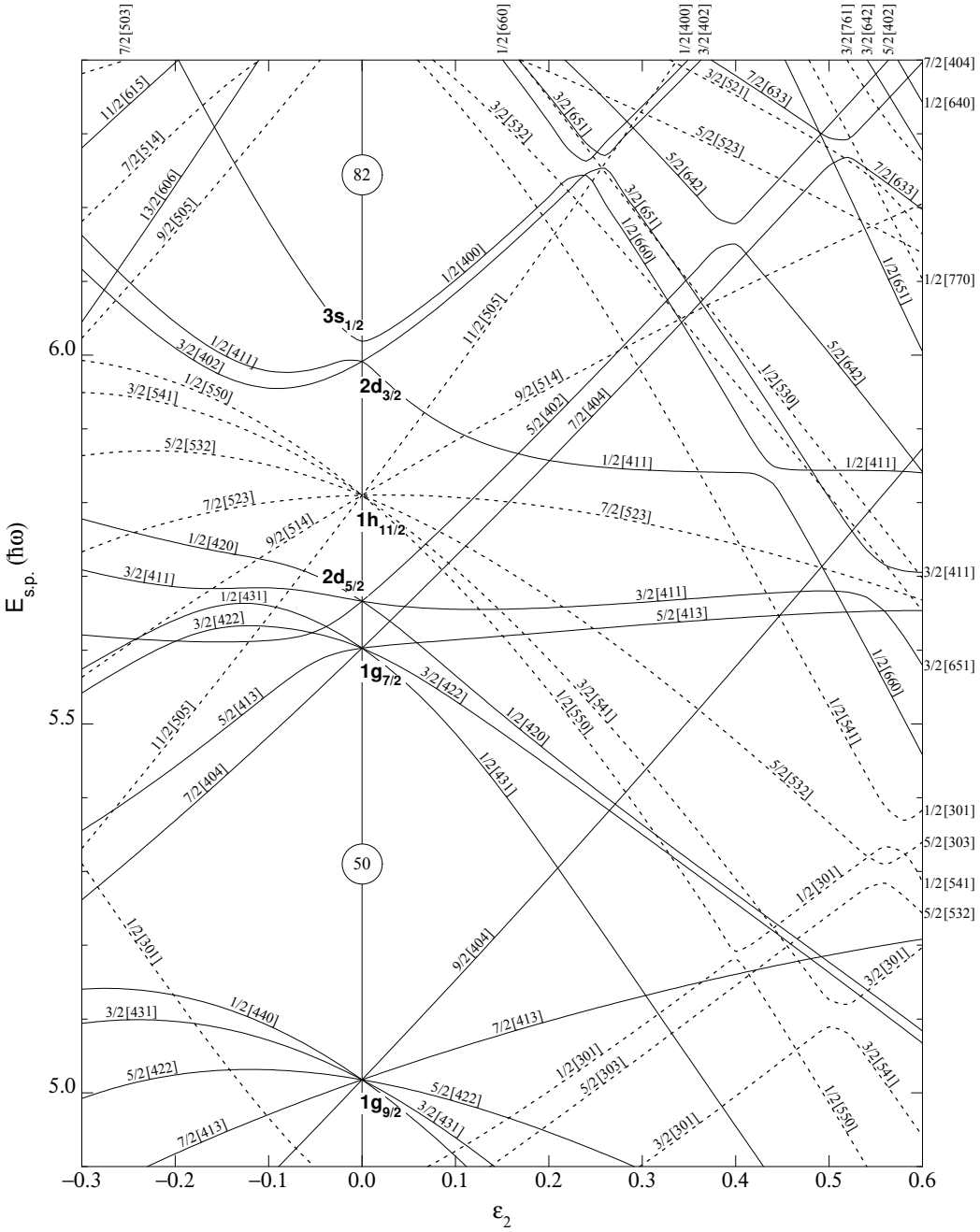

Figure 2.3 Nilsson diagram for protons, $50 \leq Z \leq 82$ ($\varepsilon_4 = \varepsilon_2^2/6$). Solid lines indicate $\pi = +$ and dashed lines $\pi = -$. Reprinted from Ref. [26].

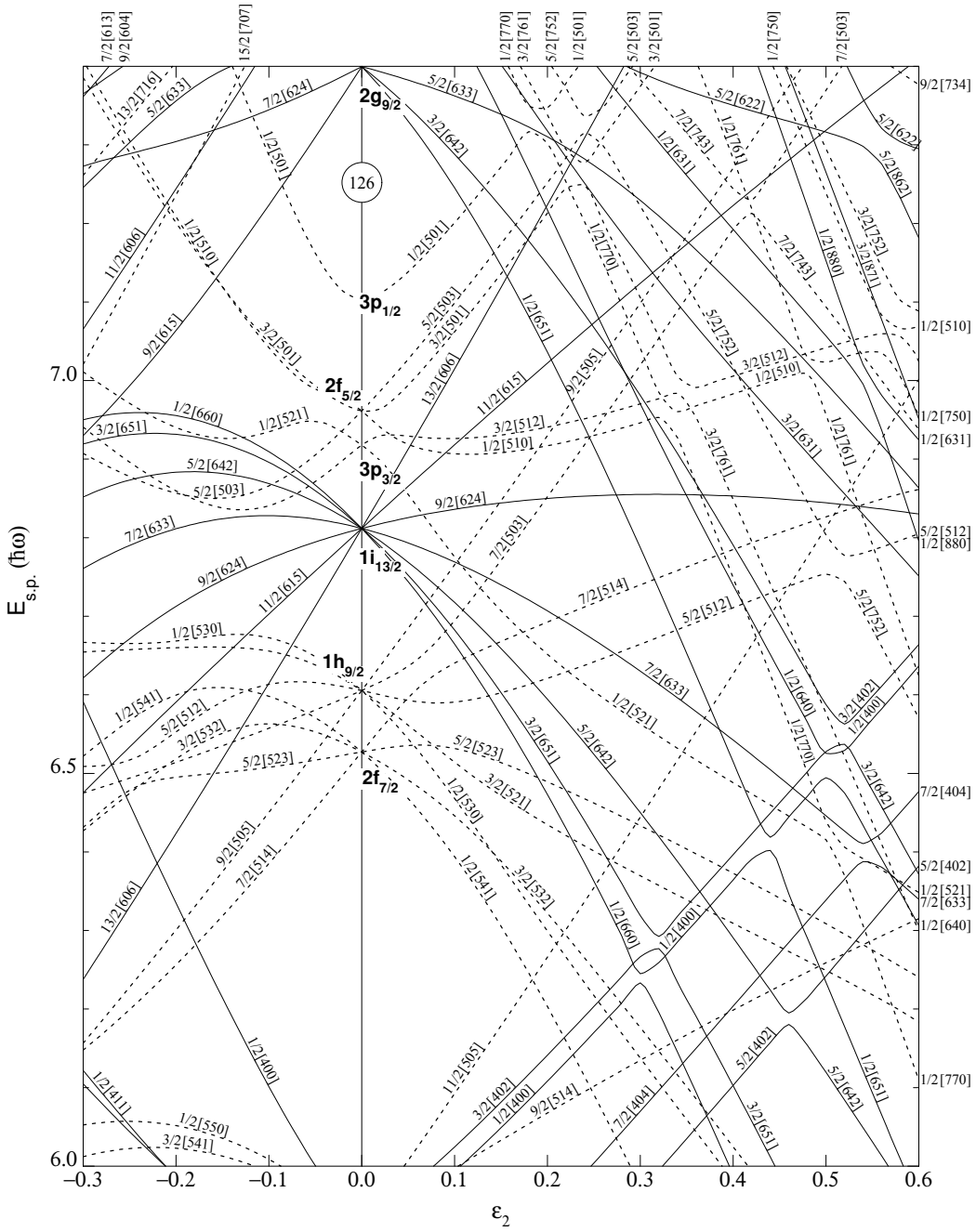

Figure 2.4 Nilsson diagram for neutrons, $82 \leq N \leq 126$ ($\varepsilon_4 = \varepsilon_2^2/6$). Solid lines indicate $\pi = +$ and dashed lines $\pi = -$. Reprinted from Ref. [26].

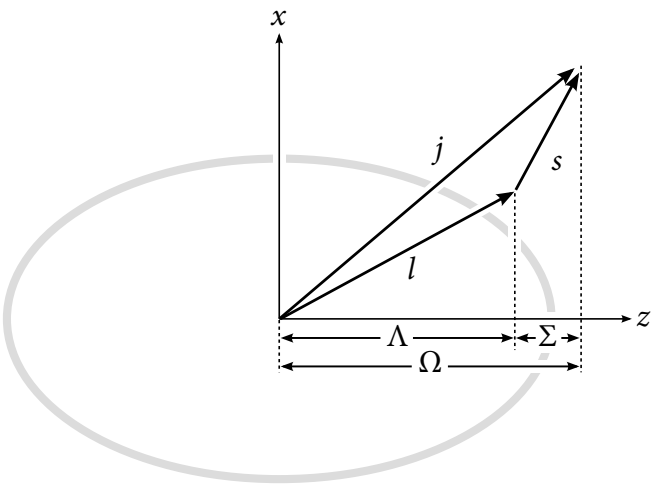

Figure 2.5 Spin projection quantum numbers for a Nilsson orbital. Here, z is the deformation axis of the nucleus and x the rotation axis.

and the maximum Ω, i.e. $\Omega = j$, must have an orbit almost perpendicular to the deformation axis and close to where the nuclear potential is at its widest. Hence, its energy is lowered for greater oblate deformation. By the same reasoning, a Nilsson orbital with the same j but the minimum Ω, i.e. $\Omega = \frac{1}{2}$, orbits the narrowest part of the nuclear potential, and so its energy increases for greater oblate deformation.

Analogous arguments can be applied to positive ε_2 deformation, which represents a prolate or 'cigar' shape that is stretched along the z axis. Here, the increase in deformation has the opposite effect on the energies of orbitals with different Ω, with low-Ω orbitals being brought down in energy while high-Ω orbitals are raised.

As ε_2 is increased and the Nilsson orbitals are rearranged, the spherical shell gaps disappear to be replaced by shell gaps with different values of N and Z. It is these deformed shell gaps that lead to relatively stable highly deformed and superdeformed shapes. We continue this idea in the following sections, where the

orbitals are further rearranged by triaxial deformation and collective rotation, creating the possibility of stable triaxial shapes at high spin.

2.1.5 Triaxiality

The potential in Eq. 2.8 only allows one to specify shapes with axial symmetry, i.e. shapes that are symmetrical about the deformation axis z. We would like to go further and consider triaxial shapes, for which $\omega_x \neq \omega_y \neq \omega_z$. The AHO potential then becomes

$$V_{\text{osc}} = \tfrac{1}{2}m\left[\omega_x^2 x^2 + \omega_y^2 y^2 + \omega_z^2 z^2\right]. \tag{2.13}$$

The ratio of the three axes can be specified by a triaxiality parameter γ (in $^\circ$) in accordance with the Lund convention shown in Fig. 2.6. The harmonic oscillator frequencies along each axis in terms of ε_2 and γ are

$$\omega_x = \omega_0(\varepsilon_2, \gamma)\left[1 - \tfrac{2}{3}\varepsilon_2 \cos(\gamma + 2\pi/3)\right], \tag{2.14}$$

$$\omega_y = \omega_0(\varepsilon_2, \gamma)\left[1 - \tfrac{2}{3}\varepsilon_2 \cos(\gamma - 2\pi/3)\right], \tag{2.15}$$

$$\omega_z = \omega_0(\varepsilon_2, \gamma)\left[1 - \tfrac{2}{3}\varepsilon_2 \cos(\gamma)\right]. \tag{2.16}$$

The length of the principle axis $i = x, y, z$ is then inversely proportional to ω_i. In this work we investigate the possible existence of TSD shapes with positive and negative γ. Examples of these two shapes are shown in Fig. 2.7, with slightly larger values of (ε_2, γ) than are predicted for ^{154}Er in order to emphasise their differences.

Using the stretched coordinates defined in Eqs. 2.9, Eq. 2.13 can be rewritten

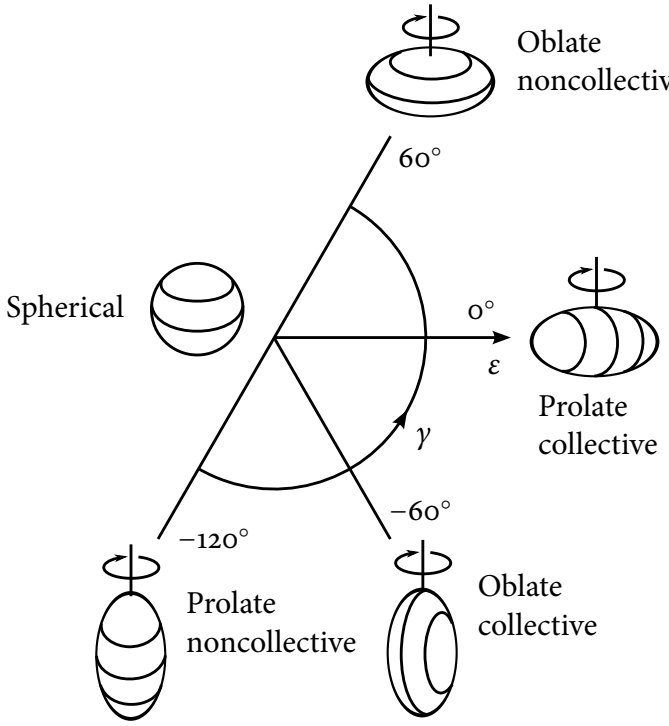

Figure 2.6 The Lund convention for the parametrisation of triaxial shapes using γ and ε_2 [27].

according to Ref. [28] as

$$V_{\rm osc} = \tfrac{1}{2}\hbar\omega_0\rho^2\left[1 - \tfrac{2}{3}\varepsilon_2\sqrt{\frac{4\pi}{5}}\left\{\cos\gamma\, Y_2^0 - \frac{1}{\sqrt{2}}\sin\gamma\,(Y_2^2 + Y_2^{-2})\right\}\right], \qquad (2.17)$$

where Y_l^m are spherical harmonics. As might be expected, increasing or decreasing γ from 0° induces further changes to the energies of the Nilsson orbitals, leading to triaxial shell gaps. The effect on proton and neutron orbitals of increasing γ from 0° to 20° is shown in Fig. 5.6.

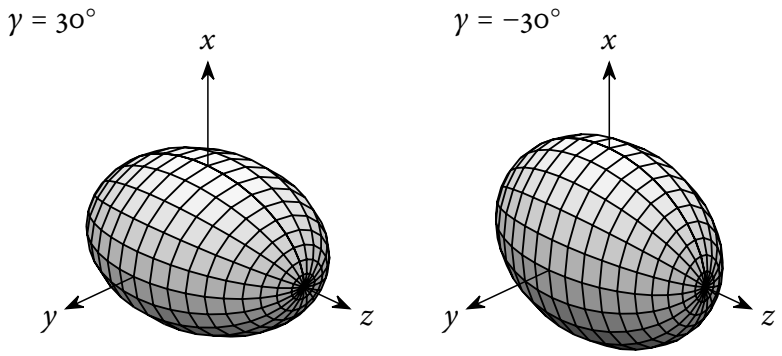

Figure 2.7 Positive- and negative-γ TSD shapes with $\varepsilon_2 = 0.4$. The x-axis corresponds to the rotation axis.

2.1.6 Potential energy surfaces and the Strutinsky method

In Chapter 5 we present a plane in deformation space, like that in Fig. 2.6, onto which a potential energy surface (PES) is superimposed, giving the total energy of the nucleus at any value of (ε_2, γ). Thus, minima on this surface indicate values of ε_2 and γ belonging to relatively stable nuclear shapes for the nucleus of interest. These minima form the basis of subsequent calculations that give favoured configurations of occupied orbitals. These are also presented in Chapter 5.

The method for producing PES plots, described in Ref. [29], essentially involves calculating the total energy for each point on a 'mesh' in the (ε_2, γ) plane and interpolating between these points. The total energy is calculated from the liquid-drop model (LDM) energy [30], which is able to reproduce the the bulk properties of the nucleus, plus a correction term [31] that accounts for the shell structure of the single-particle orbitals, calculated using the Nilsson potential.

2.1.7 Cranking

Finally, we introduce the cranking model, which deals with the effects of collective rotation on the nucleus. The cranking Hamiltonian or *Routhian* is the Hamiltonian for the system in the intrinsic frame of reference [29], given by

$$H_\omega = H_0 - \omega I_x = \sum h_\omega, \tag{2.18}$$

where H_0 is the sum of all the single-particle static Hamiltonians, ω is the rotational frequency, I_x is the projection of the total angular momentum onto the rotation axis and the single-particle Hamiltonians are given by

$$h_\omega = h_0 - \omega i_x. \tag{2.19}$$

The $-\omega I_x$ term is analogous to the classical Coriolis and centrifugal forces.

At $I = 0$, each Nilsson orbital is doubly degenerate, with pairs of nucleons occupying symmetrical *time-reversed* orbits. Under rotation, time-reversal symmetry is broken and orbitals are split into partners with opposite values of the *signature exponent quantum number* α. This quantum number comes from the eigenvalue of the rotation operator $\mathcal{R}_x(\pi)$, which represents a rotation of the particle wavefunction by 180° around the rotation axis, or

$$\mathcal{R}_x(\pi)\psi = \exp(-i\pi I_x)\psi = r\psi, \tag{2.20}$$

where r is the signature quantum number and is related to α by

$$r = e^{-i\pi\alpha}. \tag{2.21}$$

For single-particle orbitals, r is a phase factor of $\pm i$, and so $\alpha = \pm\frac{1}{2}$.

As the nucleus is rotated, the energies of opposite-signature orbitals are affected differently and a further rearranging of orbitals together with the appearance of new shell gaps may be observed (Fig. 5.6). This has the effect that deformation minima change as a function of spin, and deformed shapes that are not stable at low spins become more stable as spin is increased.

2.2 Observables

This section describes physical quantities that are directly measurable or easily derivable from the experimental data. They are not only useful in that they tell us something about the properties of the nucleus, but also because they can be compared with theoretical values in order to determine the accuracy of a theoretical model or a specific nucleon configuration assignment.

2.2.1 Rotational frequency

The rotational frequency of a collectively rotating nucleus at a particular value of excitation energy E and spin I is given by

$$\omega = \frac{\mathrm{d}E}{\mathrm{d}I} \approx \frac{\Delta E}{\Delta I} = \frac{E_\gamma}{2\hbar}, \tag{2.22}$$

where the right-hand side holds true for $\Delta I = 2$ transitions, which is assumed to be the case for the transitions in the strongly deformed bands of ^{154}Er. The quantity $\omega\hbar$ is therefore half the transition energy. This is particularly useful in our case, since we do not know the absolute spins of the bands of interest.

2.2.2 Effective alignment

A useful concept when comparing strongly deformed bands in neighbouring nuclei is the additivity of energy and spin contributions from the occupation of individual orbitals [32]. The effective alignment, i_{eff}, between two bands is defined as

$$i_{\text{eff}} = I_1(\omega) - I_2(\omega), \tag{2.23}$$

where $I_1(\omega)$ and $I_2(\omega)$ are the spins of the bands being compared at a given ω. Following the principle of additivity, the value of i_{eff} is the sum of the individual spin contributions from additional particles in band 1 with respect to band 2. This is helpful when making configuration assignments, such as in Chapter 5 where we use i_{eff} to compare the ^{154}Er SD band with the 'yrast' SD band of ^{152}Dy.

2.2.3 Moments of inertia

The kinematic and dynamic moments of inertia are defined as

$$\mathcal{J}^{(1)} = I\left\{\frac{\mathrm{d}E}{\mathrm{d}I}\right\}^{-1} = \frac{I}{\omega} \tag{2.24}$$

and

$$\mathcal{J}^{(2)} = I\left\{\frac{\mathrm{d}^2E}{\mathrm{d}I^2}\right\}^{-1} = \frac{\mathrm{d}I}{\mathrm{d}\omega} = \mathcal{J}^{(1)} + \omega\frac{\mathrm{d}\mathcal{J}^{(1)}}{\mathrm{d}\omega} \tag{2.25}$$

$$\approx \frac{4}{E_\gamma(I+2 \to I) - E_\gamma(I \to I-2)} \tag{2.26}$$

in units of in units of $\hbar^2\,\text{MeV}^{-1}$. The $\mathcal{J}^{(2)}$ moment of inertia describes the response of the nucleus to a torque [33]. It is very sensitive to internal changes of structure,

and its value gives an indication of the deformation of the nucleus – large $\mathcal{J}^{(2)}$ generally indicates large deformation. As with the rotational frequency, the $\mathcal{J}^{(2)}$ moment of inertia does not require knowledge of the absolute spins of the band.

2.2.4 Quadrupole moments

The ultimate goal of this work is to measure the electric quadrupole moments of the two strongly deformed bands. This quantity is a measure of how much the charge distribution in the nucleus deviates from spherical symmetry [34]. The quadrupole moment we measure in this work is referred to as the *transition* quadrupole moment, Q_t, and can be expressed in terms of the density distribution along the principle axes (x, y and z) [18] as

$$Q_t = e\sqrt{\tfrac{8}{3}}|Q_{22}(\hat{x})|, \tag{2.27}$$

where $Q_{22}(\hat{x})$ is the Q_{22} component of the quadrupole moment around the rotation axis [3], given by

$$Q_{22}(\hat{x}) = \sqrt{\tfrac{3}{2}}\left\langle y^2 - z^2 \right\rangle. \tag{2.28}$$

Hence Q_t is proportional to the difference in the nuclear radius between the two axes perpendicular to the rotation axis. This means that a triaxial shape rotating about its intermediate axis (i.e. negative γ), with the y-axis corresponding to the short axis, will have a larger Q_t than the same shape rotating about its short axis (positive γ), with the y-axis corresponding to the intermediate axis. This result allows us to identify the nuclear shape for a strongly deformed band by comparing

its experimental Q_t with the theoretical value for the positive- and negative-γ TSD shapes.

Experimentally, we measure Q_t by (indirectly) measuring the lifetimes of the states in the strongly deformed bands. These two quantities can be related in the following way [35]:

$$\tau = B_\gamma \frac{821.0565}{Q_t^2 E_\gamma^5 \langle IK20|I-2K\rangle^2}, \tag{2.29}$$

where τ is in femtoseconds ($1\,\mathrm{fs} = 10^{-15}\,\mathrm{s}$), B_γ is the branching ratio of the level, $\langle IK20|I-2K\rangle$ is the Clebsch-Gordan coefficient for the transition with a value of roughly $(\frac{3}{8})^{1/2}$, Q_t is in electron-barns and E_γ is in MeV. The measurement of τ forms the basis of the Doppler-shift attenuation method (DSAM) described in Chapter 4.

Chapter 3

Methods

3.1 Experimental details

The experiment that provided the data used in this thesis was performed at the ATLAS facility in Argonne National Laboratory, USA, using the Gammasphere detector array. The following sections include a description of the reaction used to populate high-spin states in ^{154}Er, details of Gammasphere, and a description of the target setup necessary for the DSAM.

3.1.1 Fusion-evaporation

High-spin states in ^{154}Er were populated using the fusion-evaporation reaction ^{110}Pd(^{48}Ti,4nγ)^{154}Er. A 215 MeV ^{48}Ti ion beam supplied by the ATLAS accelerator with a beam current of 20–30 enA bombarded a ^{110}Pd target, forming the compound nucleus ^{158}Er. ^{154}Er was then formed through the evaporation of four neutrons.

The intensity patterns of SD bands generally show a steep increase as the bands

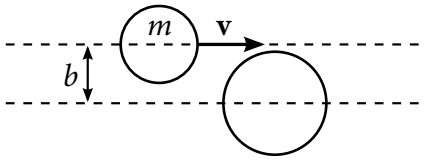

Figure 3.1 A schematic illustration of a heavy-ion reaction showing the impact parameter b.

decay from their highest spin followed by a levelling off, in contrast to the gradual gain in intensity for ND bands [36], indicating that strongly deformed bands are fed primarily at high spins. It is therefore crucial that the reaction is designed to impart the resulting nuclei (or 'recoils') with the greatest possible amount of angular momentum.

The angular momentum transferred to the compound nucleus by a beam with linear momentum $\mathbf{p} = m\mathbf{v}$ is $\mathbf{l} = \mathbf{b} \times \mathbf{p}$, where $\mathbf{b}$ is the impact parameter, shown in Fig. 3.1. Hence the angular momentum, $l = mvb$, can be increased by raising the momentum of the beam particle or increasing the impact parameter. In practice, fusion only occurs for small values of b. For larger values, other reaction processes such as Coulomb excitation and inelastic scattering dominate.

The linear momentum of the projectile, mv, increases with the projectile mass and beam energy. However, this quantity is also limited by competition with fission such that the maximum angular momentum increases with beam energy up to a critical value [37]. This critical value, in its turn, reaches a maximum of around $77\,\hbar$ at $A \approx 140$ [38] (for greater masses, Coulomb repulsion makes fission more favourable and the critical angular momentum is lowered). This makes the rare earth region of the nuclear chart particularly well-suited to the study of high-spin behaviour.

When fusion occurs, it takes 10^{-20} s for the compound nucleus to reach thermodynamic equilibrium, after which its formation history has no influence on its behaviour. This is followed by particle evaporation, with the Coulomb barrier making neutron emission more likely than proton emission in this region of the nuclear chart. Neutrons carry away 8–10 MeV of excitation energy but only 1–2 $\hbar$ of angular momentum, effectively 'cooling' the nucleus, until a low enough excitation energy is reached for γ-ray emission to become more energetically favourable. Statistical model calculations for this process are shown for Fig. 3.2.

Initial γ decays are via competing quadrupole and dipole γ rays emitted from a quasicontinuum of high-energy states [40]. The γ rays have a continuous range of energies and therefore cannot be resolved experimentally, appearing instead as background 'bumps'. Eventually, the quasicontinuum transitions come to populate discrete *yrast* (lowest energy for a given spin) or near-yrast states, namely the ND and strongly deformed states shown in Fig. 1.2.

Cross-section calculations performed using the fusion-evaporation simulation program PACE [41] served as a guide by which to choose an appropriate beam energy for the reaction. However, in this case, we have used an identical beam and target to those successfully used by Lagergren et al. to study ^{154}Er [15], hence the same beam energy of 215 MeV was used.

3.1.2 Gamma-ray detection

Since the strongly deformed bands in ^{154}Er make up less than 1% of the total intensity of the 4n channel, an efficient γ-ray detection system is essential. As will be seen in Section 3.2.1, we isolate the γ rays of interest by imposing the condi-

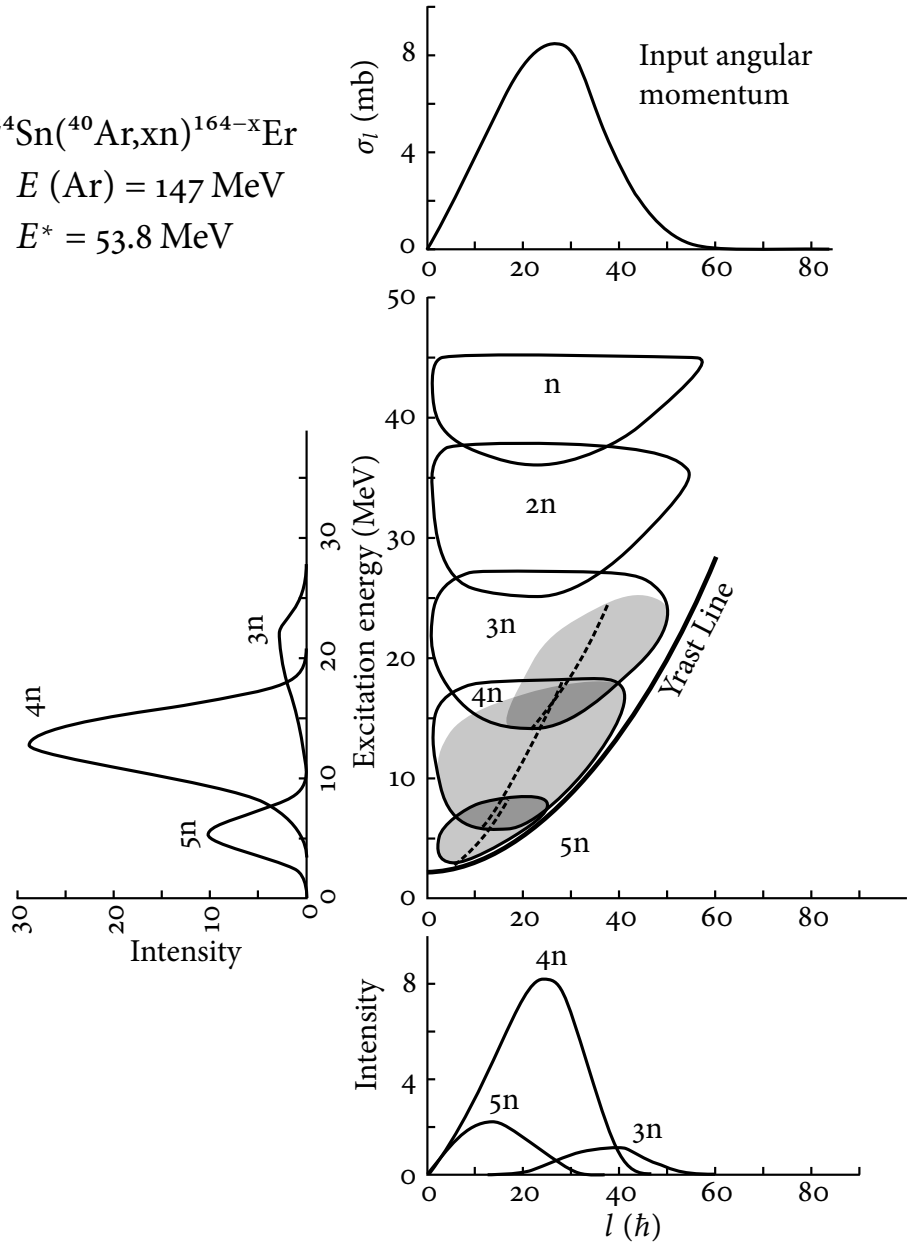

Figure 3.2 Statistical model calculations performed by Hillis et al. [39] for the reaction ^{124}Sn(^{40}Ar,xn)$^{164-x}$Er, displaying similar features to the reaction ^{110}Pd(^{48}Ti,xn)$^{158-x}$Er in the present experiment. The central plot indicates regions of spin versus excitation energy populated by the nucleus after the emission of 1–5 neutrons. Regions where γ decay competes with neutron emission are shown in grey, together with their predicted entry lines (dotted), and population intensity as a function of excitation energy (left) and spin (bottom).

tion that each group of γ rays (or *event*) incremented into a spectrum comprises a minimum number of γ rays with energies known to belong to the band of interest. This means that the detector system should be capable of detecting several γ rays emitted in rapid succession.

This was achieved using Gammasphere (pictured in Fig. 3.3), a spherical array of Compton-suppressed, high-purity germanium (Ge) detectors [42]. Gammasphere can accommodate up to 110 detectors with solid angle coverage of 47% of 4π [43]. 'Compton suppression' is the reduction of unwanted background events resulting from a γ ray Compton scattering out of the Ge detector, thereby failing to deposit all of its energy. The Ge detector is surrounded by bismuth germanate (BGO) scintillation detectors (Fig. 3.4) that pick up γ rays Compton scattering out of the Ge detector. A γ ray recorded in the Ge detector in coincidence with a γ ray in the BGO shield can be assumed not to have deposited its full energy and is excluded from the recorded data, drastically reducing the peak-to-background ratio of resulting spectra [44].

A total of 101 detectors were in use for the experiment. Most of those not used belonged to the foremost ring of detectors at 17.3°, which was removed for separate experiments involving the Fragment Mass Analyzer located down-beam from Gammasphere. The ^{110}Pd target foils were fixed to a target ladder at the centre of the target chamber, oriented at an angle of 27° to the vertical. The front of the Ge detectors are 25.4 cm from centre of the target chamber.

We have performed an efficiency calibration of the array using ^{182}Ta, ^{152}Er, ^{243}Am and ^{56}Co sources. A fitted curve is shown in Fig. 3.5, of the form

$$\varepsilon(E_\gamma) = \exp\left\{\left[(A + Bx + Cx^2)^{-G} + (D + Ey + Fy^2)^{-G}\right]^{-1/G}\right\}, \tag{3.1}$$

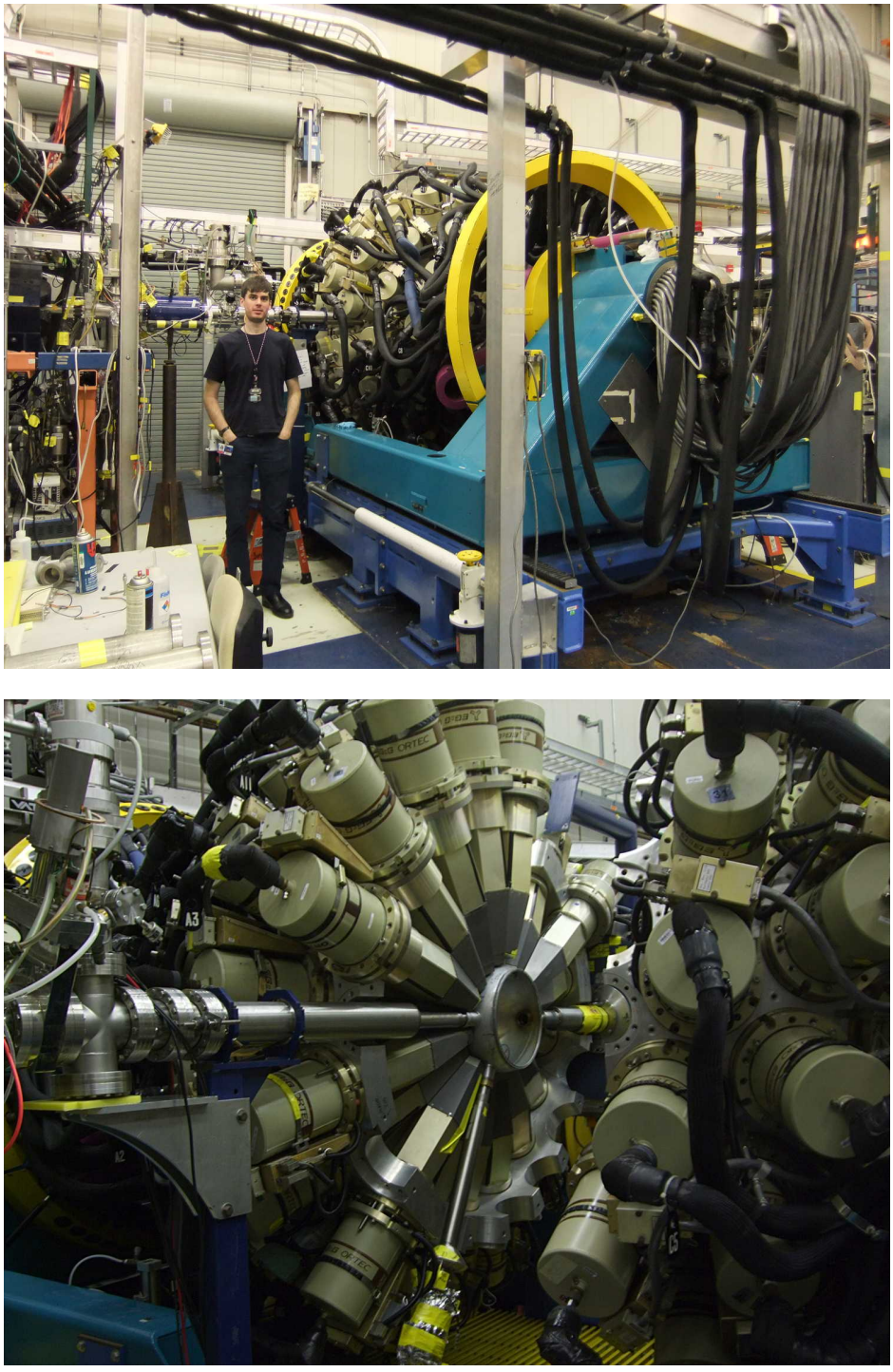

Figure 3.3 (Top) External view of Gammasphere. (Bottom) The two hemispheres of Gammasphere separated, exposing the detectors, the target chamber at the centre, the horizontal beam pipe and the target ladder mechanism entering the target chamber from below at an angle of 27° to the vertical.

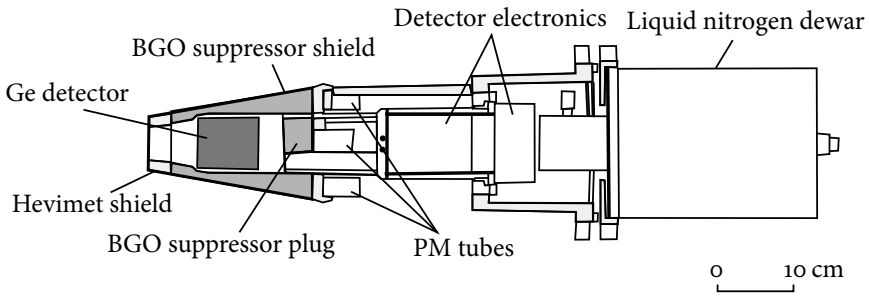

Figure 3.4 The main parts of a Gammasphere Ge detector module.

where $x = E_\gamma/100$ and $y = E_\gamma/1000$ with E_γ in keV, and A–G are the fitted parameters. While this calibration is not essential for the DSAM, it is needed to correctly measure the relative intensities of transitions, given in Chapter 4, which in turn provide an estimate of the intensity of side-feeding bands, shown in Fig. 3.18, in the Monte Carlo simulation used to fit Q_t.

Since the isolation of γ rays of interest requires several γ-ray energies in each event (at least four in the present analysis), the condition for the recording of an event was set to a minimum of four energies (*fold 4* events). This also has the practical advantage of minimising both the disk space required to store the experimental data, and the processing time needed to sort through it.

3.1.3 DSAM

Two targets were used in the present experiment. A thin target consisting of two stacked, self-supporting 500 μg/cm^2 ^{110}Pd foils was also used for a short time, allowing spectra to be directly compared with those of Lagergren et al., who used an identical target. Additionally, the absence of a gold backing means that the slowing of recoils is minimal and all γ rays are Doppler shifted to roughly the same extent, allowing coincidence relationships between ND and strongly deformed transitions

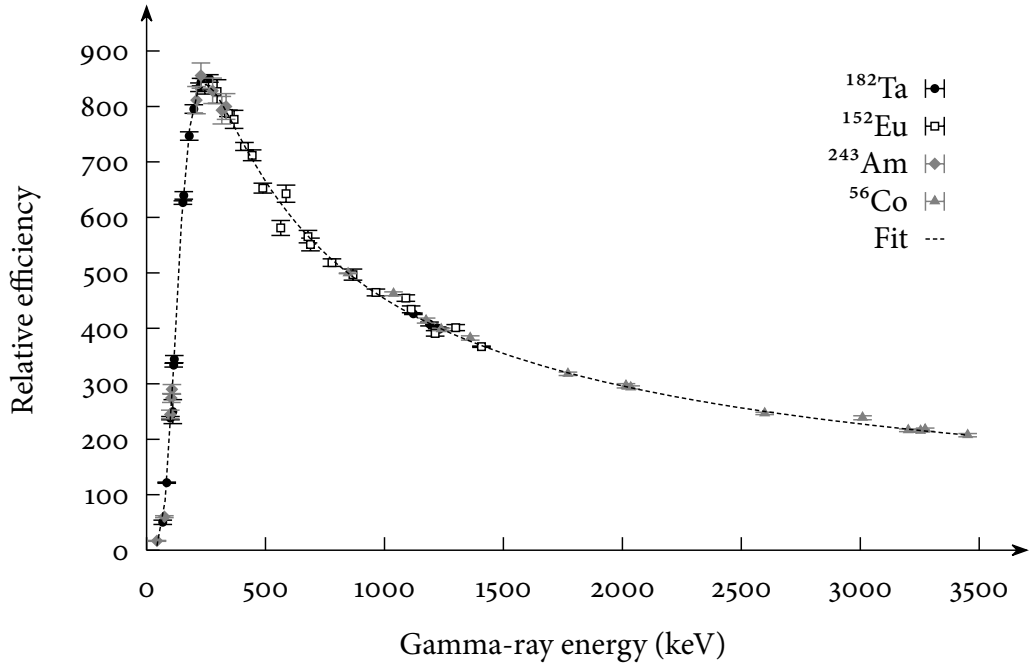

Figure 3.5 Fitted efficiency curve for the current experiment.

to be investigated (see Section 4.3).

The main target, used in the DSAM, consisted of a 1 mg/cm^2 layer of ^{110}Pd evaporated onto a 10 mg/cm^2 layer of ^{197}Au. A 0.07 mg/cm^2 layer of aluminium was placed between these two layers to prevent migration of palladium atoms into the gold backing due to heating of the target.

In the present 'centroid-shift analysis' version of the DSAM, the lifetimes of states in a strongly deformed band are derived from the velocity of the nucleus at the point when it emits γ rays from these states. A simulation of the slowing down process gives the time at which a particular velocity is reached. Hence, the lifetime of a state is obtained by subtracting the time at which the nucleus reached the state's decay velocity by the time at which it reached the previous state's decay velocity. These calculations are described in detail in Section 3.2.7.

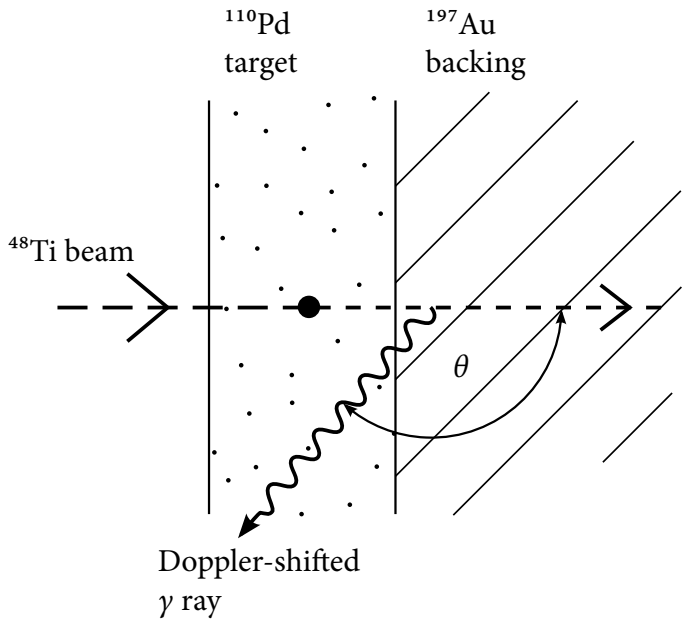

Figure 3.6 A schematic illustration of the DSAM. An incoming ^{48}Ti ion fuses with a ^{110}Pd target nucleus to form ^{158}Er, which evaporates four neutrons to become ^{154}Er. The recoil continues into the gold backing where it is slowed down to a stop while emitting γ rays.

The ability to measure lifetimes using this method therefore relies on the fact that, for lifetimes of the order 10^{-15} to 10^{-13} s, the recoil nucleus experiences a significant slowing down within the target between decays. It cannot be used to measure, for example, the much longer lifetimes of the ND states, since the nucleus has invariably slowed to a stop by the time these states decay.

Fig 3.6 is a schematic illustration of a recoil nucleus being created in the ^{110}Pd layer and emitting a γ ray at some angle θ to the beam direction. The velocity of the nucleus is measured from the Doppler shift of the emitted γ ray. A γ ray emitted from a nucleus travelling at velocity $\beta = v/c$ relative to the detector (where c is the

speed of light) has energy

$$E'_\gamma = \frac{E_{\gamma 0}}{\gamma(1-\beta)} \tag{3.2}$$

$$= E_{\gamma 0}\sqrt{\frac{1+\beta}{1-\beta}} \tag{3.3}$$

where E_0 is the γ-ray energy measured in the inertial frame of the nucleus and γ is the Lorentz factor $1/\sqrt{1-\beta^2}$. Performing a series expansion of Eq. 3.3 up to the first power of β and replacing β with $\beta\cos\theta$ (its component perpindicular to a detector at angle θ) one obtains

$$E'_\gamma = E_{\gamma 0}\,(1+\beta\,\cos\theta). \tag{3.4}$$

In the DSAM, β is commonly expressed as a fraction $F(\tau)$ of the initial velocity β_0, and so Eq. 3.4 becomes

$$E'_\gamma = E_{\gamma 0}\,(1+F(\tau)\,\beta_0\,\cos\theta). \tag{3.5}$$

An example of a Doppler-shifted peak, taken from the present data, is shown in Fig. 3.7. For $\theta = 90°$, the component of the beam velocity in the nucleus-to-detector direction is zero, and so detected γ rays are unshifted. For $\theta = 35°$ (a forward angle), a large component of the beam velocity points towards the detector, the γ-ray frequency is increased and $E'_\gamma = 1053$ keV, while the opposite is true of $\theta = 145°$ (a backward angle), for which $E'_\gamma = 1012$ keV.

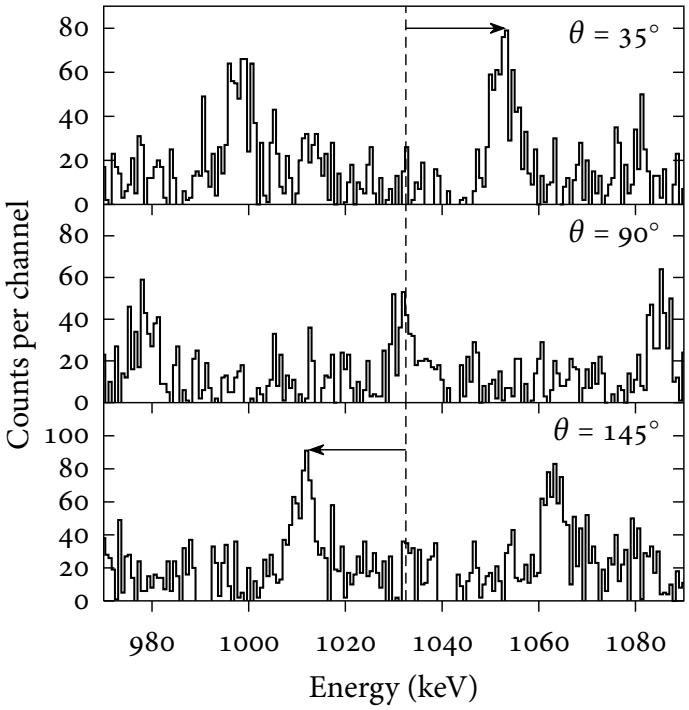

Figure 3.7 An example of a Doppler-shifted peak: the 1033 keV transition from band 1 of ^{154}Er seen at different detector angles.

3.2 DSAM analysis

A total of 3.9×10^9 events of fold four or higher were collected using the backed target over almost six days of beam time. Additionally, 8×10^8 events were collected using the thin target over $1\frac{3}{4}$ days of beam time. This section describes how Q_t values were extracted from the backed-target data.

3.2.1 Sorting

In order to measure the Doppler shift of transitions within a strongly deformed band, we must first sort the data to produce spectra containing those transitions. The ideal spectrum contains as little contamination as possible from transitions

outside the band, and as many counts as possible from those in the band.

This is difficult for strongly deformed bands in ^{154}Er, as the intensity of even the strongest band is only a small fraction of the intensity of the 4n decay channel. In the raw, unsorted spectrum containing all the individual γ-ray energies recorded in the experiment (the *full projection*), the peaks from the strongly deformed bands are completely obscured by the rest of the data, even when the energies are corrected to account for the broadening effect of Doppler shift.

This is where we can make use of the high fold of recorded events. In the sorting procedure, a sort program compares the γ-ray energies within each event with a list of energy gates corresponding to the γ rays in the band. Events with a minimum number of matching energies are kept, and the others rejected. In this way, we increase the proportion of events resulting from multiple decays within the band of interest.

The MTSORT package [45] was used to sort the data. The raw data were first presorted to remove any unwanted events or energies, i.e. events/energies detected outside of a given time window after the beam pulse, very low energies, and pileup. The presort also converted events from Gammasphere to Eurogam format [46]. Events in the latter format essentially comprised a list of detected γ rays, with each γ ray represented by its detector number and energy. The data were then re-sorted, with gating conditions applied, to produce the spectra used in the DSAM analysis.

The sort program used a 'spikeless' sorting method [47] to ensure that each γ-ray energy is incremented only once into any particular spectrum.[1] The basic procedure followed by the sort program is shown in Fig. 3.8.

[1] This is an alternative to sort methods in which higher-fold events are first 'unpacked' into lower-fold sub-events. Each γ ray then appears in multiple sub-events, creating the possibility that it will be incremented into a spectrum more than once.

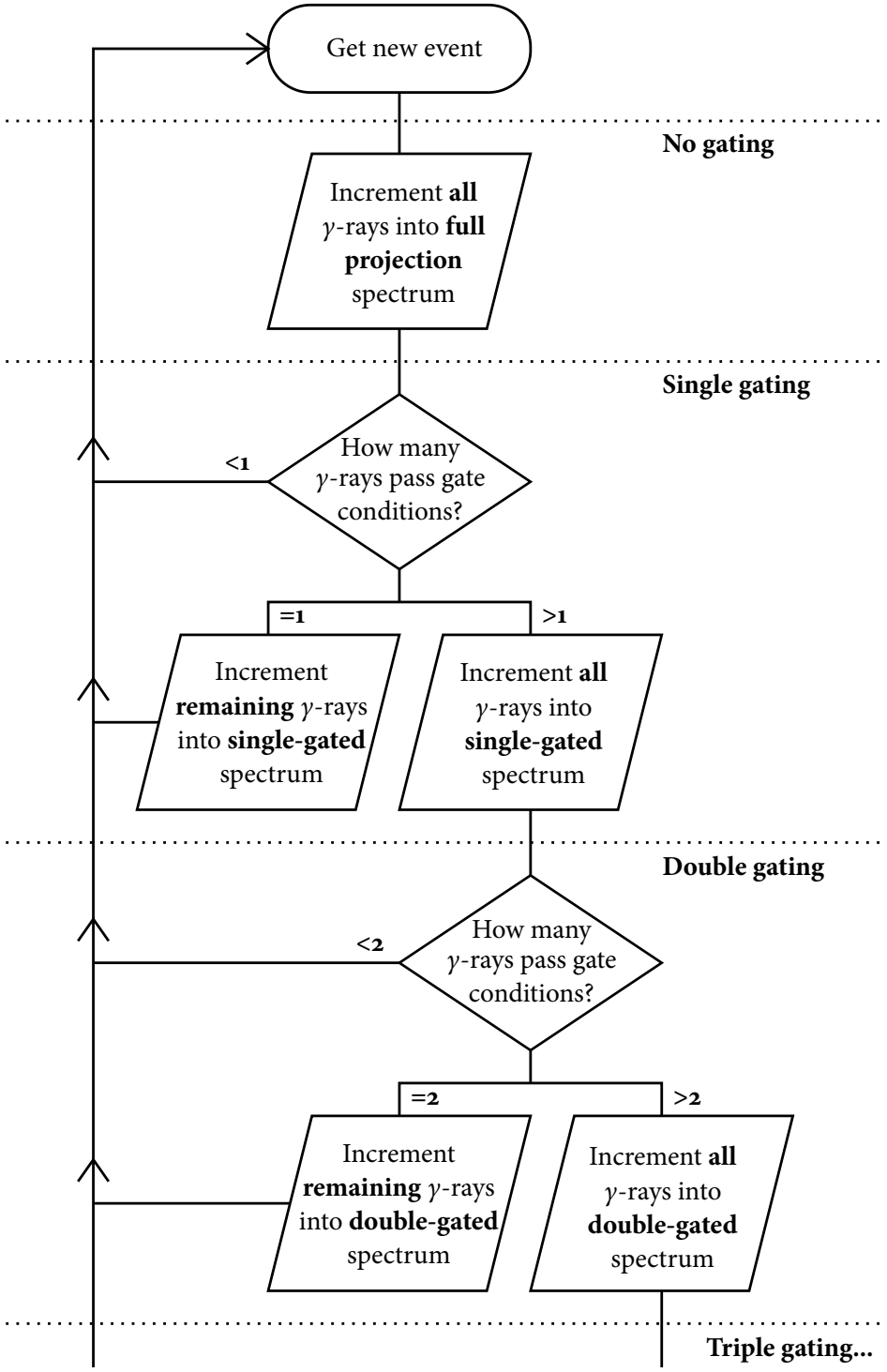

Figure 3.8 Flowchart depicting the procedure followed by the sort program using the spikeless sorting method.

Fig. 3.9 shows the effect of an increasing number of successive gates, corresponding to the energies of band 1 in ^{154}Er, applied to the experimental data. With each gate added, the intensities of the peaks of interest increase relative to the background and the other peaks in the spectrum.

Obtaining the best quality spectra for analysis required the optimisation of three parameters: the number of gates, gate width and Doppler correction. Although increasing the number of gates will increase the number of counts in the spectra, gates with $E_\gamma \lesssim 875$ keV are in a region of high contamination, so we must take care that their inclusion is not counteractive. For the final spectra, 13 gates were used with energies 735–1300 keV.

We can apply similar reasoning to the choice of gate width. Increasing the gate width beyond a certain value has a detrimental effect on spectrum quality, such that it is preferable to exclude the low-intensity tails of the peaks from the gate range. A width of 18 channels (≡ 6 keV) was used for the final spectra.

Finally, a Doppler correction must be applied to the gates, since the positions of the peaks being gated on vary with detector angle. In the MTSORT language this is more easily achieved in reverse, i.e. a single unshifted gate is declared for each transition, while a Doppler correction,

$$E_{\gamma 0} = \frac{E'_\gamma}{1 + \beta \cos\theta}. \tag{3.6}$$

is applied to each γ-ray energy E'_γ before it is tested against the gate list. For band 1, an optimum value of $\beta \sim 0.0243$ was determined by observing the variation in peak area for a range of values (see Fig. 3.10).

More sophisticated methods were also tested to try and match the Doppler cor-

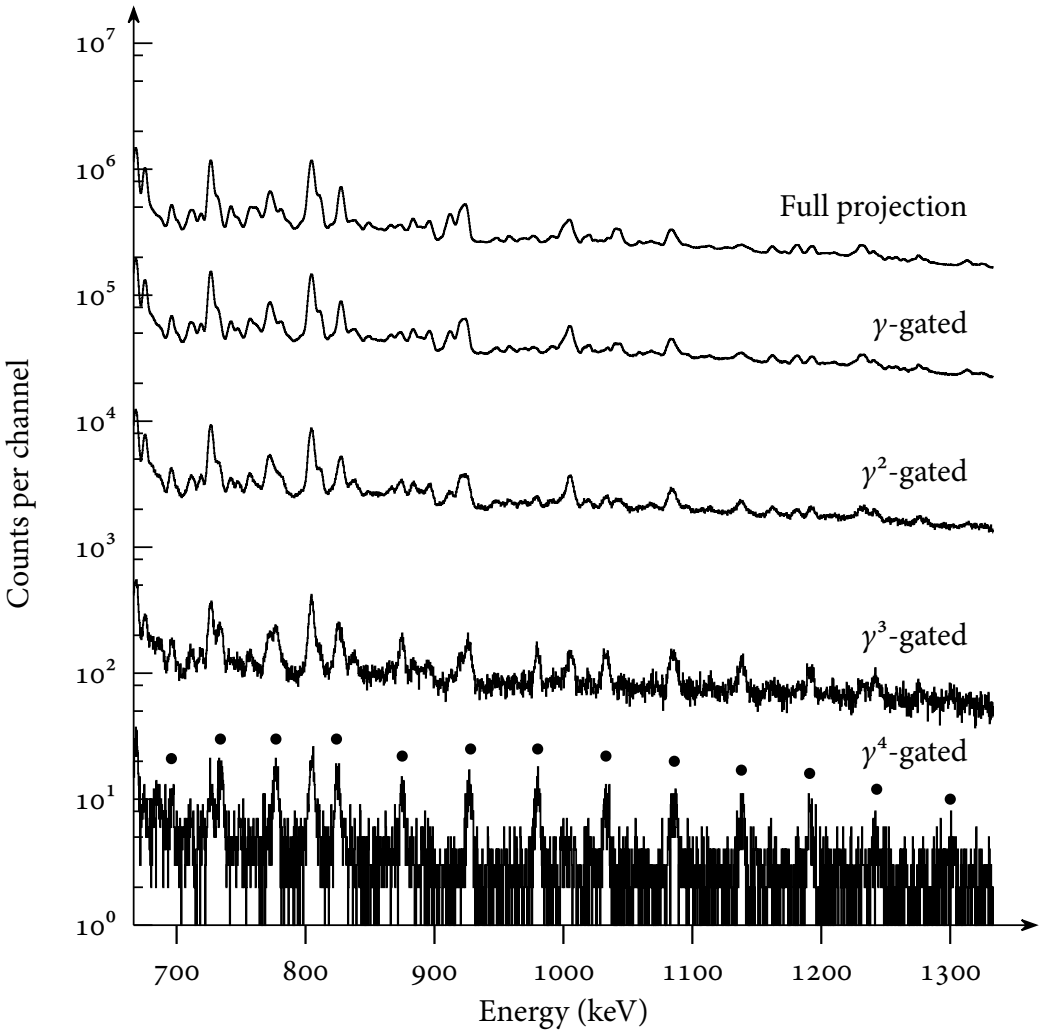

Figure 3.9 Doppler-corrected spectra for band 1 of ^{154}Er (black points) resulting from multiple-fold gating of the thin-target data.

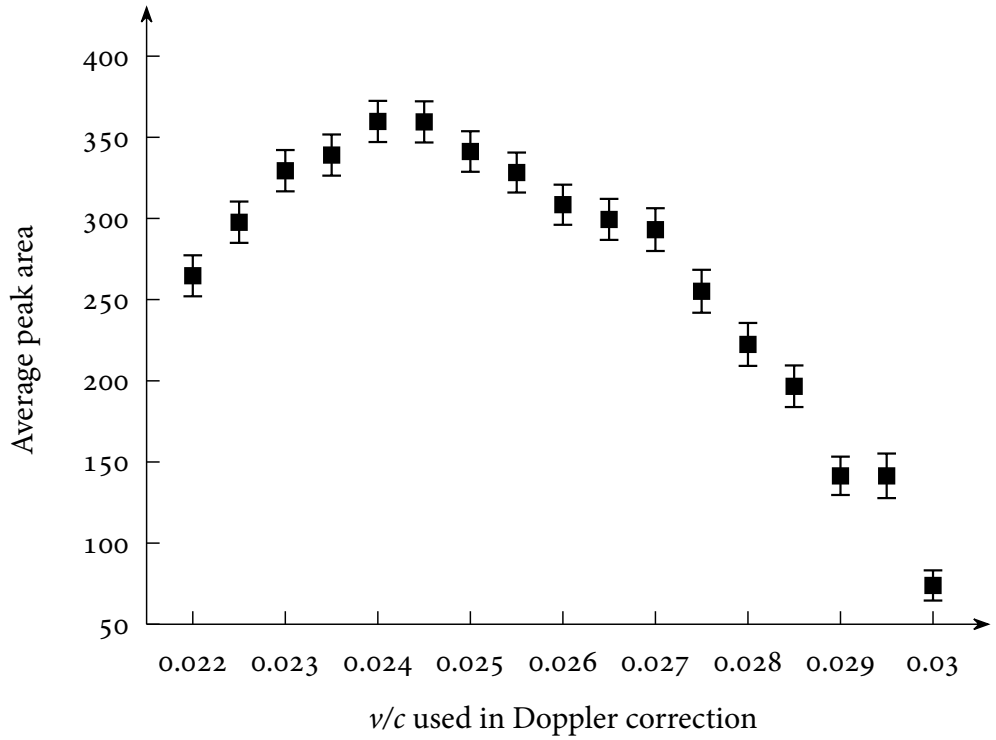

Figure 3.10 The variation of average peak area of band 1 of ^{154}Er (734–1243 keV transitions) with the Doppler correction applied by the sort program. Peaks were fitted using the procedure described in section 3.2.3.

rection more closely with the experimentally observed decrease in Doppler shift with decreasing spin (and hence γ-ray energy). The optimum *constant* Doppler correction is merely an average of the $F(\tau)$ values of the gated transitions. An *energy-dependent* Doppler correction that follows the experimental $F(\tau)$ curve should therefore produce better spectra.

To this end, two alternative sort methods were tested. The first used an energy-dependent function of the form

$$F(E_\gamma) = 1 - \frac{a}{1 + e^{(E_\gamma - b)/c}} \tag{3.7}$$

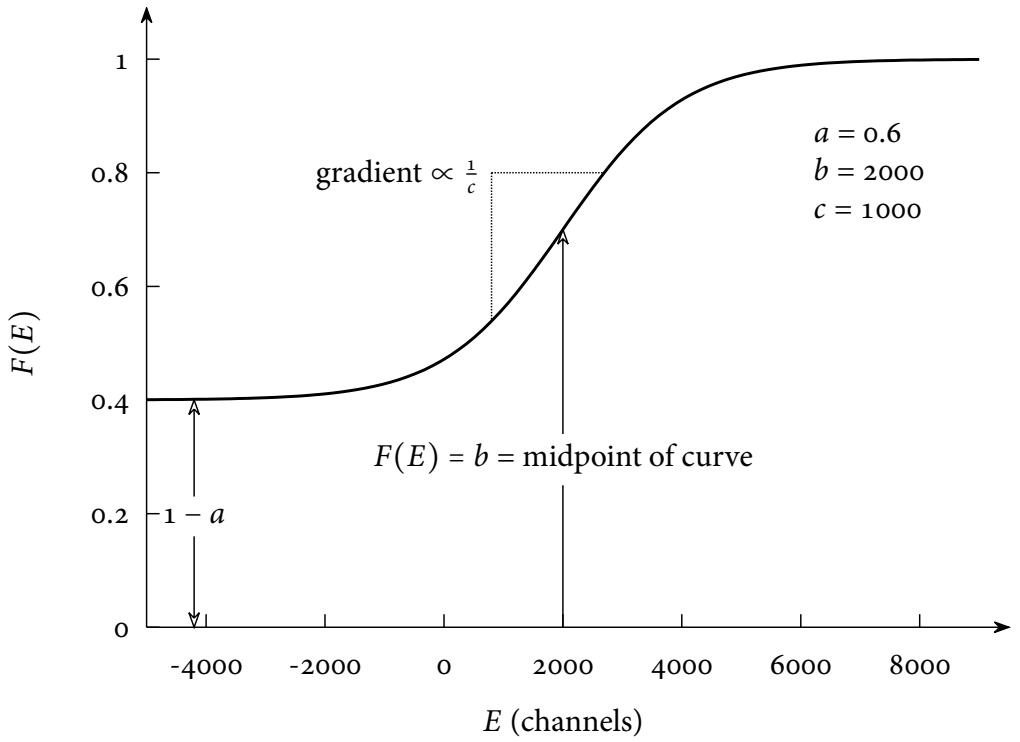

Figure 3.11 The function described by Eq. 3.7 with parameter values $a = 0.6$, $b = 2000$ and $c = 1000$.

where a, b and c are parameters determining the shape of the curve (Fig. 3.11). The problem with this approach is that the Doppler-shift equation becomes

$$E'_\gamma = E_{\gamma 0}\left(1 + F(E_{\gamma 0})\ \beta\ \cos\theta\right) \tag{3.8}$$

and so the Doppler correction, equivalent to Eq. 3.6, becomes:

$$E_{\gamma 0} = \frac{E'_\gamma}{1 + F(E_{\gamma 0})\ \beta\ \cos\theta}. \tag{3.9}$$

But $F(E_{\gamma 0})$ is not known. One could instead use the approximation

$$E_{\gamma 0} \approx E''_\gamma = \frac{E'_\gamma}{1 + F(E'_\gamma)\ \beta\ \cos\theta}. \tag{3.10}$$

However, for forward angles $E'_\gamma > E_{\gamma 0}$ and so $F(E'_\gamma) > F(E_{\gamma 0})$. E'_γ is therefore over-corrected, i.e. $E''_\gamma < E_{\gamma 0}$. For backward angles $E'_\gamma < E_{\gamma 0}$, therefore $F(E'_\gamma) < F(E_{\gamma 0})$ and E'_γ is under-corrected, but again this leads to $E''_\gamma < E_{\gamma 0}$.

This problem can be solved by noting that E''_γ is nevertheless closer to $E_{\gamma 0}$ than is E'_γ, which in turn means that $F(E''_\gamma)$ is a better approximation of $F(E_{\gamma 0})$ than is $F(E'_\gamma)$, and in practice

$$E_{\gamma 0} \approx \frac{E'_\gamma}{1 + F(E''_\gamma)\ \beta\ \cos\theta} \tag{3.11}$$

is correct to well within ⅓ keV.

A second sort method is to leave the γ-ray energies uncorrected and shift the gates according to detector angle. While a list of one-dimensional gates cannot be modified in MTSORT, the set of all shifted gates can be calculated beforehand to construct two-dimensional gates in channel vs. ring number 'space', e.g.,

```
GATEMAP 2D gates1[8192,18]
(2234 2  2232 3  2224 4  2219 5  2210 6  2203 7  2202 8
 2195 9  2187 10 2185 11 2177 12 2169 13 2164 14 2157 15
 2154 16 2149 17 2167 17 2172 16 2175 15 2182 14 2187 13
 2195 12 2203 11 2205 10 2213 9  2220 8  2221 7  2228 6
 2237 5  2242 4  2250 3  2252 2)
```

for the 734 keV gate. The numbers in parentheses consist of pairs of channel numbers and ring numbers, respectively. Together, these points describe a polygonal 2D gate, against which both γ-ray energy and ring number were tested in-sort.

The two sort methods are, in principle, equivalent and indeed produce similar results. However, the latter method is somewhat faster as it does not need to perform a Doppler correction calculation each time a γ-ray energy is tested. It is also more flexible since the Doppler shift of each gate can take on any value rather than that determined by a function. Nevertheless, Eq. 3.11 is useful for producing a Doppler-corrected spectrum once an event has passed the gating conditions.

3.2.2 Background subtraction

While the γ^4-gated spectrum in Fig. 3.9 is the cleanest, it contains ~1 order of magnitude fewer counts than the γ^3-gated spectrum. Indeed, a more precise centroid measurement may be made using the γ^3-gated spectrum following the subtraction of a background spectrum, such that the number of counts in channel i of the final spectrum S is given by

$$S_i = U_i - fB_i, \tag{3.12}$$

where U_i and B_i are the number of counts in the i^{th} channel of the unsubtracted and background spectra, respectively, and f is a normalisation factor to ensure a flat background of $\sim$ 0 counts in the final spectrum. The γ^{n-1}-gated spectrum usually provides a good background spectrum for the γ^n-gated spectrum, being of a similar shape to the latter except for the peaks of interest, which are weaker. Thus, these peaks are accentuated in the resulting spectrum (see Fig. 3.12).

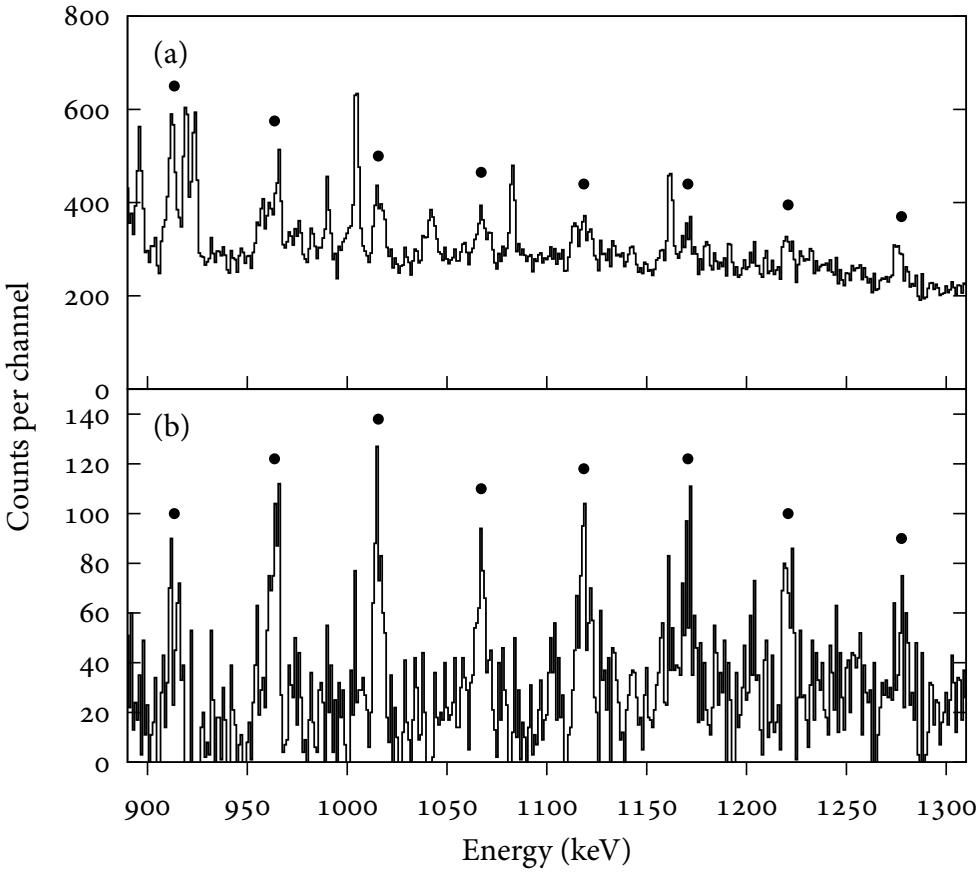

Figure 3.12 γ^3-gated spectra for band 1 of ^{154}Er (black points) at detector angle 130° (a) before background subtraction and (b) after the subtraction of the corresponding γ^2-gated spectrum with a normalisation factor of 4%.

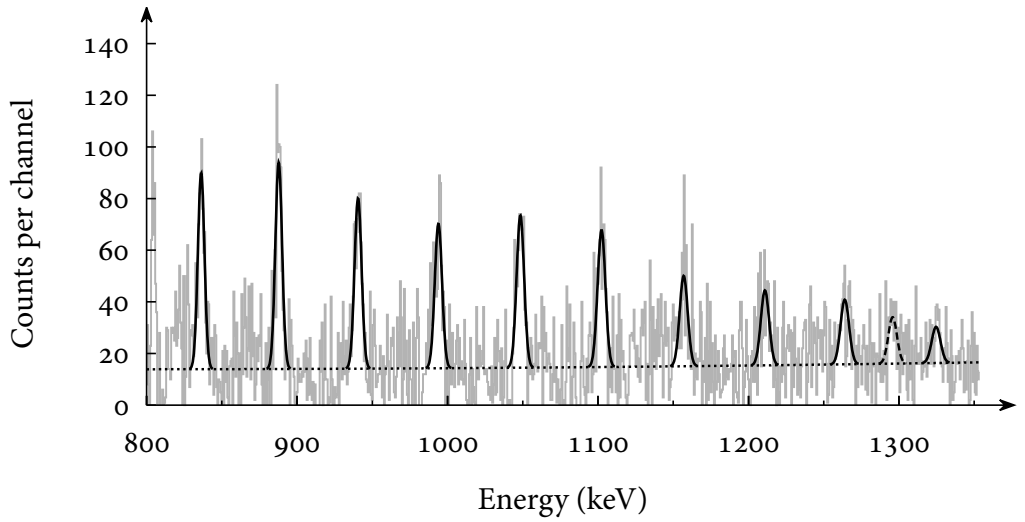

Figure 3.13 A typical fit to a spectrum (grey line). Each peak is fitted with a Gaussian function (solid black line), while a quadratic function (dotted line) is fitted to the background. An additional peak (dashed line) not belonging to the band was included to obtain the correct background fit.

3.2.3 Centroid measurement

Once sufficiently clean spectra were obtained, the centroids of the in-band transitions were measured in the one-dimensional spectrum analysis program GF3 [48], which is part of the RADWARE software package. Centroids were measured by fitting a Gaussian to each peak, as in Fig. 3.13. To obtain a true fit with correct errors, weighting spectra [48] were first produced according to

$$W_i = U_i + f^2 B_i \tag{3.13}$$

where W_i is the number of counts in the i^{th} channel of the weighting spectrum and U_i, B_i and f are as defined in Eq. 3.12.

3.2.4 Doppler shift calculation

This section describes how the Doppler shift of each transition was calculated from the measured centroids using a linear least-squares fit. The χ^2 of some of the fits was found to be quite high, which in bands 1 and 2 was due to the presence of one or two outliers. Although the inclusion of these points does not greatly influence the fitted Doppler shifts, the difficulty of fitting Q_t values to these Doppler shifts in later sections warrants the need for extra care to ensure that their accuracy is not in doubt. As such, criteria were applied to test for outliers, which in some cases were deleted from the data.

For band 3, where the quality of the spectra was much lower than for bands 1 and 2, removing a single outlier was in one case not sufficient to lower the χ^2 of the fit to an acceptable value. A more robust fitting procedure known as *jackknifing* is introduced in this section to deal with this case.[2]

The angles of certain pairs of detector rings are close enough for there to be little difference in the Doppler shifts of the γ rays they detect. As such, the spectra from these pairs of rings were summed together, producing spectra with an effective angle θ_{eff} of

$$\cos(\theta_{\text{eff}}) = \frac{N_1 \cos(\theta_1) + N_2 \cos(\theta_2)}{N_1 + N_2} \tag{3.14}$$

where N_1 and N_2 are the total number of counts measured in the full projection spectrum at angles θ_1 and θ_2, respectively. The effective angles are summarised in Table 3.1.

Once all the centroids for a particular transition have been measured, $F(\tau)$ for

[2] The jackknife method will also be applied in the parametric fit of Q_t to produce sensible errors.

Ring	θ (°)	θ_{eff} (°)
1[a]	17.3	17.3
2	31.7	35.3
3	37.4	
4	50.1	50.1
5	58.3	58.3
6	69.8	69.8
7	79.2	79.9
8	80.7	
9	90.0	90.0
10	99.3	100.1
11	100.8	
12	110.2	110.2
13	121.7	121.7
14	129.9	129.9
15	142.6	145.2
16	148.3	
17	162.7	162.7

[a]Ring 1 detectors not used in experiment.

Table 3.1 Detector angle θ for each ring of Gammasphere and mean detector angle θ_{eff} after summing of the indicated rings.

that transition can be calculated. Rearranging Eq. 3.5 slightly, we obtain

$$E'_\gamma = E_{\gamma 0}\, F(\tau)\, \beta_0\, \cos\theta + E_{\gamma 0}, \tag{3.15}$$

from which it can be seen that a plot of centroid energy vs. $\cos\theta$ should produce a straight line with gradient $E_{\gamma 0}\, F(\tau)\, \beta_0$ and intercept $E_{\gamma 0}$. Hence,

$$F(\tau) = \frac{\text{gradient}}{\beta_0 \times \text{intercept}}. \tag{3.16}$$

A weighted least-squares fit was applied to the data in order to determine these

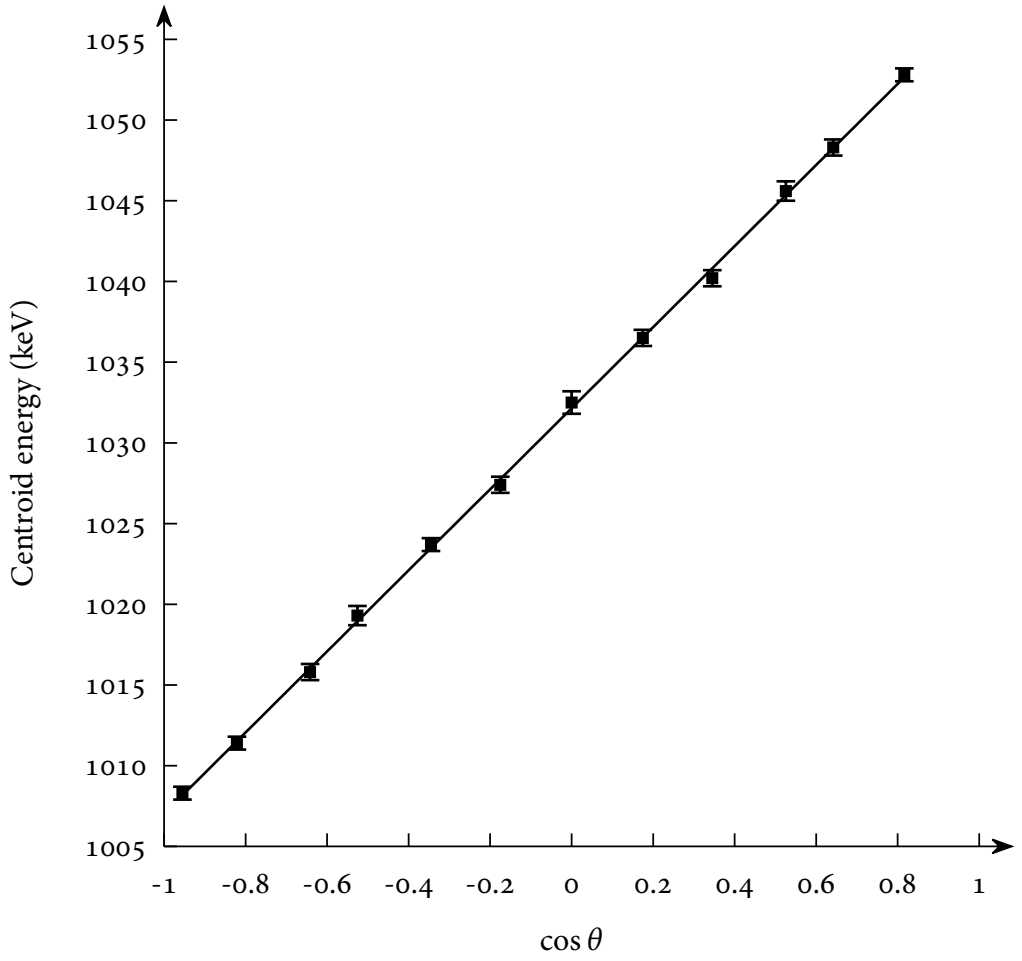

Figure 3.14 A weighted least-squares linear fit (solid line) of centroid energy vs. $\cos\theta$ data (squares) for the 1033 keV transition in band 1.

quantities. An example is shown in Fig. 3.14.

All the centroids in Fig. 3.14 lie close to the best-fit line. The χ^2 of the fit is

$$\chi^2 = \sum_N \frac{[y_i - y(x_i)]^2}{{\sigma_i}^2}, \tag{3.17}$$

where y_i is the independent variable (in this case E'_γ), x_i is the dependent variable (here, $\cos\theta$), $y(x_i)$ is the value predicted by the fit and σ_i is the error on y_i. For

the case of the 1033 keV transition in the figure, $\chi^2 = 3.8$. The probability that χ^2 exceeds this value for the given number of degrees of freedom ν, or $P(\chi^2 \geq \chi^2_{\text{fit}}, \nu)$, is an indicator of the goodness of the fit. For 1033 keV, $P = 0.96$. The ideal value for P is 0.5, so the errors in this particular fit may have been over-estimated.

In Fig. 3.15a, by contrast, one of the data points deviates much more from the best-fit line than the rest. As a result, $\chi^2 = 23.3$ and $P = 0.01$. The minimum acceptable value of P is conventionally 0.05 and so, if we adopt this standard, the fit must be rejected. It is tempting to immediately dismiss the deviating point as an outlier – possibly due to contamination in the spectrum or a random fluctuation in the background – and delete it from the data set.

However, the situation is less clear in other cases, such as 1206 keV in band 2 (Fig. 3.15b). Again, the fit has a low P-value ($P = 0.007$), but this time there is no single obvious outlier. The need arises for a systematic method of outlier rejection, and indeed there exist a number of tests to identify outliers. Although some tests are more sophisticated than others, there is no absolute definition of an outlier, so all tests are essentially based on some arbitrary rule.

One relatively simple test is Chauvenet's criterion [49, 50]. This criterion states that if the expected number of measurements that are at least as deviant as the measurement being tested is less than one-half, then that measurement can be considered for rejection. This number can be expressed as

$$n = N \times \text{erfc}\left(\frac{|y_i - y(x_i)|}{\sqrt{2}\sigma_i}\right), \tag{3.18}$$

where N is the number of measurements in the data set and erfc is the complimentary error function.

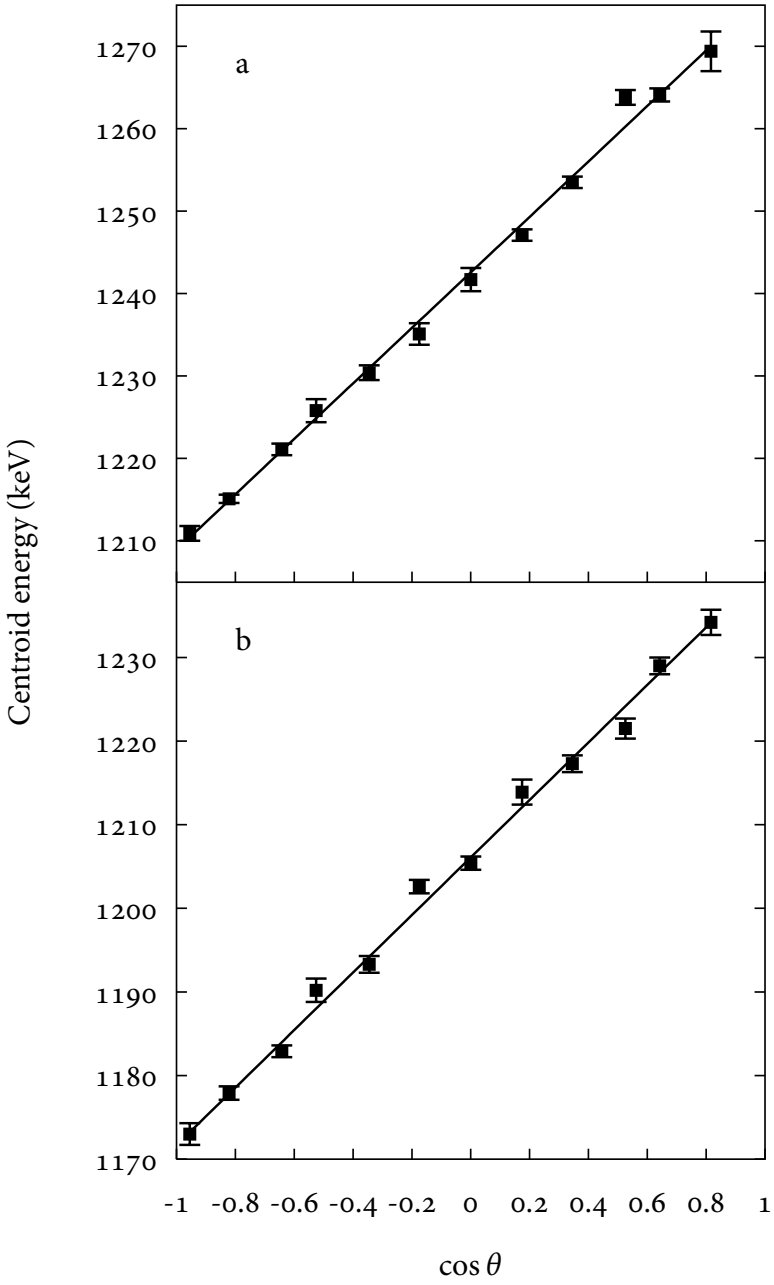

Figure 3.15 A weighted least-squares linear fit (solid line) of centroid energy vs. $\cos\theta$ data for (a) the 1243 keV transition in band 1 and (b) the 1206 keV transition in band 2. Both fits have an unacceptably large χ^2.

E_γ (keV)	P-value
Band 1	
824	0.05
875	0.14[a]
928	0.28
980	0.08
1033	0.96
1086	0.07
1138	0.20
1191	0.24
1243	0.90[a]
1300	0.50
Band 2	
878	0.23
924	0.23
971	0.14
1018	0.28
1064	0.13[a]
1112	0.60[a]
1159	0.18
1206	0.18[a]

[a] One outlier deleted from data.

Table 3.2 Probabilities associated with linear fits to bands 1 and 2

We have applied Chauvenet's criterion to the data conservatively, i.e. only if $P < 0.05$. For the transitions in bands 1 and 2, the deletion of the data point with the highest χ^2 was in all cases sufficient to raise P above 0.05. The final P-values for these two bands are summarised in Table 3.2.

The spectra for band 3 were of much lower quality than those of bands 1 and 2 and were therefore harder to fit peaks to. As a result, the deletion of the data point with the largest χ^2 was sometimes not enough to bring P above 0.05. For the 898 keV transition, a visible contamination peak at ~ 921 keV was deemed to

E_γ (keV)	Comments	Error on β (10^{-3})
847		1.9
898	Three outliers deleted	0.4
951		0.6
1005	One outlier deleted	0.6
1059	One outlier deleted	0.8
1114		0.7
1169	Jackknife	2.8
1223		0.8

Table 3.3 Error on $\beta(= F(\tau)\beta_0)$ for the transitions in band 3, indicating where the jackknife method has been used or outliers have been deleted from the data.

be the cause of high-χ^2 points at forward detector angles, and three points were deleted from the fit. For the 1169 keV transition, however, deviant points were not localised around a particular part of the spectra, so the same reasoning could not be applied. Deleting a second data point based purely on its deviation from the fit is generally discouraged [49, 50], so for this point the *jackknife* method of error estimation [51, 52] was employed. The method was used in this work principally to determine the errors on Q_t, and so it is discussed in more detail in Section 3.2.9. 'Jackknifing' generally results in a larger error on β than the conventional estimate (see Table 3.3), ensuring that the β values calculated from the poor fit to the 1169 keV centroids are given less weight in the final Q_t fit.

3.2.5 Calculation of β_0

We can see from Eq. 3.16 that the initial velocity of the nucleus, β_0, is needed to calculate $F(\tau)$. In previous DSAM experiments, a satisfactory β_0 has been obtained from a straightforward calculation using the theoretical stopping power for the

beam in the target, and the target thickness. This calculation is presented in the current section. However, evidence will be presented in Section 3.2.7 suggesting that this theoretical value is incorrect, and an alternative value of β_0 will be proposed.

In the theoretical calculation, it is assumed that the average recoil nucleus is produced in the centre of the target. The beam energy at this position is

$$E_{\mathrm{b,mid}} = E_0 - \frac{d}{2}\frac{\mathrm{d}E}{\mathrm{d}x} \tag{3.19}$$

where E_0 is the initial beam energy, d is the thickness of the target layer and $\mathrm{d}E/\mathrm{d}x$ is the theoretical stopping power for the beam ion in the target, which is assumed not to vary significantly over the range of beam energies involved. By conservation of angular momentum and using a non-relativistic approximation,

$$m_{\mathrm{b}}v_{\mathrm{b}} = m_{\mathrm{c}}v_{\mathrm{c}} = (m_{\mathrm{b}} + m_{\mathrm{t}})v_{\mathrm{c}} \tag{3.20}$$

where m is mass, v is velocity and the subscripts b, t and c signify the beam, target and compound nuclei, respectively. The beam energy is equal to

$$E_{\mathrm{b}} = \tfrac{1}{2}m_{\mathrm{b}}v_{\mathrm{b}}^2 \tag{3.21}$$

$$\Rightarrow v_{\mathrm{b}} = \sqrt{2E_{\mathrm{b}}/m_{\mathrm{b}}}. \tag{3.22}$$

Substituting Eq. 3.22 into Eq. 3.20,

$$m_b\sqrt{2E_b/m_b} = (m_b + m_t)v_c \tag{3.23}$$

$$\Rightarrow v_{c,mid} = \frac{\sqrt{2E_{b,mid}m_b}}{m_b + m_t}. \tag{3.24}$$

The ^{158}Er compound nucleus must lose four neutrons to become ^{154}Er, with each emitted neutron carrying away some kinetic energy in the centre-of-mass frame. This means that individual recoils will in general have a velocity different from $v_{c,mid}$. However, evaporated neutrons are assumed to be emitted in all directions with equal probability in the centre-of-mass frame, meaning that the *average* recoil velocity in the lab frame *is* equal to $v_{c,mid}$, and so $\beta_0 = v_{c,mid}/c$.

Using the theoretical dE/dx calculated by the program SRIM 2008 by Ziegler [53] in Eq. 3.19, one obtains $\beta_0 = 0.02933$. $F(\tau)$ for all measured transitions can then be calculated from Eq. 3.16.

3.2.6 Monte Carlo simulations

This section describes how the Monte Carlo program SRIM was used to simulate the slowing down of several thousand recoil nuclei in the target. The data obtained from this simulation were used to fit the parameters Q_t, Q_{sf} and T_{sf} using a χ^2-minimisation program, as described in Section 3.2.7.

SRIM allows the initial positions, energies and directions of individual ions to be specified by an input file. This means that the simulated ions can have different values of these parameters, as they would in the experiment. The first step is therefore to generate the desired number of ions, each with an energy, position and

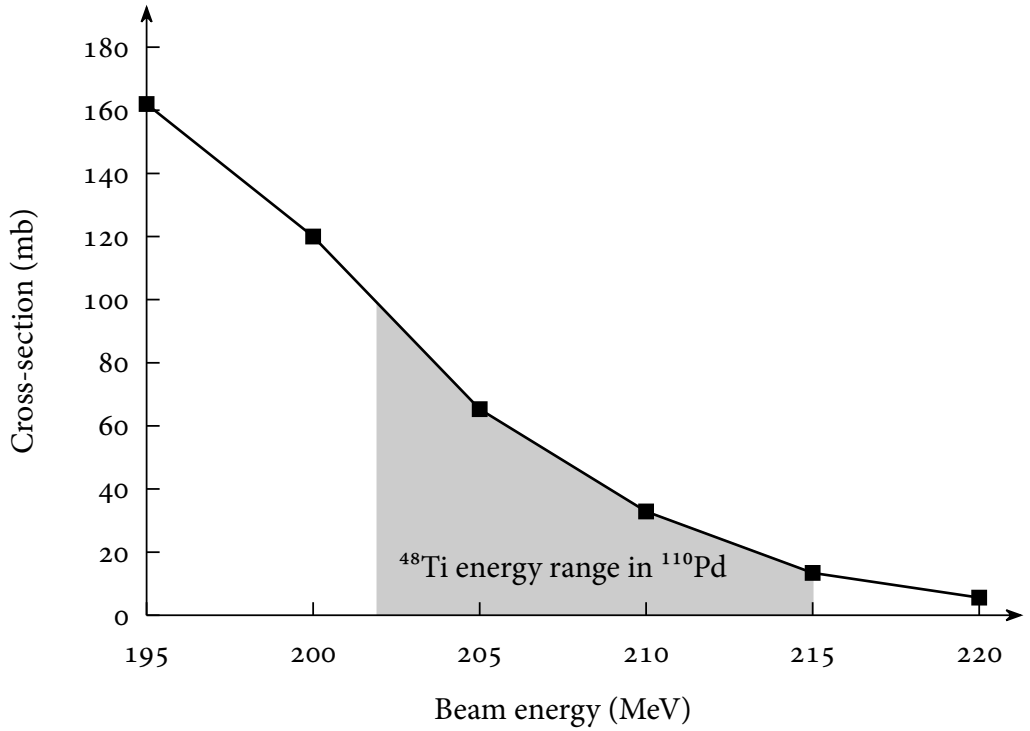

Figure 3.16 The cross-section for the reaction ^{110}Pd(^{48}Ti,4n)^{154}Er calculated by PACE, together with the calculated energy range of the beam in the target layer.

velocity chosen randomly from an appropriate distribution.

First, the reaction beam energy is selected from a probability distribution that follows the specified reaction cross-section (Fig. 3.16), giving an initial β from Eq. 3.24. For previous DSAM analyses performed by the collaboration, the cross-section profile has not been taken account (i.e. the reaction is assumed to occur with equal probability at all beam energies) without causing any apparent problems. This assumption was used to calculate the preliminary results presented in Section 3.2.7. However, it will be shown in Section 3.2.8 that the reaction cross-section must have a strong influence on the initial recoil velocity and therefore should be taken into account.

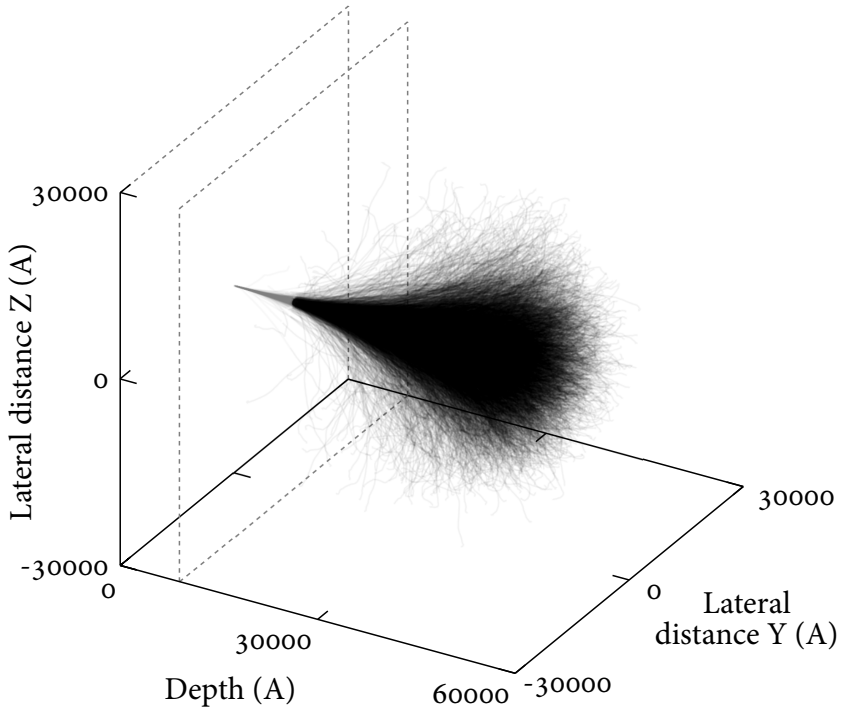

Figure 3.17 The paths of 10000 simulated recoils generated by SRIM. The grey dashed and solid lines delineate the ^{110}Pd target layer and the paths through it, respectively.

The chosen beam energy corresponds to a unique target depth (cf. Eq. 3.19), giving the initial recoil position. Four neutrons are then evaporated with energies chosen randomly from a Maxwellian distribution (see e.g. [54, p. 931]). Momentum conservation is applied to give the residual nucleus a 'kick' after each evaporation, changing its velocity by a small amount in a direction that is, likewise, randomly chosen, this time from an isotropic probability distribution. This has the effect of widening the 'cone' of recoils in the target (Fig. 3.17).

The next step is to run the SRIM simulation. The program calculates the paths of the nuclei as they slow down in the target and backing. The stopping power of a

material is the sum of its nuclear and electronic stopping powers,

$$\frac{\mathrm{d}E}{\mathrm{d}x} = \left(\frac{\mathrm{d}E}{\mathrm{d}x}\right)_{\mathrm{n}} + \left(\frac{\mathrm{d}E}{\mathrm{d}x}\right)_{\mathrm{e}}, \tag{3.25}$$

resulting from interactions with atomic nuclei and electrons, respectively. Following each interaction, the energy and position of the recoil are recorded. When the simulation is complete, energy and position are translated into velocity and time via kinematic calculations. In this way, the velocity of every simulated recoil at any time from its creation can be 'looked up' for the χ^2-minimisation calculations described in the next section.

3.2.7 A preliminary fit of Q_t

This section describes how the decays of the simulated recoils were modelled in order to calculate a theoretical $F(\tau)$ curve, and how a χ^2 minimisation procedure was used to determine the values of the model parameters that produce the best fit to the data. However, we will see that the values obtained are physically unrealistic, and that certain assumptions must be made to get around the problem.

With each iteration of the χ^2 minimisation program, MLTFIT [55], a trial value of each fit parameter is compared with the experimental results. This is done by calculating the decay time of each transition from the parameter values, and then looking up the nucleus' β at those times in SRIM's output. $F(\tau)$ is then simply β/β_0.

Fig. 3.18 is a schematic of the decay scheme used to model the feeding and subsequent decay of band 1. The main band, which has transition quadrupole moment Q_t, is fed by several bands with an average transition quadrupole moment Q_{sf}. Energies in the side-feeding bands are calculated from Eq. 2.25 assuming that

the bands' $\mathcal{J}^{(2)}$ moment of inertia is equal to that of the states being fed. A side-feeding delay, T_{sf}, is included to represent any decay of states above those modelled.

MLTFIT uses the trial Q_t together with input information on the transition energies and relative intensities within the band to calculate τ for each state using Eq. 2.29. The same is done for the side-feeding bands using Q_{sf}. To simulate decay times in an individual nucleus, MLTFIT selects a random side-feeding band from which to begin, and then generates a random decay time for each consecutive state based on its average lifetime τ. Finally, the $F(\tau)$ of the nucleus for each state at the time of its decay is looked up from the SRIM data and added to a running average for that state. In this way, the program is able to calculate an average $F(\tau)$ curve for a large set of nuclei with realistic formation and decay properties.

When the calculation is complete, the χ^2 of the trial parameters is calculated using Eq. 3.17 with the experimental and simulated $F(\tau)$ in place of y_i and $y(x_i)$, respectively. The calculation is then repeated with different parameter values while a χ^2 minimisation algorithm attempts to find the Q_t, Q_{sf} and T_{sf} that give the lowest χ^2. MLTFIT uses both the SIMPLEX and MIGRAD algorithms from the MINUIT statistical analysis package [56].

Once the best-fit parameters have been obtained, their uncertainties must be calculated. For a multi-parameter fit, this can be done by noting that an increase in the χ^2 of 1 from χ^2_{min} is equivalent one standard deviation [50, p. 211]. Hence, in a surface plot of χ^2 for parameter values around χ^2_{min}, the uncertainties are delimited by the $\chi^2_{min} + 1$ contour (Fig. 3.19). For simplicity, Fig. 3.19 shows the case for only two free parameters, Q_t and Q_{sf}. The full $\chi^2_{min} + 1$ contour, taking into account T_{sf}, is three-dimensional and produces larger errors on Q_t and Q_{sf}.

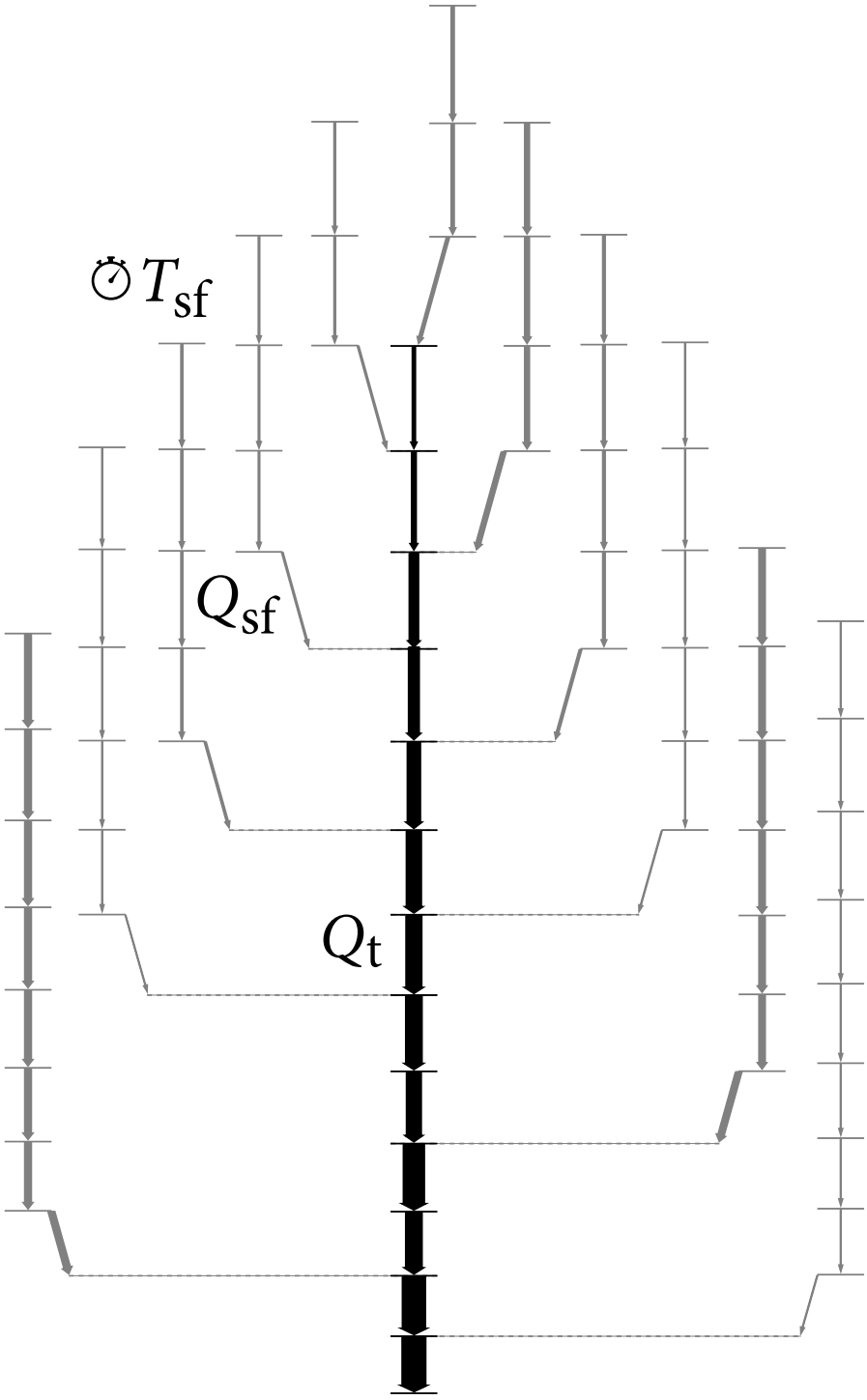

Figure 3.18 The side-feeding of band 1 modelled by MLTFIT. Simulated γ rays are shown in grey.

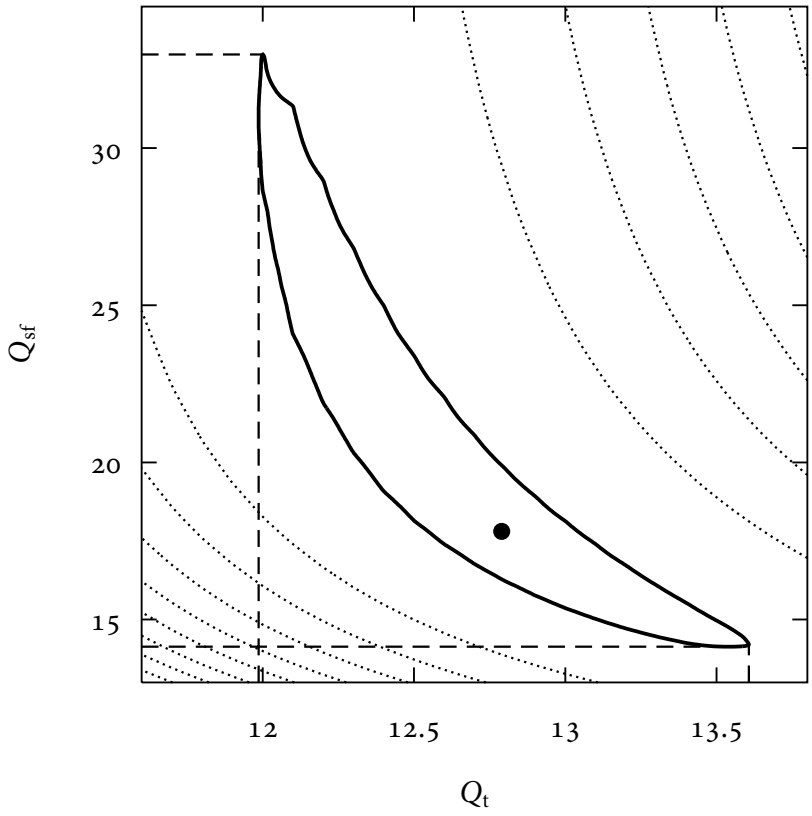

Figure 3.19 A χ^2 contour plot for band 1. The black point indicates the lowest value, χ^2_{min}, while the first (bold) contour has a value of χ^2_{min} + 1. Successive contours (dotted lines) represent $\chi^2_{min} + 10, +20, \ldots, +80$. The dashed lines indicate the uncertainty limits on the fitted parameters. This plot is for a fixed value of T_{sf} – the complete error analysis involves calculating the χ^2_{min} + 1 contour in an additional dimension, corresponding to the T_{sf} parameter.

Band	Q_t (eb)	Q_{sf} (eb)	T_{sf} (fs)
1	$12.8^{+0.9}_{-0.8}$	18^{+30}_{-5}	54^{+4}_{-6}
2	$15.9^{+1.1}_{-0.8}$	$69^{+>11}_{-57}$	11^{+4}_{-11}
3	$12^{+>18}_{-3}$	$6.8^{+3}_{-1.3}$	$1.4^{+13}_{-0.4}$

Table 3.4 Preliminary results using a three-parameter fit. A '>' indicates the uncertainty exceeds the maximum value allowed by the fitting program.

Presented in Table 3.4 are the preliminary results, calculated using the method described thus far, while Fig. 3.20 compares experimental and theoretical $F(\tau)$ curves for bands 1 and 2.

Fig. 3.20 illustrates a number of problems with the fit that are reflected in the numerical results. Firstly, some of the points (particularly 1086 keV in band 1) are very far from the best-fit value, and as such the χ^2 of the fit is 28.2, with an associated probability of 9×10^{-5}. This problem will be discussed in Section 3.2.9. The second problem is that the best-fit curve approaches an initial $F(\tau)$ that is significantly less than 1. This is because the fitted value of the side-feeding delay T_{sf} is 54 fs.

There is no physical reason for T_{sf} to be greater than a few femtoseconds. Indeed, for the majority of DSAM measurements performed to date, either good results have been obtained using the assumption that $T_{sf} \sim 0$ fs (e.g. [57]), or T_{sf} has been fitted at no more than a few femtoseconds [58–60]. Two exceptions are band 1 of ^{152}Dy with $T_{sf} = 24.0^{+1.5}_{-4.5}$ fs [61] and band 2 of ^{194}Hg with $T_{sf} = 28^{+3}_{-6}$ fs [62, 63]. No satisfactory explanation has been put forward for either result, and in the case of ^{152}Dy, a DSAM experiment performed under very similar conditions found no delay for the same band [57].

A third problem is that despite the $F(\tau)$ values of bands 1 and 2 being markedly different, the Q_t values of the two bands are only $\sim$ 3 eb apart. At 15.9 eb, the Q_t

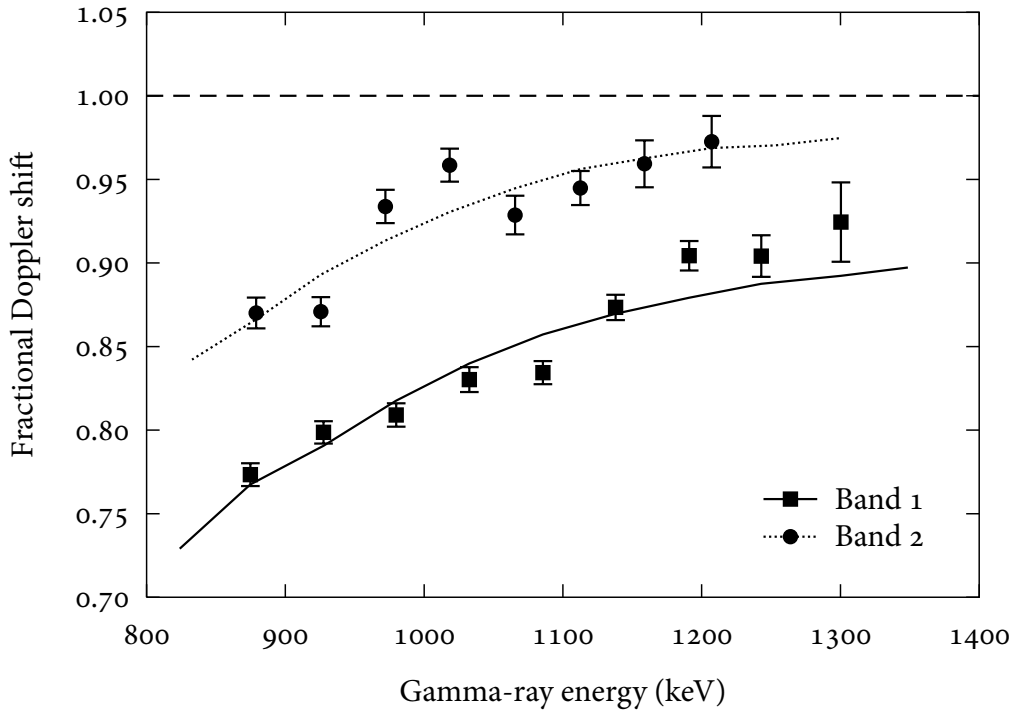

Figure 3.20 Fits of bands 1 and 2 with Q_t, Q_{sf} and T_{sf} free to vary and β_0 = 0.02933. Parameter values are given in Table 3.4.

of band 2 is rather low compared to theoretical predictions. It may seem rather fallacious to use a result as evidence to discount the method used to obtain it, but we should remember that the motivation for studying ^{154}Er is that the SD band can be used to calibrate the Q_t of the TSD band. Similarly, and although the Q_t of TSD bands in ^{157,158}Er have been found to exceed predictions, the Q_t of band 1 is far in excess of the theoretical Q_ts presented in Chapter 5.

The Q_{sf} values for bands 1 and 2 are also extremely high, although their large uncertainties allow for values close to Q_t. Indeed, such large error limits make the inclusion of a Q_{sf} parameter rather redundant and possibly even a hindrance, since the additional parameter has a tendency to increase the error on Q_t.

In light of these problems, a number of changes to the model are proposed. One overriding problem is that the model was developed assuming that

> "[…] these types of measurements are no longer limited by the statistical accuracy of the measurement […]" [63]

in which case one can afford to use a sophisticated model with three free parameters. The above assertion was true at the time, when a new generation of high-resolution detector arrays, such as Gammasphere, had only recently come online and an unprecedented amount of data could now be collected for relatively intense SD bands. However, we are now still using the same generation of detector arrays for DSAM experiments, while experimental boundaries have been extended to very weak bands such as those in ^{154}Er. In other words, the statistical accuracy of our measurements is worse than that of the measurements to which the side-feeding model were first applied. There are too many free parameters to produce a meaningful result from the limited data that we have.

We therefore propose to reduce the number of free parameters from three to only one: Q_t. In order to do this, we must make certain assumptions about the values of the two parameters we wish to eliminate. First, we can fix Q_{sf} by assuming that the side-feeding bands have the same quadrupole moments as the main band. This is a reasonable assumption, and is borne out by previous measurements where Q_{sf} has been allowed to vary freely. In these cases, Q_{sf} has usually been found to be roughly equal to Q_t [9, 18, 57, 64] or slightly lower than it [57, 61, 65–67]. Occasionally, Q_{sf} has been found to be significantly lower than Q_t [63, 68, 69]. However, the constraint that $Q_{sf} \sim Q_t$ is not unprecedented [70–72], and indeed Ur et al. resort to it in Ref. [72] when allowing Q_{sf} to vary freely gives unreasonable results, as is

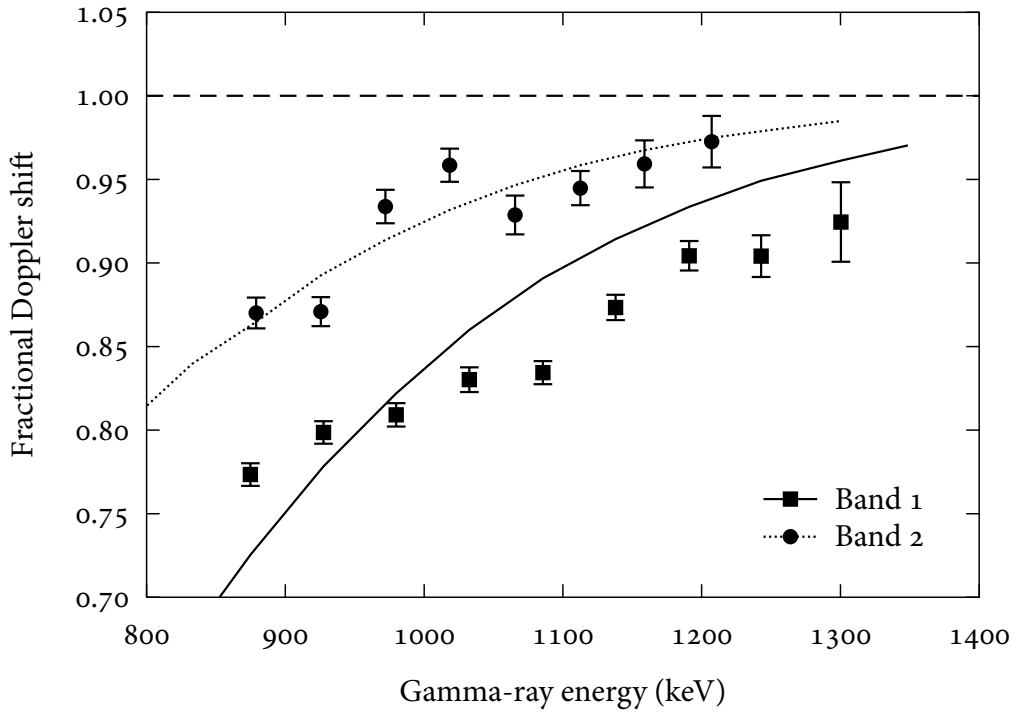

Figure 3.21 Fits of bands 1 and 2 with $Q_{sf} = Q_t$, $T_{sf} = 1$ fs and $\beta_0 = 0.02933$. For band 1, $Q_t = 10.0$ eb and for band 2, $Q_t = 15.6$ eb.

the case here.

We can then use the fact that very large values of T_{sf} are, as noted above, both very rare and seemingly unphysical to justify fixing T_{sf} at a small value, e.g. 1 fs. Fig. 3.21 shows the revised fit with only the Q_t parameter free. This time, the Q_t for band 1 is 10 eb – closer to the range of values predicted for the TSD minima in Chapter 5. However, the Q_t of band 2, 15.6 eb, has changed little and is still far from the values predicted for any minima. More importantly, one can see by inspection that the fit to band 1 is very poor, which is confirmed by a χ^2_{min} value of 201.

It would seem, then, that the large T_{sf} is justified, empirically if not physically. However, the 'gap' between $F(\tau) = 1$ and highest measured transitions in band 1

would be reduced if β_o were lower than calculated. This is plausible, since β_o is theoretical (see Eq. 3.19 and 3.24). The next problem is therefore to find a better way of calculating β_o. The next section describes an attempt at doing this using data collected using the thin target.

3.2.8 Measurement of β_o using thin-target data

The thin target consisted of two stacked self-supporting ^{110}Pd foils of total thickness 1 mg/cm^2. The main idea behind using the data collected from it to determine β_o is that nuclei created in the target are not stopped within it as with the backed target. The nuclear velocity upon exiting the target, which will be denoted β_{ex}, depends on the stopping powers of the nuclei in the target material. If we can measure β_{ex} using the DSAM, we can compare the theoretical and experimental exit velocities and hopefully deduce something about the true stopping power of the target material.

Figure 3.22 shows the measured v/c and average nucleus position as a function of spin for the normally-deformed states in the level scheme. The nucleus' position along the beam path can be calculated using the fact that the detector angles relative to the nucleus will change as it travels away from the target. We can then perform a fit of $\cos\theta$ versus centroid energy as in Fig. 3.14 but with θ allowed to vary depending upon a free parameter, the position along the beam path. The fit with the minimum χ^2 should give the nuclear position.

The measurements in Fig. 3.22 for ^{150}Dy clearly show that the nucleus exits the back of the target before it has decayed to its ground state. We can calculate β_{ex} by averaging all the measured velocities below the 'exit spin', which in this example is $I \sim 19$. For ^{150}Dy, we obtain $\beta_{ex} = 0.0256$. All measurable values of β_{ex} for the

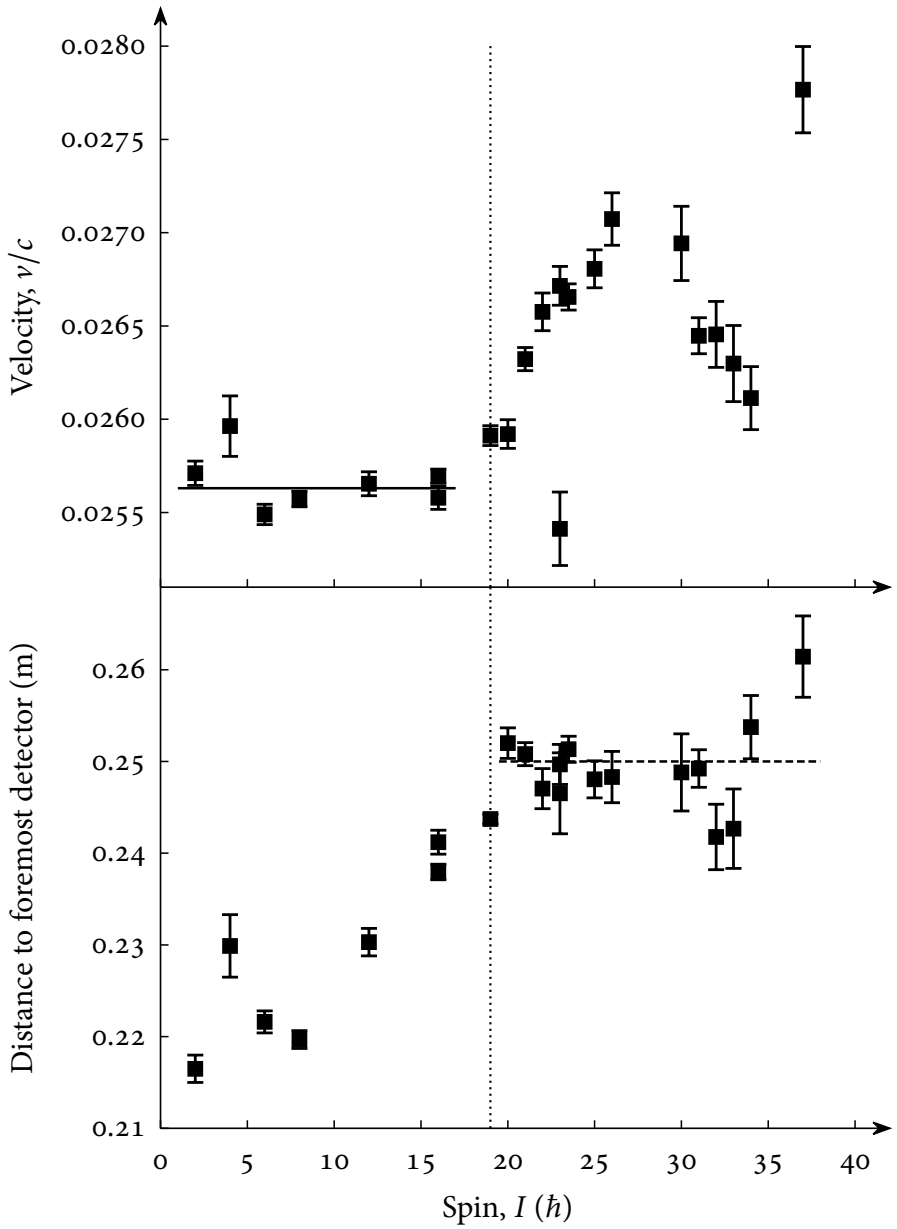

Figure 3.22 Thin-target measurements for transitions in ^{150}Dy. There is a clear flattening of the nuclear velocity (top panel) below spin ~ 19 (dotted line). The average of these points is taken to be the exit velocity β_{ex} (solid line). The position measurement (bottom panel) shows the opposite trend, with a constant position above spin ~ 19, the average of which (dashed line) is consistent with the nominal target position of 0.254 m.

current experiment are shown in Fig. 3.23. It was not possible to measure β_{ex} for all reaction channels in this experiment, due variously to no clear flattening of β at low spin; doublets causing the value of β to be the average of two values, leading to an insufficient number of data points; or simply too low an intensity to preform a reliable centroid-shift measurement.

Shown in Fig. 3.24 is a comparison of the measured β_{ex} and theoretical values calculated using different parameters. The parameters for Fig. 3.24b are those used thus far, i.e. a constant relative cross-section for each reaction channel at all beam energies. In such a case, the only difference in β_{ex} between reaction channels is due to the difference in stopping powers of the recoil nuclei in ^{110}Pd. Since all the nuclei have approximately the same A and Z, the terms on the right of Eq. 3.25 show little varation and so, by consequence, do the values of β_{ex}. This is clearly not the case in the experimental data (Fig. 3.24a), where the range in β_{ex} is an order of magnitude greater. We must conclude that the variation in cross-section with beam energy should be taken into account when calculating β_o.

If this is done, using cross-sections calculated by PACE, the values of β_{ex} shown in Fig. 3.24c result. The relative placement of the values is roughly correct, and the relative placement of isotopes of the same element is always correct, although the magnitude of the difference is overestimated for holmium and dysprosium. However, it is apparent that these values are consistently greater than the experimental values, and it is this fact that allows us to make the case for β_o being lower than the theoretical value. If the velocity of nuclei exiting the target is lower than predicted, it is reasonable to suppose that they are also created with a velocity lower than predicted (although we shall see that it is not necessarily the case).

The next question is whether the data can be used to determine a new β_o. As

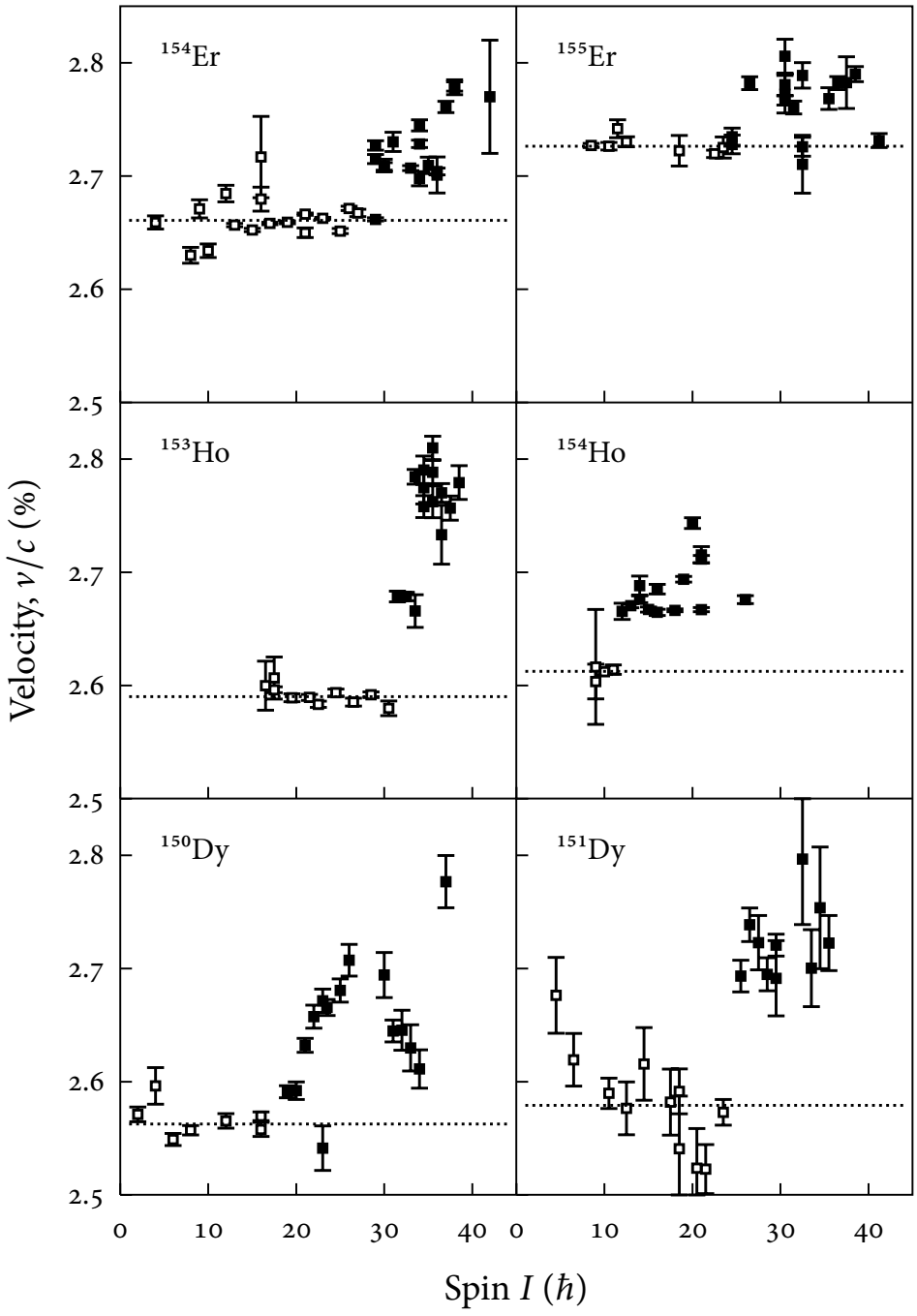

Figure 3.23 Doppler-shift measurements from the thin-target data. The v/c values indicated by unfilled squares were averaged to calculate β_{ex} (dotted line).

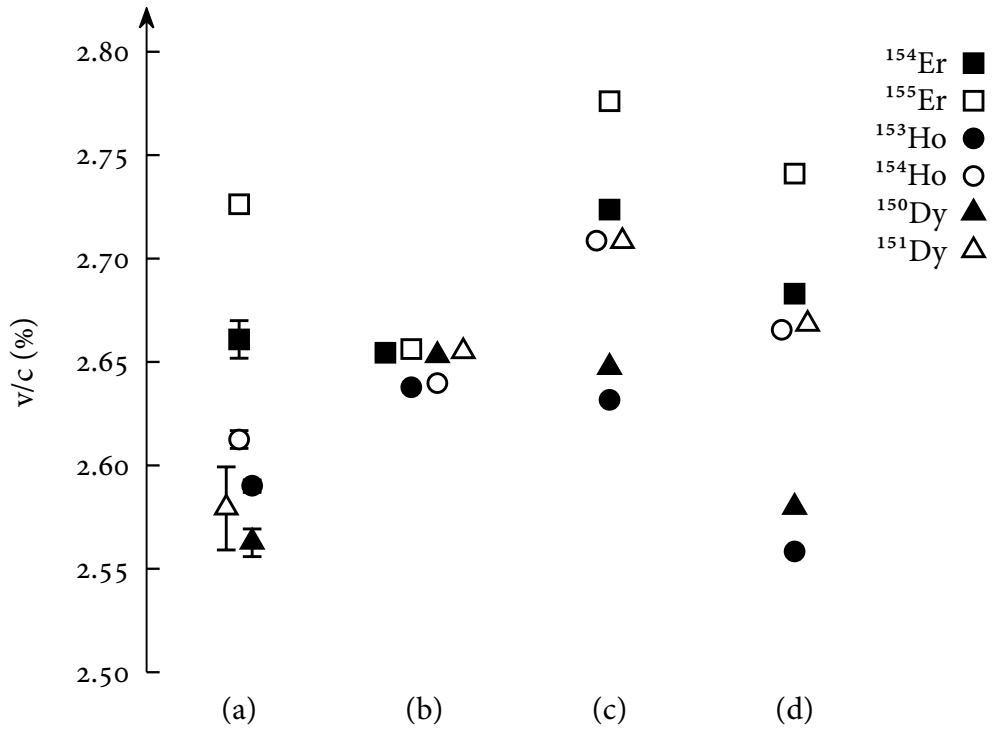

Figure 3.24 A comparison of (a) experimental and (b–d) theoretical velocities of nuclei exiting the thin target (β_{ex}). The calculations use (b) a constant reaction cross-section at all beam energies and dE/dx from SRIM, (c) cross-sections calculated by PACE and dE/dx from SRIM and (d) cross-sections from PACE and dE/dx_{beam} increased by a factor of 2.

stated at the end of the last section, β_o is theoretical and relies on the value of dE/dx for ^{48}Ti in ^{110}Pd provided by SRIM. A higher value of dE/dx would lead the recoils to be created with a lower average energy (see Eq. 3.19) and therefore a lower β_o. We can indeed determine a new value of dE/dx by performing a χ^2 minimisation. Here, dE/dx is the free parameter and the χ^2 comes from the difference between the resulting β_{ex} and the experimental β_{ex}.

The best-fit dE/dx is 21 MeV mg^{-1} cm^2, or twice the SRIM value. The resulting β_{ex} are shown in Fig 3.24d, and they agree fairly well with experiment. The β_o for

^{154}Er calculated using this new $\mathrm{d}E/\mathrm{d}x$ is 0.0286, or 97.5% of the previous value. This is consistent with the largest β measured in ^{154}Er of 0.02853 for 1208 keV in band 2.

However, it should be noted that an inaccurate $\mathrm{d}E/\mathrm{d}x$ for the beam is not the only explanation for the β_{ex} results. So far we have only considered the slowing down of the *beam* nuclei in the target, but of course the recoils continue to slow down after they have been created. If we accept that $\mathrm{d}E/\mathrm{d}x_{\mathrm{beam}}$ is greater than predicted, there is no reason that $\mathrm{d}E/\mathrm{d}x_{\mathrm{recoil}}$ could not also be greater. Indeed, if we have an additional free parameter in the χ^2 fit consisting of a correction factor to $\mathrm{d}E/\mathrm{d}x_{\mathrm{recoil}}$, we obtain a lower χ^2 by multiplying $\mathrm{d}E/\mathrm{d}x_{\mathrm{beam}}$ by 0.7 and $\mathrm{d}E/\mathrm{d}x_{\mathrm{recoil}}$ by 1.4. Of course, this would leave β_{o} slightly higher than the preliminary value and we would no longer have an explanation for the unphysical results.

Likewise, if the target were thicker than the nominal 1 mg/cm^2, we would expect β_{ex} to be lower while β_{o} would change only slightly. The thin target was not made with this type of analysis in mind, and it is not known how close the true target thickness is to the nominal thickness. However, allowing target thickness alone to vary produces a poor fit to the β_{ex} data.

Nevertheless, since an increased $\mathrm{d}E/\mathrm{d}x_{\mathrm{beam}}$ is the only way to explain a lower β_{o}, and since this new β_{o} of 0.0286 is consistent with the highest β measured in ^{154}Er, we use this value to obtain the final Q_{t} measurements. Because of the problems encountered in the present analysis, we suggest that it might be worth making reliable $\mathrm{d}E/\mathrm{d}x$ measurements as part of future DSAM experiments, using for example the 'semi-thick target' method (see e.g. Ref. [73] and references therein).

3.2.9 Error on Q_t

While fits of bands 1 and 2 using $\beta_o = 0.0286$ and Q_t as the only free parameter look reasonable to the eye (see Fig. 4.3 in Chapter 4), there remains the problem of a very high χ^2. If we didn't have previous knowledge of how the $F(\tau)$ values were obtained, we could surmise that the large χ^2 means that the errors on $F(\tau)$ have been underestimated (in other words, the denominator in Eq. 3.17 is too small.) However, we already made sure in Section 3.2.4 that the fits used to calculate $F(\tau)$ had acceptable χ^2s, and hence, through error propagation, the errors on $F(\tau)$ are in principle correct.

This implies that the $F(\tau)$ curve of band 1 really does follow the trend in Fig. 3.21, i.e. there is a 'dip' around 1100 keV. While the possibility that this reflects a real physical phenomenon is discussed in Chapter 4, we will conclude in that chapter that there is no satisfactory explanation for the dip, and so we are forced to fit the data as they are presented.

We could choose to simply ignore the large χ^2, but it poses a problem when calculating the uncertainty on Q_t. Using the one-dimensional equivalent of the method illustrated in Fig. 3.19, we find that for a large χ^2_{min}, χ^2 rises rapidly for a small change in the free parameter Q_t. Hence, we obtain unreasonably small uncertainties on Q_t, given in Table 3.5.

This is where we reintroduce the jackknife method [51, 52] briefly discussed in Section 3.2.4. It is useful for estimating the errors on parameters in parametric fits when it is impossible or inconvenient to calculate them analytically. The basic procedure is:

1. Delete point i from the set of N data points.

Band	Q_t (eb)
1	$11.00^{+0.11}_{-0.13}$
2	19.5 ± 0.7
3	10.0 ± 0.4

Table 3.5 Preliminary results using a single free parameter, Q_t, and uncertainties calculated using the method presented in Section 3.2.7.

2. Refit the parameters using this subset of $N - 1$ data points.

3. Repeat 1 and 2 for all N data points.

4. The jackknife estimate of the standard error on a parameter $\hat{p}$ is then

$$\sigma_J(\hat{p}) = \sqrt{\frac{N-1}{N}\sum_{i=1}^{N}(\hat{p}^{(.)} - \hat{p}^{(i)})^2} \tag{3.26}$$

where

$$\hat{p}^{(.)} = \frac{1}{N}\sum_{i=1}^{N}\hat{p}^{(i)} \tag{3.27}$$

and $\hat{p}^{(i)}$ is the best-fit parameter value resulting from step 2.

The jackknife standard error σ_J given in Eq. 3.26 essentially measures the scatter of the data points, weighted by their uncertainties. For example, if an $F(\tau)$ value is far from the line of best fit and has a relatively small uncertainty, its exclusion will lead to a large change in the fitted Q_t and it will therefore make a large contribution to the squared term in Eq. 3.26. This method was used to calculate the final errors given in Chapter 4.

3.3 The search for new bands

This section details how new strongly deformed bands were found in the data. The main difficulty arises from the fact that these bands are difficult to see when gating on transitions in the main, 'normally-deformed' level scheme. In the case of ^{154}Er, this is mostly because the bands have a relative intensity of a few per cent down to fractions of a per cent, and as such are drowned out by other transitions.

Additionally, most of the data in this experiment came from the thick target. In the thick target, the nucleus is still moving when it emits γ rays from the strongly deformed states (which is essential for the DSAM), but it has already stopped by the time it reaches the ND states, since these are much longer-lived. Hence a Doppler correction is required to align peaks from the strongly deformed states (such as those shown in Fig. 3.7), while no Doppler correction is required to align peaks from the ND states. Consequently, when data are sorted with no Doppler correction so that the ND transitions can be gated on, any peaks from the strongly deformed states will be too broadened to see.

3.3.1 Cubes

The solution makes use of the regular energy spacing that is typical of strongly deformed rotational bands. The data must first be sorted into a form from which spectra can be rapidly extracted by the placing of energy gates. Currently, one of the best ways of doing this is to create a multi-dimensional histogram of the data using software included in the RADWARE package [74, 75]. A histogram with a single dimension – simply a spectrum, of which there are many examples in this thesis – tells us the number of γ rays in a data set that fall inside a particular energy bin. A

histogram with two dimensions, called a *matrix*, has an additional energy dimension, so it can tell us, for each energy bin, what γ rays were detected *in coincidence* with γ rays of that energy. Effectively, each energy bin has its own one-dimensional histogram, so that by gating on a particular energy in the matrix we can produce a spectrum of coincident peaks. In this way, we can deduce a level scheme by identifying which γ rays follow on from each other, and which do not.

Inevitably, confusion may arise when more than one transition in a level scheme has the same energy, or when more than one nucleus in the data set has transitions of a certain energy. Gating on an energy will produce a spectrum with peaks that are coincident with *all* γ rays of that energy, so that peaks from different parts of a level scheme or different nuclei may be mixed together.

To overcome this we can create histograms with three dimensions (*cubes*) or even four dimensions (*hypercubes*), allowing us to simultaneously gate on up to two or three energies, respectively. The resulting spectra are extremely clean, and the ability to gate on multiple transitions provides additional information in the deduction of the level scheme. The idea here is to use the characteristic spacing of γ rays in strongly deformed bands to 'guess' the energies of unknown bands. The cleanliness of the multiple-gating technique should allow us to see even very weak bands if we guess the energies correctly.

Additionally, RADWARE is able to produce spectra from a large number of multiple gates in a matter of seconds, compared to a few hours for the MTSORT sorts that produced the DSAM spectra. This allows us to perform a thorough and systematic search of the data in a reasonable amount of time.

To search for new bands in the current data set, several cubes were made with different Doppler corrections applied to the data. As illustrated in Fig. 3.10, the

quality of the spectra depends on how well the peaks from individual detector rings are aligned i.e. how well the Doppler correction matches the Doppler shifts of transitions in the band. Since we have no information about the Doppler shifts of the bands we are searching for, we must sort the data with different Doppler corrections and test each case.

The RADWARE program LEVIT8R, used for analysing cubes, has an 'SD search' function [76] which allows cubes to be tested for strongly deformed bands using lists of energy gates specified by the user. The program sets the gates and calculates a 'figure of merit' for the resulting spectrum based on the number of counts in the spectrum and how close these counts are to the energies in the list. So, for example, if we wanted to look for bands with an energy spacing of 50 keV, our gate list file might resemble the following:

```
List 1
 800
 850
 900
 950
1000
1050
1100
1150
1200

List 2
 801
 851
 901
 951...

  ⋮

List 50
 849
```

899
949
999
1049
1099
1149
1199
1249

Thus any bands with a 50 keV energy spacing and transitions in the ~ 800–1250 keV region should be picked up by the search routine.

Similar searches were performed for energy spacings of 30–60 keV, which is what we would reasonably expect for these kinds of bands. This procedure was followed for cubes with a range of Doppler corrections, i.e. β = 70–100% at 10% intervals. In this way, we have performed a comprehensive, systematic search of strongly deformed bands in the data. The results are presented in the following chapter.

Chapter 4

Results

4.1 New bands

We have found two new strongly deformed bands in the data which we believe belong to ^{154}Er. These are shown in Fig. 4.2. The γ-ray energies and relative intensities of the known and new strongly deformed bands in ^{154}Er, as measured in the current data, are given in Tables 4.1 and 4.2, respectively. The maximum intensity of band 1 relative to that of the 4n channel, taken to be equivalent to the intensity of the $2^+ \rightarrow 0^+$ 560 keV transition, was measured at 0.6%. This is in agreement with previously published values [15, 20]. Band 2 was measured to have approximately half the intensity of band 1, and bands 3 and 4 half again.

As with the two previously known bands, we could not link the new bands definitively to the ND level scheme. We instead base the assignment on the observation of ND transitions in spectra produced by gating on the bands, shown in Fig. 4.6. These spectra and their implications regarding where the bands feed into the main level scheme are discussed in Section 4.3.

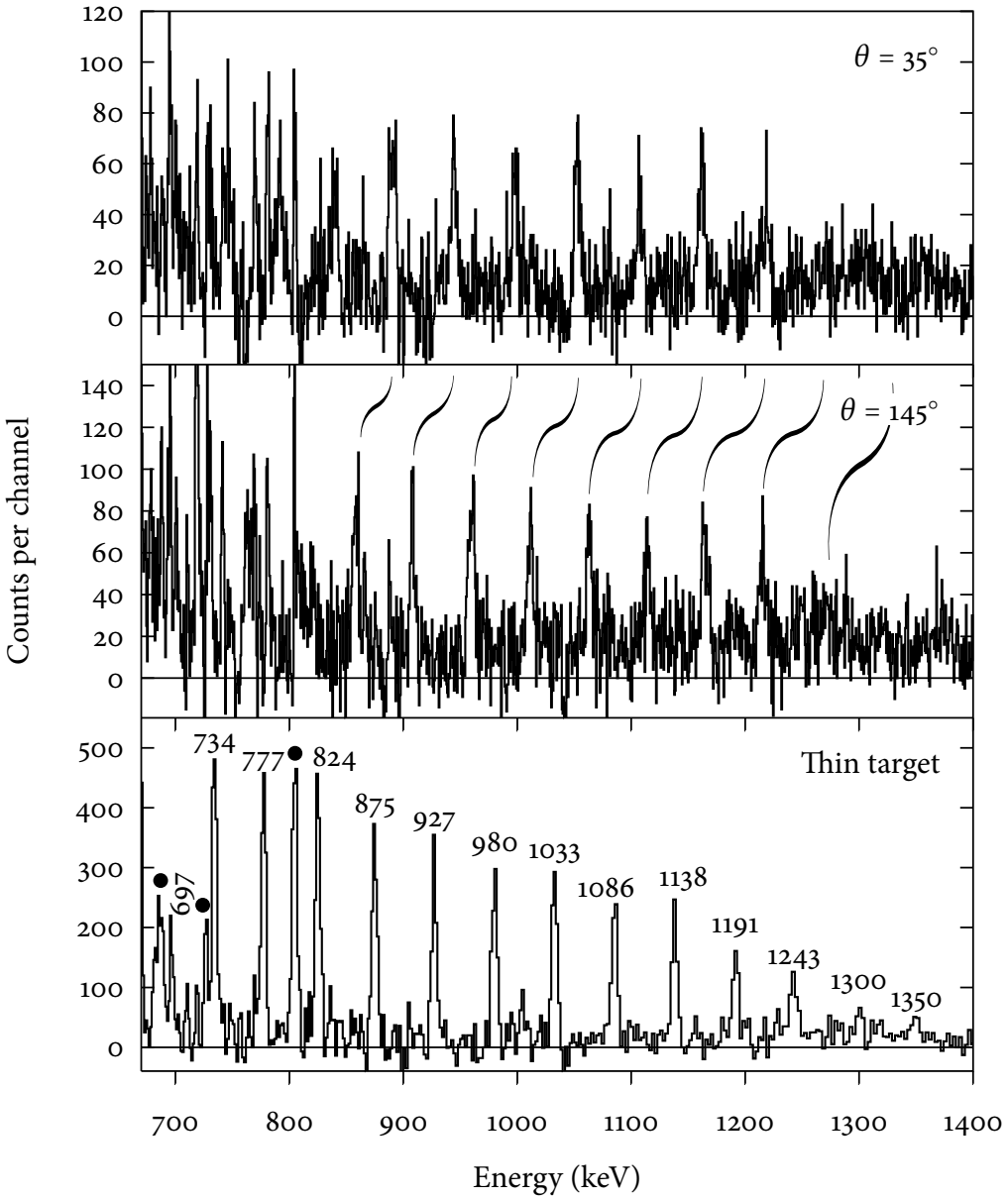

Figure 4.1 Typical spectra from individual detector rings (top panels) showing the Doppler shifted peaks in band 1. Spectra were obtained from the backed-target data by imposing three successive gates (γ^3) from a list of all in-band energies between 734 keV and 1300 keV, followed by a background subtraction as described in Section 3.2.2. (Bottom panel) Thin-target, γ^3-gated coincidence spectrum for band 1 produced in the RADWARE program 4DG8R. Black points indicate ND transitions.

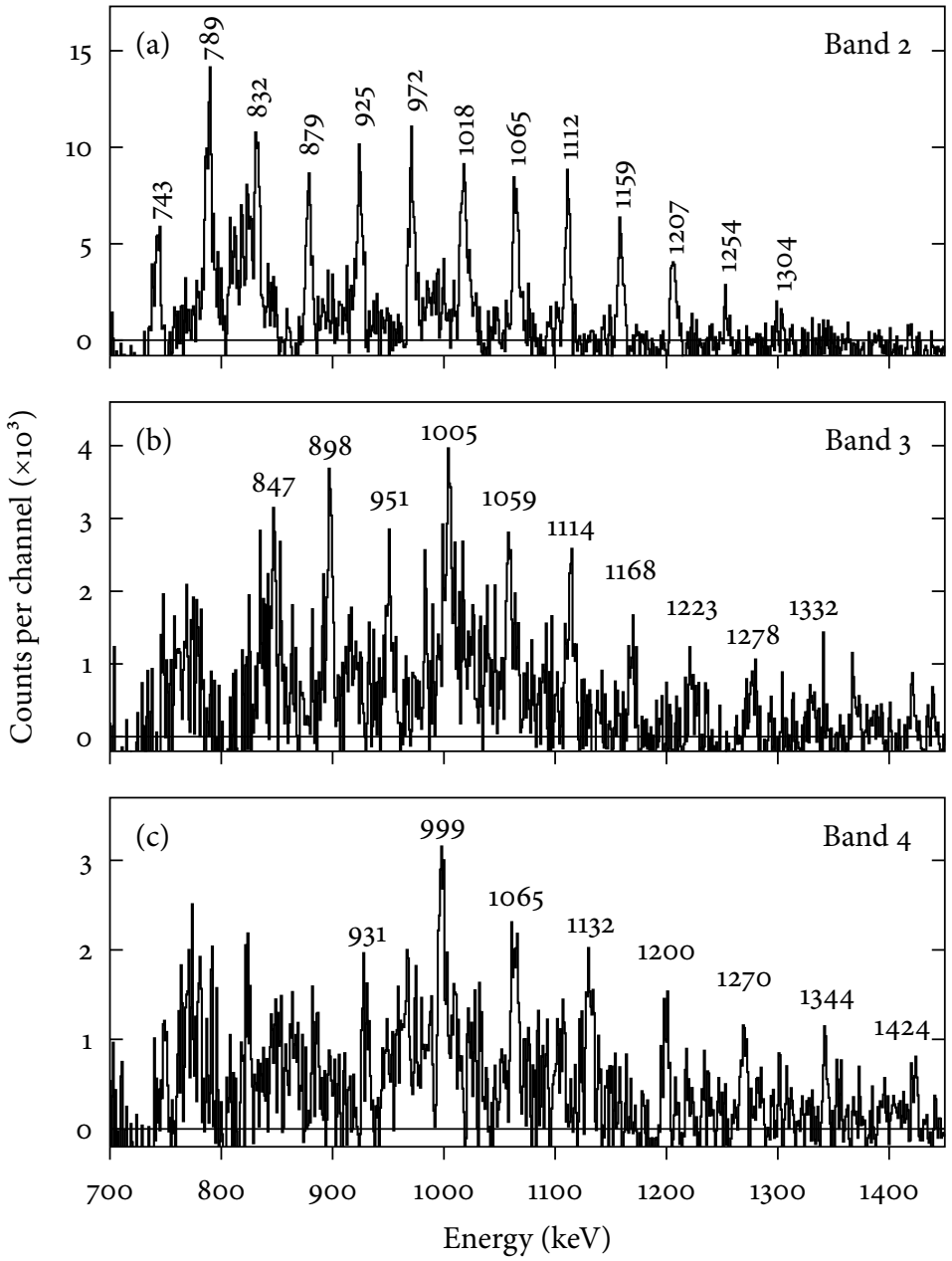

Figure 4.2 Backed-target spectra of (a) band 2 and the newly observed (b) band 3 and (c) band 4 of ^{154}Er. Spectra were produced in the RADWARE program LEVIT8R by applying γ^2 gates from a gate list of the indicated energies to three-dimensional energy histograms (cubes). The γ-ray energies in the cubes were first Doppler corrected by v/c = 2.80% for band 2 and v/c = 2.62% for bands 3 and 4.

	E_γ (keV)	Relative intensity	$I_\mathrm{i} \rightarrow I_\mathrm{f}$
Band 1	696.5(3)	13.8(24)	$(26^+ \rightarrow 24^+)$
	734.39(8)	≡ 100(5)	$(28^+ \rightarrow 26^+)$
	777.09(8)	97(5)	$(30^+ \rightarrow 28^+)$
	824.29(7)	69(4)	$(32^+ \rightarrow 30^+)$
	875.09(7)	89(3)	$(34^+ \rightarrow 32^+)$
	926.98(7)	62.6(28)	$(36^+ \rightarrow 34^+)$
	980.19(7)	69.2(28)	$(38^+ \rightarrow 36^+)$
	1032.79(8)	66.9(28)	$(40^+ \rightarrow 38^+)$
	1085.53(8)	63.7(29)	$(42^+ \rightarrow 40^+)$
	1138.24(11)	56(3)	$(44^+ \rightarrow 42^+)$
	1191.09(13)	45(3)	$(46^+ \rightarrow 44^+)$
	1242.65(18)	39(3)	$(48^+ \rightarrow 46^+)$
	1299.5(4)	19(4)	$(50^+ \rightarrow 48^+)$
	1350.3(7)	13(3)	$(52^+ \rightarrow 50^+)$
Band 2	743.02(21)	79(6)	$(28^+ \rightarrow 26^+)$
	789.17(16)	≡ 100(5)	$(30^+ \rightarrow 28^+)$
	832.69(17)	45(3)	$(32^+ \rightarrow 30^+)$
	879.25(13)	65(3)	$(34^+ \rightarrow 32^+)$
	924.93(14)	68(3)	$(36^+ \rightarrow 34^+)$
	971.51(12)	73.3(29)	$(38^+ \rightarrow 36^+)$
	1018.25(13)	75(3)	$(40^+ \rightarrow 38^+)$
	1065.22(13)	75.6(28)	$(42^+ \rightarrow 40^+)$
	1111.80(13)	76.6(27)	$(44^+ \rightarrow 42^+)$
	1159.11(17)	61.4(27)	$(46^+ \rightarrow 44^+)$
	1206.71(22)	51.5(27)	$(48^+ \rightarrow 46^+)$
	1254.0(5)	22.8(26)	$(50^+ \rightarrow 48^+)$
	1303.8(6)	16.3(26)	$(52^+ \rightarrow 50^+)$

Table 4.1 Energies and intensities for the two previously known strongly deformed bands in ^{154}Er. Proposed spin assignments are from the analysis in Section 4.3.

	E_γ (keV)	Relative intensity	$I_i^\pi \rightarrow I_f^\pi$
Band 3	847.4(4)	49(6)	$(28^+ \rightarrow 26^+)$
	898.07(27)	70(5)	$(30^+ \rightarrow 28^+)$
	951.0(4)	45(5)	$(32^+ \rightarrow 30^+)$
	1005.01(21)	≡ 100(6)	$(34^+ \rightarrow 32^+)$
	1059.4(3)	71(6)	$(36^+ \rightarrow 34^+)$
	1114.4(3)	64(6)	$(38^+ \rightarrow 36^+)$
	1169.4(8)	30(6)	$(40^+ \rightarrow 38^+)$
	1223.3(9)	27(6)	$(42^+ \rightarrow 40^+)$
	1277.7(7)	36(5)	$(44^+ \rightarrow 42^+)$
	1331.6(7)	37(6)	$(46^+ \rightarrow 44^+)$
Band 4	931.0(4)	57(10)	$(32^+ \rightarrow 30^+)$
	998.60(23)	≡ 100(7)	$(34^+ \rightarrow 32^+)$
	1064.94(28)	85(7)	$(36^+ \rightarrow 34^+)$
	1131.7(3)	76(7)	$(38^+ \rightarrow 36^+)$
	1199.8(3)	50(6)	$(40^+ \rightarrow 38^+)$
	1270.1(3)	46(6)	$(42^+ \rightarrow 40^+)$
	1343.5(5)	31(5)	$(44^+ \rightarrow 42^+)$
	1423.8(6)	27(5)	$(46^+ \rightarrow 44^+)$

Table 4.2 Energies and intensities for the newly observed strongly deformed bands in ^{154}Er. Proposed spin assignments are from the analysis in Section 4.3.

Band	Q_t (eb)
1	11.0 ± 0.6
2	19.5 ± 1.5
3	10.1 ± 0.9^a

[a] This error is rather small. See text for further discussion.

Table 4.3 Final quadrupole moments for bands 1–3 in ^{154}Er.

4.2 Quadrupole moments

The final values for the quadrupole moments of bands 1–3 are presented in Table 4.3 and the final fits are shown in Fig. 4.3. One issue with these results is the small error on the quadrupole moment of band 3. Its value is ⅔ that of the error on the Q_t of band 1, yet the points are significantly more scattered, and the errors on $F(\tau)$ much larger. The error on the Q_t of band 2 is almost twice as large, despite the smaller errors on $F(\tau)$. This is partly because the experiment is inherently more sensitive to lower Q_ts (see Fig. 4.4). While the errors on $F(\tau)$ are smaller for band 2 and the points appear to be less scattered, they encompass a large range of Q_t values.

We can compare these errors with errors calculated using an alternative method that is more sensitive to the scatter of the points. Now that the number of fit parameters has been reduced to one, we can obtain a Q_t from a single $F(\tau)$ value. If we fit each $F(\tau)$ value in the band to get a quadrupole moment and an error, we can calculate a weighted mean with a standard error. Using this method, the values of Q_t for bands 1–3 are, respectively, 10.3 ± 0.4, 20 ± 3 and 8 ± 4. These uncertainties seem intuitively more sensible.

However, they are partly a result of Q_t being arbitrarily limited to a value of 30 eb (larger values than this are physically unlikely). Indeed, the Q_t of the 1223 keV

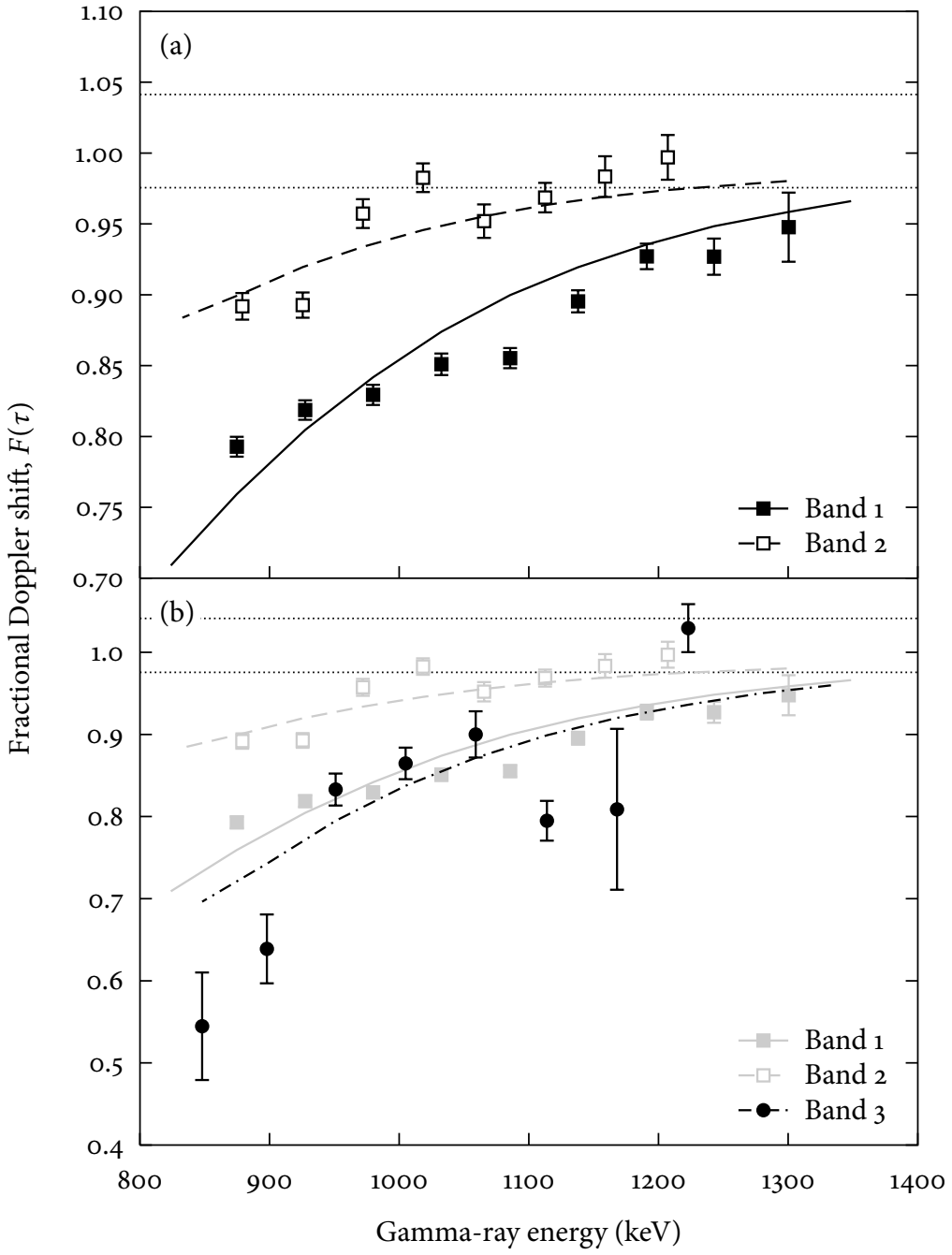

Figure 4.3 Measured $F(\tau)$ values and fitted quadrupole moments for (a) bands 1 and 2 in ^{154}Er and (b) band 3 in ^{154}Er. The dotted lines indicate the range of initial velocities of the ^{154}Er recoils.

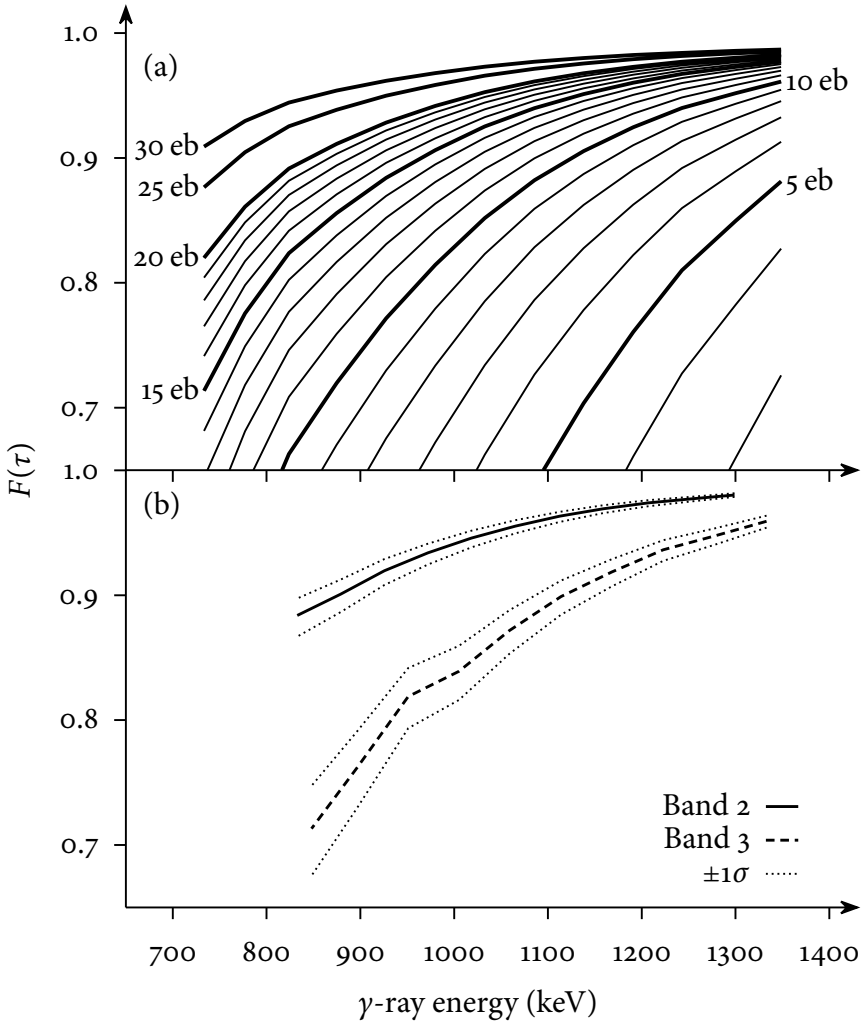

Figure 4.4 (a) Simulated $F(\tau)$ curves for a range of Q_t values. The experimental sensitivity to Q_t decreases with increasing Q_t, meaning that (b) the error limits on band 3 span a wider range of $F(\tau)$ values than those of band 2, despite the error on Q_t being *smaller* for band 3 (see Table 4.3).

transition in band 2 reaches this limit. If MLTFIT is rewritten to allow a higher limit of, for example, 80 eb, we find that the Q_t exceeds even this value, leaving the uncertainty of the mean Q_t in excess of 11 eb. Since the uncertainties calculated using this method are so sensitive to an arbitrary value written into the fitting program, we prefer to continue using the jackknife standard error, but treat the error on band 3 with some doubt. The initial aim of this experiment was after all the measure the Q_t of bands 1 and 2, and any additional information is a bonus. We can deduce from the $F(\tau)$ values, $\mathcal{J}^{(2)}$ and optimum Doppler correction that band 3 has a similar deformation to band 1, but 10.1 ± 0.9 eb is almost certainly too precise.

Next is the problem that there seems to be a significant dip in of $F(\tau)$ curve of band 1, reaching its lowest point relative to the fitted curve at 1086 keV. We have already ensured in Section 3.2.4 that the fit that produced this $F(\tau)$ value is acceptable. One possibility is that the spectra used in the Doppler-shift measurement contain some contamination. The presence of a contaminating peak close in energy to an in-band peak would shift the fitted centroid towards the contaminating peak and therefore affect the measured shift. However, the presence of such contamination is difficult to prove, and none is apparent in the spectra.

Another possibility is that the band does not have a constant Q_t. A lower Q_t at the top of the band, increasing at $\sim$ 1033 keV, would result in the observed trend. However, such a change in Q_t would be reflected in a change in the $\mathcal{J}^{(2)}$ moment of inertia. An inspection of $\mathcal{J}^{(2)}$ (Fig. 5.3) reveals that it is fairly constant at intermediate rotational frequencies (corresponding to the middle of the band).

A third, admittedly more far-fetched possibility is a defect in the target. If something were to cause the nucleus to slow down less than predicted below 1086 keV, there would be a flattening of $F(\tau)$ like that observed. Fig 4.5 shows the simulated

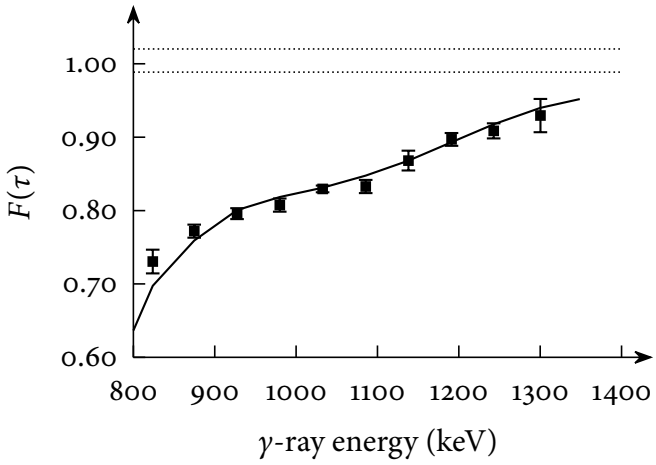

Figure 4.5 Experimental band 1 results with a simulated curve (Q_t = 7.4 eb), if the SRIM simulation is modified to include a gap in the target layer.

$F(\tau)$ curve for Q_t = 7.4 eb if a 1.5 μm vacuum gap is placed at a depth of 0.8 μm in the target, resulting in a good agreement with the measured $F(\tau)$. However, there is no supporting evidence for such a defect, and it was not possible to inspect the target used in the experiment. Additionally, the fitted Q_t for band 2 using the modified simulation is ~ 15 eb, which is much lower than predicted for the SD band.

In summary, we are unable to determine why the data produce such a poor fit. We have nevertheless obtained reasonable Q_t values that follow the overall trend of the $F(\tau)$ values after some modifications to the established analysis method. However, the error on the Q_t of band 3 seems rather small and will be treated cautiously in Chapter 5.

4.3 Feeding into the main level scheme

As stated, we have not identified any transitions linking the strongly deformed bands to the ND states. This leads to some uncertainty in the band spins, and

makes it more difficult for us to assign configurations to the bands. Lagergren et al. [15] have suggested spins on 24^+ and 26^+ for the bottoms of bands 1 and 2, respectively, based on observed coincidences between in-band transitions and transitions between ND states.

We perform a similar analysis here for all four strongly deformed bands. A RADWARE hypercube was created from the thin-target data, which had first been Doppler-corrected to align the peaks from different detector rings. Although we have made use of the change in β with spin in Section 3.2.8, the change is relatively small, and a Doppler correction of $\beta \sim 2.7\%$ aligns both high- and low-spin transitions sufficiently well.

Spectra were produced by triple-gating on transitions in the band of interest (Fig. 4.6). The peaks in the spectra should therefore correspond to transitions between ND states populated below the point at which the strongly deformed bands feed into the main level scheme. We can estimate the spin of the lowest level in a band by determining the highest-spin ND transition in the spectrum. The relative intensities at the bottom of the band (Fig. 4.7) indicate whether we expect the band to feed out gradually or through the bottom state only.

Band 1 appears to feed into the ND level scheme between $I^\pi = 19^-$ and 25^-, in agreement with Lagergren et al. The feeding-out of this band is gradual (i.e. through the bottom two states), making it difficult to determine where the bottom of the TSD band is relative to these levels. Assuming E1 multipolarity for the linking transitions, the 24^+ of Lagergren et al. seems reasonable.

Band 2 is more straightforward, since almost all the intensity appears to feed out after the bottom transition. Again, we cannot see any higher than $I^\pi = 25^-$ in the ND transitions, but this time the $25^- \rightarrow 23^-$ transition (318 keV) is much more

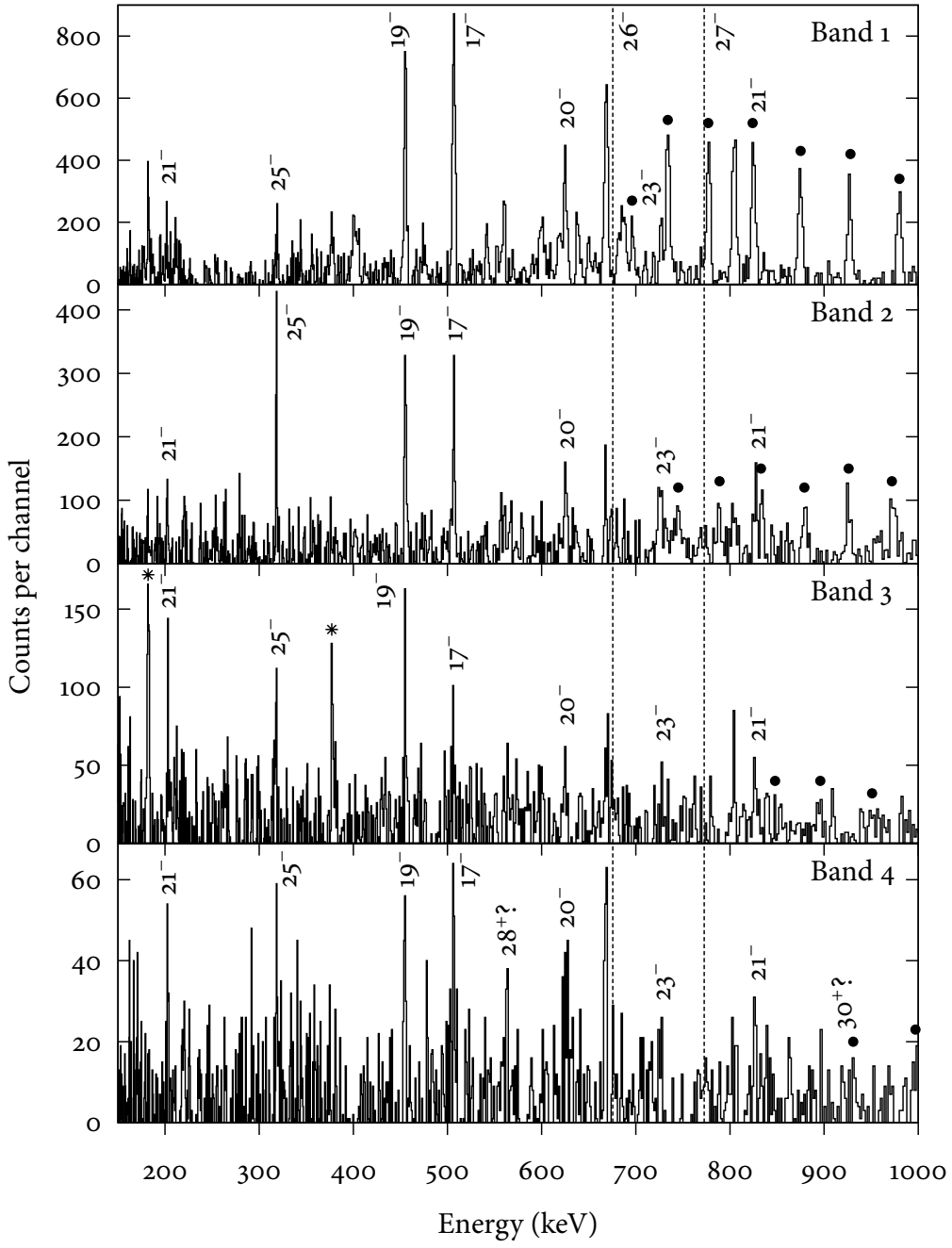

Figure 4.6 ND transitions observed in coincidence with the transitions of bands 1–4 in the thin-target data. Spectra were extracted from a RADWARE hypercube by triple-gating on all known transitions of the relevant band. Transitions are labelled with their initial-state spin and parity. In-band transitions are indicated by black points and contaminating peaks (band 3) with stars. Dotted lines mark the energies of the $26^- \rightarrow 25^-$ and $27^- \rightarrow 25^-$ transitions.

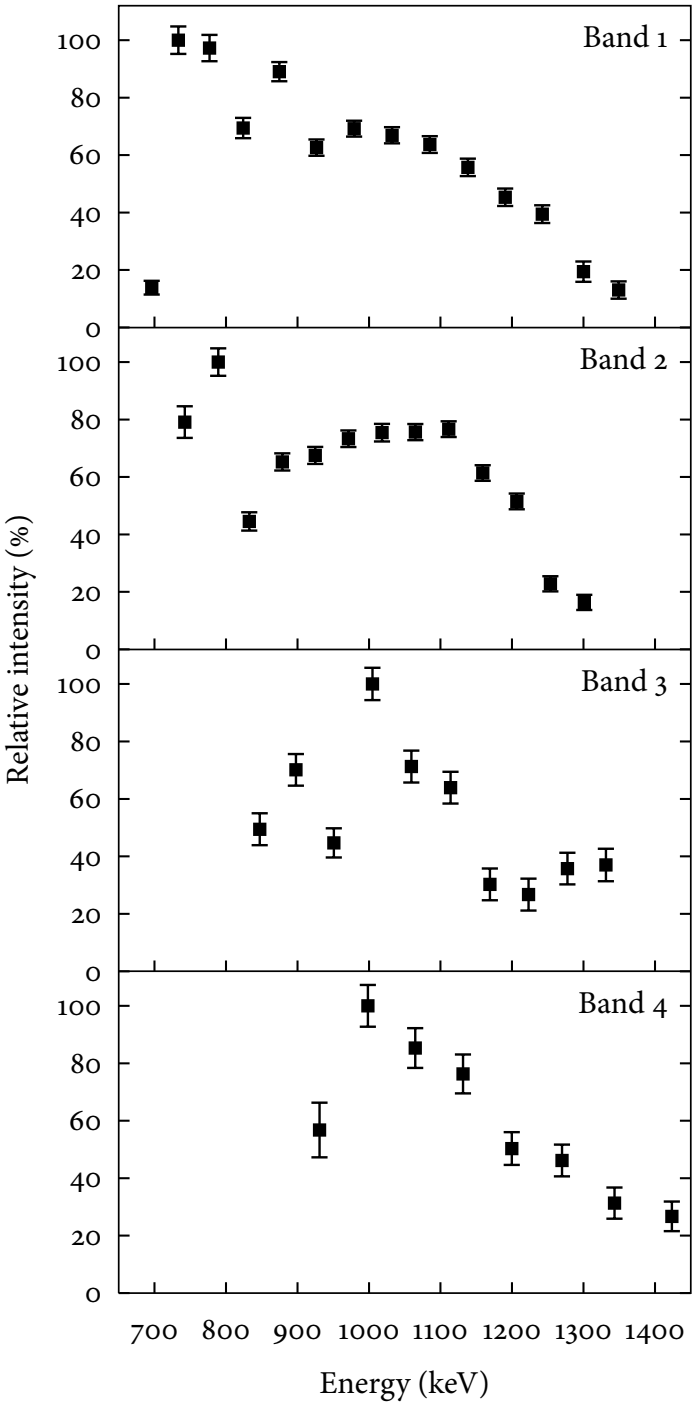

Figure 4.7 Relative intensities of transitions in the strongly deformed bands as a percentage of the maximum intensity. For band 1, intensities were measured using Gaussian fits to the summed and Doppler-corrected γ^3-gated spectra used to perform the DSAM measurement (see Fig. 4.1). For bands 2–4, intensities were taken from the spectra in Fig. 4.2.

intense. This suggests that there is a strong linking transition between the bottom of the SD band and the 25^- state, and so we agree with the 26^+ of Lagergren et al.

For band 3, there is some contamination from ^{151}Dy in the spectrum. The two most intense contaminating peaks (378 keV and 182 keV) are indicated in the figure. The relative intensities of the ND peaks are somewhere between those for bands 1 and 2, but closer to band 2. There may be a $26^- \rightarrow 25^-$ peak (dotted line), but there is certainly no $27^- \rightarrow 25^-$ peak. It is difficult to say from either Fig. 4.6 or Fig. 4.7 whether band 3 feeds out gradually. Putting all this together, we suggest 26^+ for the bottom of the band.

The band 4 spectrum has a clear peak at ~ 563 keV in this spectrum, corresponding to the $28^+ \rightarrow 27^-$ transition. This is close to the $2^+ \rightarrow 0^+$, 560 keV transition, which could be what we are seeing. However, we know that the latter should have around the same intensity as the $4^+ \rightarrow 2^+$, 601 keV transition, which in the spectrum is barely above the background [1]. There are also peaks for the $27^- \rightarrow 25^-$ and $26^- \rightarrow 25^-$ transitions, and there appears to be a small $30^+ \rightarrow 28^+$, 920 keV peak. The $29^+ \rightarrow 28^+$, 625 keV transition is difficult to identify because it is a doublet with $20^- \rightarrow 19^-$. Likewise, the $32^+ \rightarrow 30^+$, 561 keV transition is too close the aforementioned $28^+ \rightarrow 27^-$ and $2^+ \rightarrow 0^+$ transitions. It certainly does not feed in any higher than 32^+ since there is no $33^- \rightarrow 32^+$, 279 keV peak. Based on this, we estimate that the bottom of the band has a spin of 30^+ to 32^+.

[1] This is due to their being an isomeric 11^- state with $T_{½}$ = 35 ns, meaning that γ rays emitted below the isomer are not detected in coincidence with those above.

Chapter 5

Discussion

We have measured the transition quadrupole moment of the two triaxial bands to be 11.0 ± 0.6 eb and ~ 10 eb. These are consistent with the values of $10.9^{+0.6}_{-0.5}$ eb and $11.1^{+1.2}_{-0.9}$ eb for TSD bands 1 and 2 of ^{157}Er, respectively, and $11.7^{+0.7}_{-0.6}$ eb and $11.1^{+1.3}_{-1.0}$ eb for bands 1 and 2 of ^{158}Er [18].

For those nuclei and for ^{154}Er, as we shall see in the following section, these values are too large to correspond to the theoretically favoured positive-γ TSD shape, and are more consistent with the negative-γ shape predicted to be significantly higher in energy. Thus, our results support those of Wang et al., providing both a calibration of the experimental technique through the SD band, and a continuation of the puzzling discrepancy between experiment and theory through the TSD band.

In this chapter, we compare the properties of the four ^{154}Er bands with those of other nuclei, as well as Cranked Nilsson-Strutinsky predictions, and attempt to deduce their underlying single-particle structure.

5.1 Deformation minima

Shown in Fig. 5.1 are potential energy surface (PES) plots resulting from CNS calculations at different spin values [77]. These are in general agreement with the total Routhian surface plots presented by Lagergren et al. [15] resulting from cranking calculations with a Woods-Saxon potential. At $I = 0$, the yrast minimum has a low-deformation non-collective oblate shape ($\gamma = 60°$). Another low-deformation minimum at $\gamma \sim 45°$ briefly becomes yrast at $I = 10$, and the $\gamma \sim 60°$ minimum becomes yrast once more at $I = 20$–50.

At $I = 60, 70$, the SD minimum at $\varepsilon_2 = 0.6$, $\gamma \sim 0°$ becomes yrast. There are two local TSD minima at $0.3 \leq \varepsilon_2 \leq 0.4$, $20° \leq \gamma \leq 30°$ and $0.3 \leq \varepsilon_2 \leq 0.37$, $-20° \leq \gamma \leq -15°$. In keeping with the work of Wang et al. involving similar minima in ^{158}Er [18], we refer to the positive- and negative-γ minima as TSD1 and TSD2, respectively. TSD1 appears to split into two minima at $I = 60$, but we do not observe a shift to larger deformation referred to as TSD3 by Wang et al.

From our experience with classical spinning tops, we intuitively expect the negative-γ triaxial shape illustrated in Fig. 2.7 to be less stable than the positive-γ shape. Indeed, TSD2 is consistently higher in energy than TSD1, and this also the case for ^{157,158}Er [18]. The lower energy of TSD1 means that we would expect band 1, being the most intense, to originate from this minimum, with the weaker bands possibly belonging to TSD2.

One apparent discrepancy between these minima and our observations is that neither of the TSD minima ever become yrast, instead being 'bypassed' in favour of the SD band. Indeed, earlier calculations using the Nilsson potential predict the same trend [78]. However, we have measured the intensity of the TSD band, band 1,

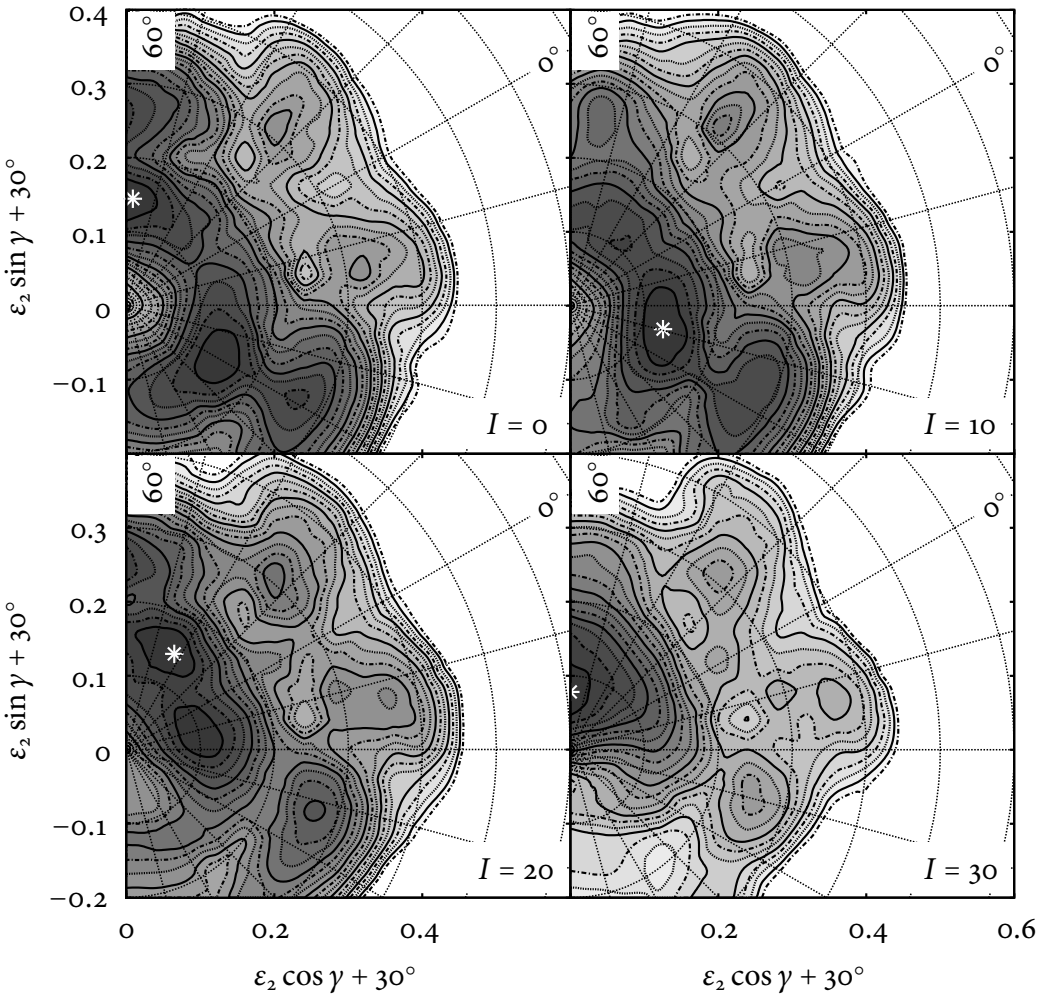

Figure 5.1 Potential energy surfaces calculated using the CNS model for positive-parity configurations in ^{154}Er for a range of spins [77]. Contours are separated by 0.25 MeV and extend to 5 MeV above the minimum, which is indicated by a star.

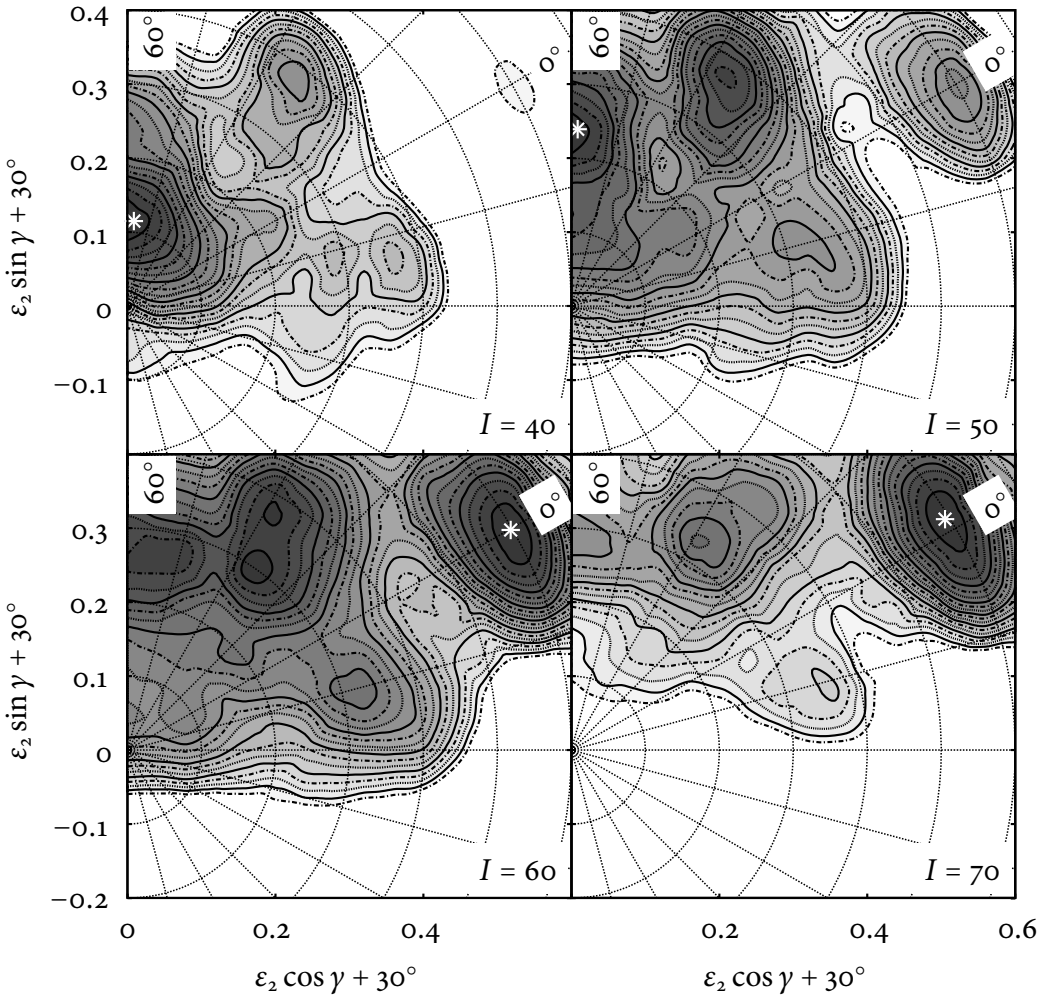

Figure 5.1 continued

to be twice that of the SD band, so we might expect the TSD to be yrast at some spin value. In contrast, Woods-Saxon calculations do predict that the TSD1 minimum becomes yrast at high spin [15, 79], which is also true of the similar TSD minimum in ^{152}Dy [60, 80]. In fact, Beck et al. predict TSD1 to be lower in energy than the SD minimum up to $I = 80$ [79]. On the other hand, our calculations predict that, while TSD1 may not be the *lowest* in energy, it is lower in energy than the SD minimum up to $I = 50$. Since our analysis in Section 4.3 puts the highest measured spin at $I = 52$, it is only to be expected that the TSD band is observed with a greater intensity than the SD band.

5.2 Strongly deformed bands

5.2.1 Band 2 (Superdeformed)

We begin by discussing band 2, since it is believed to arise from a configuration in the theoretically well-established superdeformed minimum, and as such it is the 'calibration' band. The measured Q_t of 19.5 eb confirms this assignment, as this is the magnitude of Q_t that we would expect for SD bands in this region [81].

As with neighbouring SD bands, we compare the configuration of band 2 with the 'doubly magic' yrast SD band in ^{152}Dy (SD-1), since this band has been extensively studied and is linked to the low-spin level scheme [82], meaning that its spins are known and its configuration reasonably certain. In terms of high-j orbitals, this configuration consists of four protons in the deformation-driving $i_{13/2}$ orbital, eight neutrons in the $i_{13/2}$ orbital and two neutrons in the $j_{15/2}$ orbital [57], or

$$\pi\{(i_{13/2})^4\} \otimes \nu\{(i_{13/2})^8(j_{15/2})^2\}.$$

Such configurations are often given as simply the number of nucleons in the $N = 6, 7$ orbitals [83], and so we refer to the favoured configuration as $\pi 6^4 \nu 6^8 7^2$ in this thesis.

The configurations of SD bands in neighbouring nuclei can be regarded as a number of particles or holes relative to the ^{152}Dy SD 'core' [30, 84, 85]. For ^{154}Er, the favoured configurations resulting from CNS calculations involve the occupation of $N = 4$ or $N = 5$ orbitals by the two additional protons relative to ^{152}Dy. As can be seen in Fig. 5.2, these orbitals ($[411]\frac{3}{2}$, $[413]\frac{5}{2}$, $[530]\frac{1}{2}$and $[532]\frac{3}{2}$) are close to the proton Fermi surface (the boundary between occupied and unoccupied states) at $Z = 68$. We also see that the SD shell gap at $N = 86$, which is responsible for the doubly magic nature of ^{152}Dy, persists for ^{154}Er.

Fig. 5.3 shows the dynamic moment of inertia of band 2 compared with that of ^{152}Dy SD-1. The bands follow one another closely, and indeed their energies are consistent to within 2–5 keV [86]. While this supports our configuration assignment, it makes the tentative spin assignment made in Section 4.3 and previously by Lagergren et al. problematic. We have assigned initial-to-final-state spins of $28^+ \rightarrow 26^+$ to the lowest-spin transition, 743 keV. However, the corresponding transition in ^{152}Dy SD-1 of 738 keV is known to be $32^+ \rightarrow 30^+$, hence these would be the minimum spins assigned to the 743 keV transition if band 2 were based on the same configuration. Furthermore, the proposed occupation of $N = 4$ orbitals by the two additional protons would contribute an effective alignment of approximately 1 $\hbar$, while the occupation of $N = 5$ orbitals would contribute approximately 2 $\hbar$. Fig. 5.4 shows the effective alignment of band 2 with ^{152}Dy SD-1 as a reference assuming values of 30 or 32 for the bandhead spin, compared with the predicted effective alignment from the $N = 4, 5$ protons. Despite the large number of known

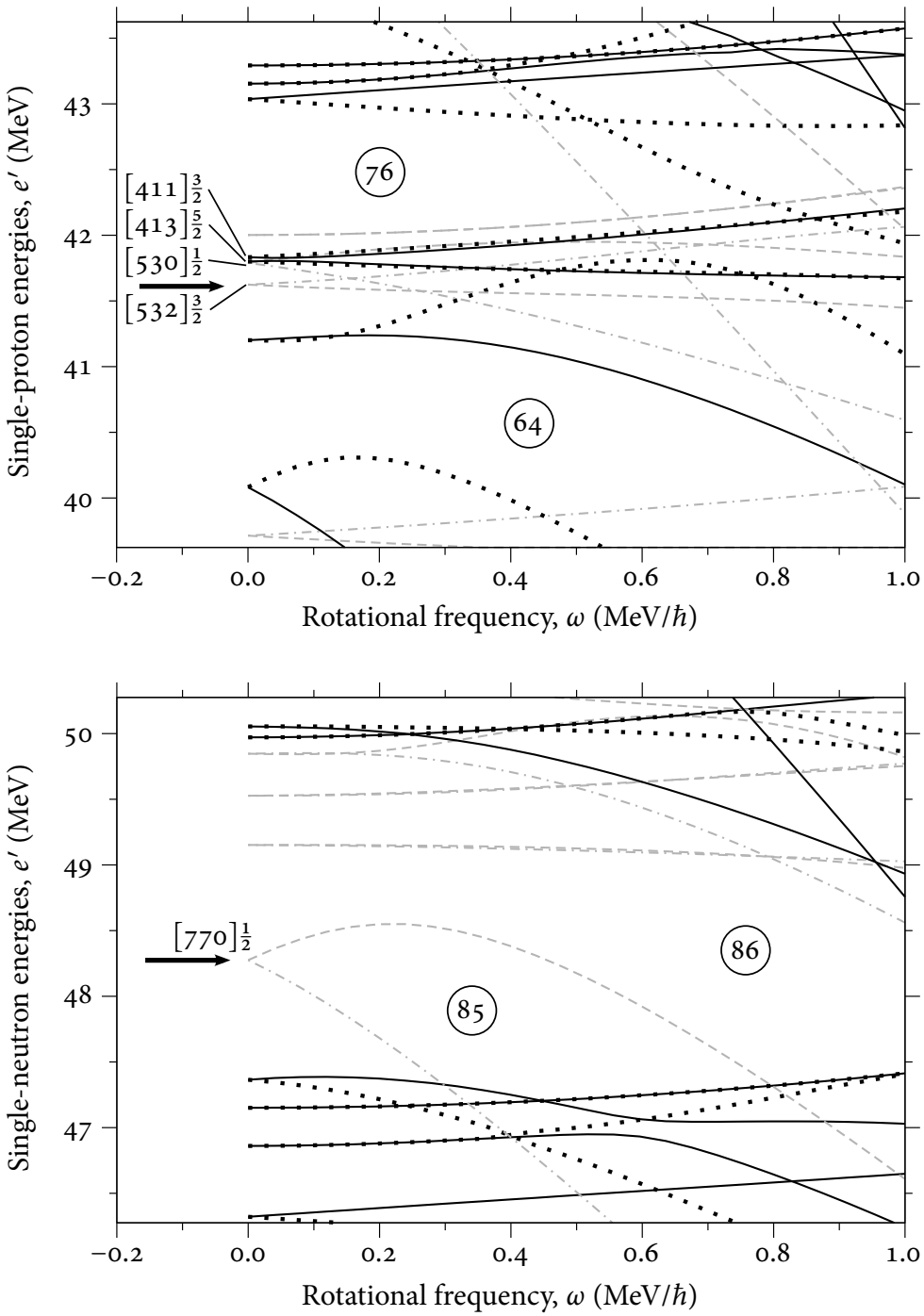

Figure 5.2 Single-particle routhians for the SD minimum, $\varepsilon_2 = 0.611$, $\gamma = 1.6°$, $\varepsilon_4 = 0.062$, calculated using the CNS model. Arrows indicate the Fermi surface, solid lines indicate $(\pi, \alpha) = (+, \frac{1}{2})$, dotted $(+, -\frac{1}{2})$, dashed $(-, \frac{1}{2})$ and dotted-dashed $(-, -\frac{1}{2})$.

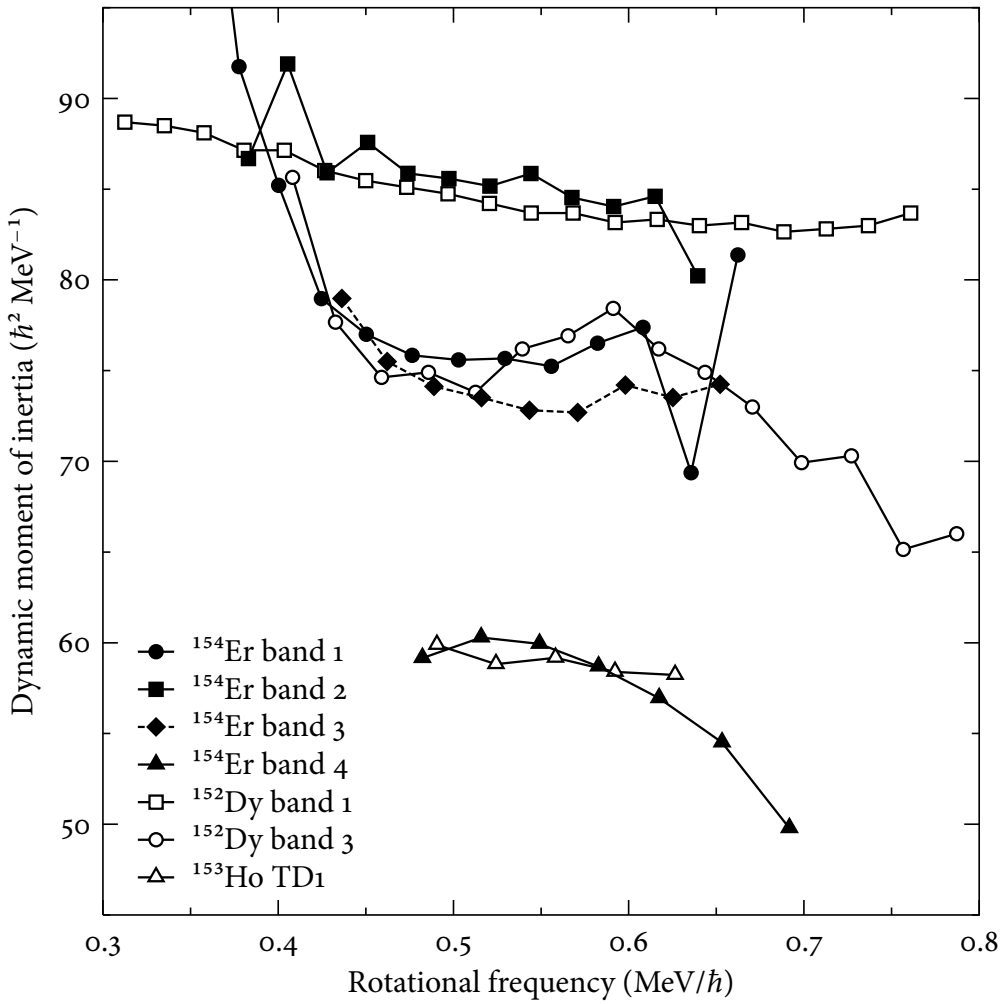

Figure 5.3 Dynamic moment of inertia, $\mathcal{J}^{(2)}$, of the bands in ^{154}Er compared with similar bands in neighbouring nuclei.

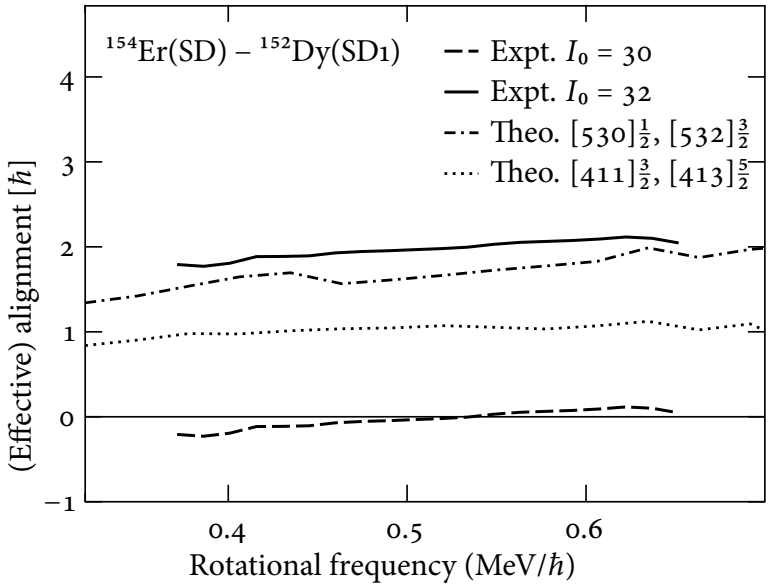

Figure 5.4 The effective alignment, i_{eff} (Eq. 2.23), for the band 2 in ^{154}Er using as reference the yrast SD band of ^{152}Dy. Experimental values are calculated for two possible bandhead spins (I_0), while theoretical values are for the occupation of the indicated orbitals by the two additional protons.

SD bands, few have been definitively linked to normally deformed states [81] and so the nature of these linking transitions is not well-known. Hence, we cannot discount the possibility that the spins are much higher than estimated. Regardless of the spin, the value of i_{eff} is remarkably flat, further supporting the assignment of a similar configuration to the ^{152}Dy band.

Figure 5.5 shows the predicted Q_t for one of the favoured $\pi 6^4 \nu 6^8 7^2$ configurations, which is representative of configurations of this type. The Q_t in the experimental spin range is $\sim$ 20 eb, consistent with our result (with the caveat that we have used this value as a basis to reject our preliminary results.)

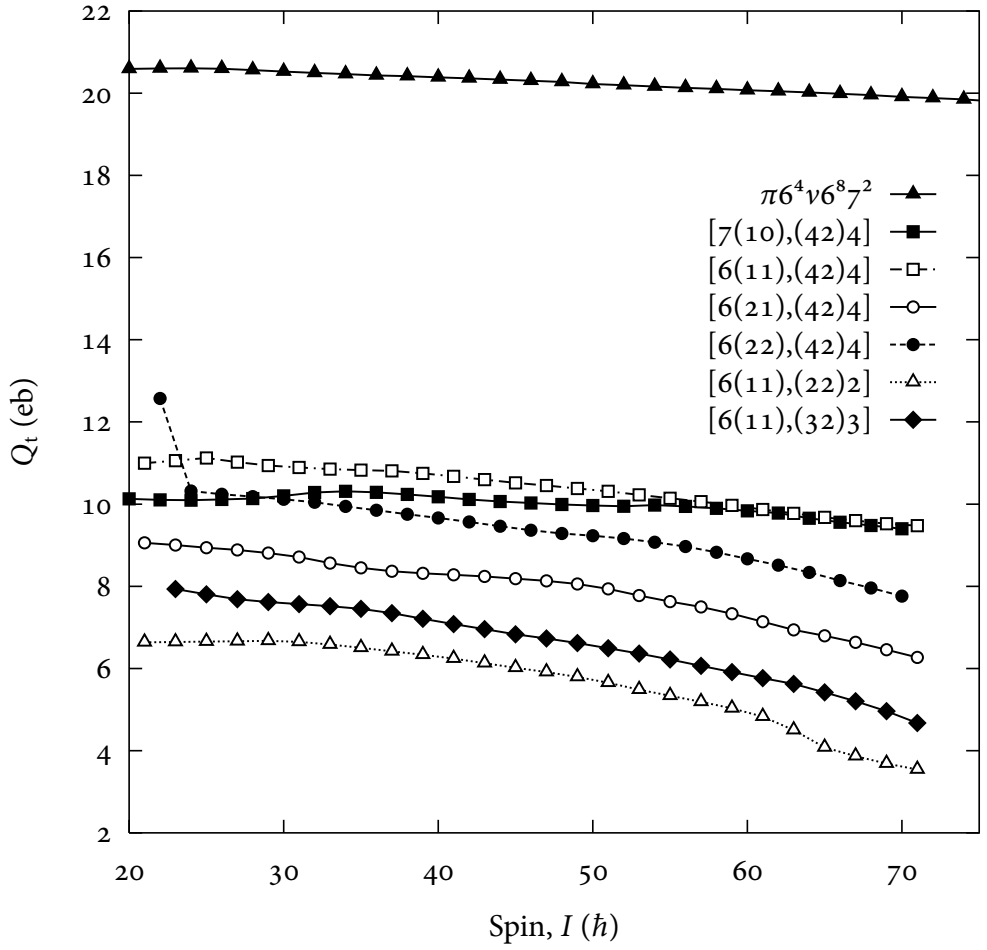

Figure 5.5 Q_t for favoured TSD configurations and one favoured SD configuration for ^{154}Er as a function of spin, calculated from the deformation values predicted by CNS calculations (Fig. 5.8) using Eqs. 2.27 and 2.28.

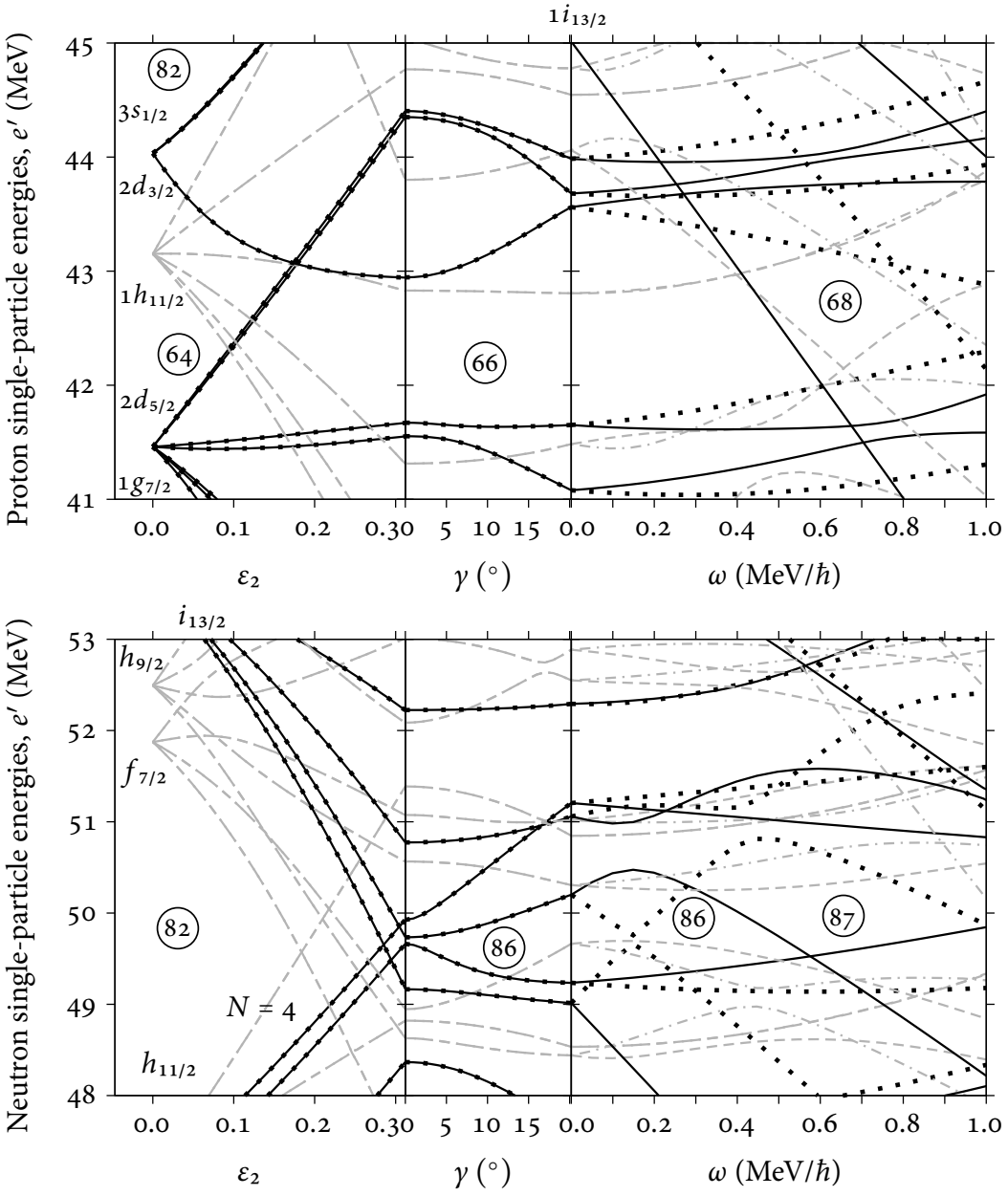

Figure 5.6 The evolution of proton and neutron single-particle orbitals around $Z = 68$ and $N = 86$ as ε (left panel), γ (centre panel) and ω (right panel) are raised from zero to values corresponding to the positive-γ TSD minimum in Fig. 5.1 ($\varepsilon_2 = 0.312$, $\gamma = 20.2°$, $\varepsilon_4 = 0.016$). Solid lines indicate $(\pi, \alpha) = (+, \frac{1}{2})$, dotted $(+, -\frac{1}{2})$, dashed $(-, \frac{1}{2})$ and dotted-dashed $(-, -\frac{1}{2})$.

5.2.2 Band 1 (TSD)

Fig. 5.6 shows proton and neutron single-particle diagrams for the positive-γ minimum, with $\varepsilon_2 = 0.312$, $\gamma = 20.2^\circ$ and $\varepsilon_4 = 0.016$. The trends observed in these diagrams are representative of both TSD minima. The TSD configurations can be considered as particles outside a $^{146}_{64}\mathrm{Gd}_{82}$ closed core.[1] At $Z = 68$ and low ω, four pairs of $h_{11/2}$ orbitals are filled. As ω increases, strongly down-sloping $f_{7/2}$ and $i_{13/2}$ orbitals go below Fermi surface, while a pair of $h_{11/2}$ orbitals rises above it, and a gap appears at $Z = 68$.

For neutrons at $N = 86$, up-sloping $h_{11/2}$ and $N = 4$ orbitals increase in energy as ε_2 is increased, to the point where they cross the Fermi surface, while the lowest down-sloping $i_{13/2}$ orbitals go beneath it. Hence favoured configurations in ^{154}Er are of the form

$$\pi(h_{11/2})^{p_1}(h_{9/2}f_{7/2})^{p_2}(i_{13/2})^{p_3} \otimes \nu(N=4)^{-n_1}(h_{11/2})^{-n_2}(i_{13/2})^{n_3},$$

where p is the number of protons and n the number of neutrons (or neutron holes) in the orbitals indicated relative to the ^{146}Gd core. These configurations are denoted $[p_1(p_2p_3), (n_1n_2)n_3]$ in this thesis.

The dynamic moment of inertia of band 1 (Fig. 5.3) lies very close to that of band 3 in ^{152}Dy [88]. This has been proposed to be a TSD band based on its $\mathcal{J}^{(2)}$ moment of inertia of 70 to 78 $\hbar^2$/MeV in the 0.45–0.65 MeV/$\hbar$ frequency range [89], which is close in magnitude to the $\mathcal{J}^{(2)}$ of the TSD bands in ^{163,164,165}Lu [6, 90].

At $\hbar\omega = 0.55$–0.60 MeV, the $\mathcal{J}^{(2)}$ of band 1 (and that of the ^{152}Dy TSD band) ex-

[1] An appreciable shell gap has been shown to exist at $Z = 64$ in addition to the magic numbers listed in Chapter 2 [87].

periences a slight rise, consistent with the positive-signature $\nu[651]\frac{3}{2}$ orbital falling below the Fermi surface at the same frequency, supplanting the positive-signature $[400]\frac{1}{2}$ orbital. This rise is followed by a sudden discontinuity not seen in the ^{152}Dy band, with no obvious explanation. A disadvantage of using $\mathcal{J}^{(2)}$ is that it can be *too* sensitive to the measured transition energy, showing irregularities when energies cannot be measured precisely. However, for $\mathcal{J}^{(2)}$ to be smooth at this frequency, the 1300 keV transition would have to be approximately 3 keV lower than measured, well outside the ±0.4 keV uncertainty.

A key feature of the triaxial bands in $^{163-165}$Lu is believed to be the occupation of the $\pi i_{13/2}$ subshell, as with the SD band, and indeed this is a feature of several of the favoured configurations resulting from CNS calculations. The energies of four candidate TSD configurations [77], minus a rotating liquid drop reference, are shown in Fig. 5.7. These are compared with the energies of band 1 assuming a spin appropriate to the configuration (using arguments similar to those applied to band 2 in the previous section).

The [6(21),(42)4] configuration is the lowest in energy over the whole spin range, although it competes with [7(10),(42)4] if only the experimental spin ranges are considered. However, as can be seen from Fig. 5.7 (bottom panel), [6(21),(42)4] is in better agreement with the experimental energies. The next best agreement is for [6(22),(42)4], but this configuration is predicted to be relatively high in energy.

In terms of the implied bandhead spin of these configurations, the addition of each proton to the $h_{9/2}f_{7/2}$ and $i_{13/2}$ orbitals adds 2–3 $\hbar$ of alignment, and so the bandhead spin, I_0, increases from 22 for [7(10),(42)4] to 30 for [6(22),(42)4]. The best agreement with experiment is for [6(11),(42)4] with I_0 = 25. When evaluating the theoretical configurations based on spin values, we should remind ourselves

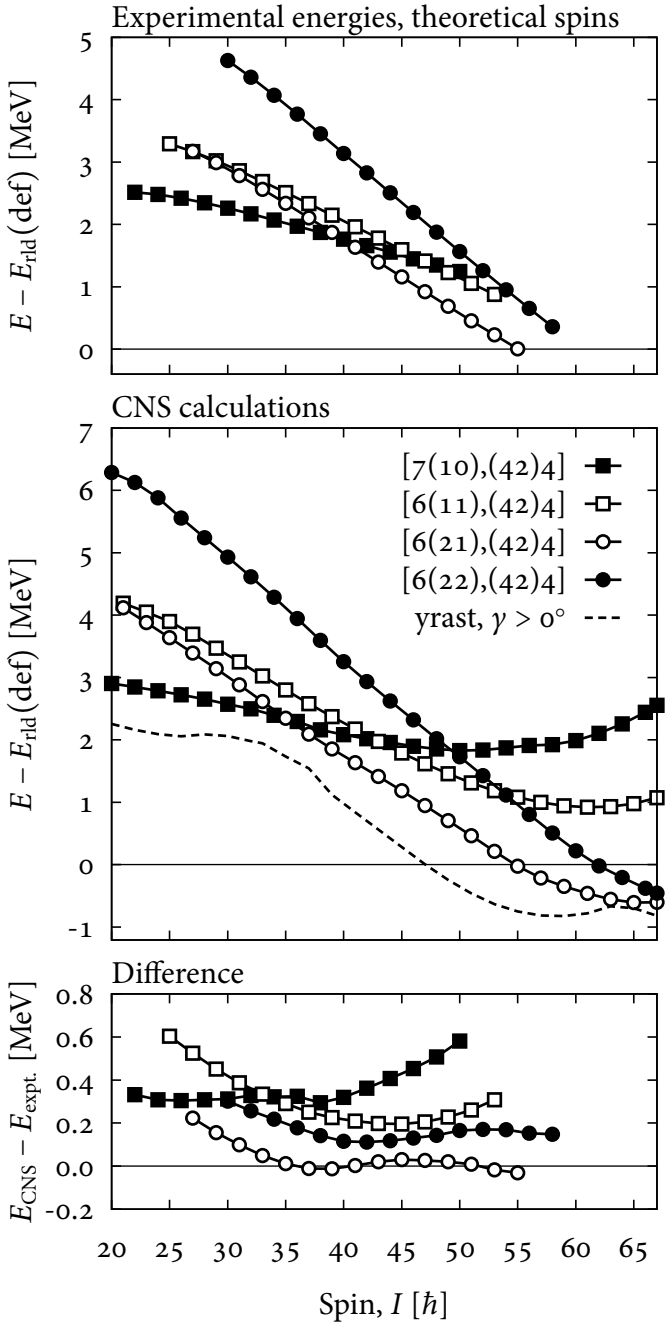

Figure 5.7 Comparison of experimental and theoretical level energies minus a rotating liquid-drop energy ($E_{\rm rld}$) as a function of spin for band 1. (Top panel) The dashed line labelled 'yrast, $\gamma > 0°$' corresponds to the lowest energy, independent of signature and parity, for the $\gamma \sim 15°$–$30°$, $\varepsilon_2 \sim 0.3$–0.4 minimum shown in Fig. 5.1.

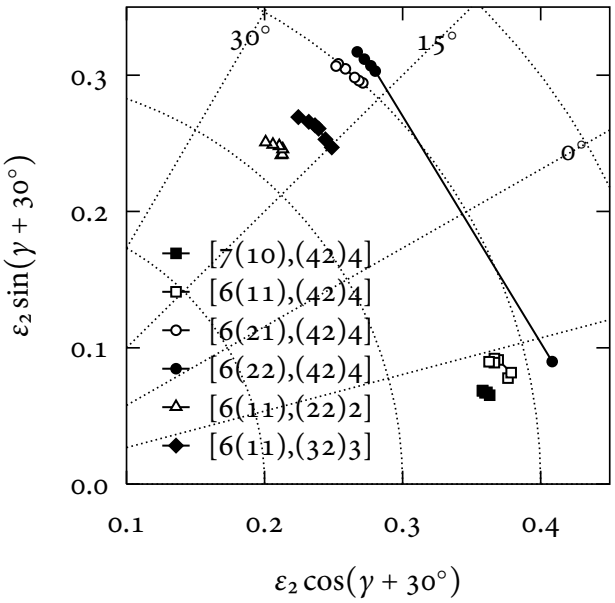

Figure 5.8 Theoretical deformation values of candidate TSD configurations over a range of spins in ^{154}Er, as predicted by CNS calculations. [6(22),(42)4] has a single TSD2 point at lower spin ($\sim 22\,\hbar$).

that the linking transitions between the bands and the ND level scheme have not been observed and the true spin may be significantly higher than our estimates.

Fig. 5.8 shows the location of these configurations in deformation space, together with two more configurations that are generally lower in energy but have low Q_t. The Q_t of the configurations as a function of spin is shown in Fig. 5.5. As we predicted from Eq. 2.28, configurations originating from TSD2 have larger Q_t than those from TSD1, with [6(11),(42)4] having $Q_t \approx 10.7$ eb and [7(10),(42)4] having $Q_t \approx 10.2$ eb, both consistent with the measured Q_t of 11.0 ± 0.6 eb. The TSD1 configurations, on the other hand, have lower Q_t. For [6(22),(42)4], $Q_t \approx 9.7$ eb while [6(21),(42)4] has $Q_t \approx 8.3$ eb, both inconsistent with our result.

Finally, the theoretical $\mathcal{J}^{(2)}$ moment of inertia for the four strongest-candidate

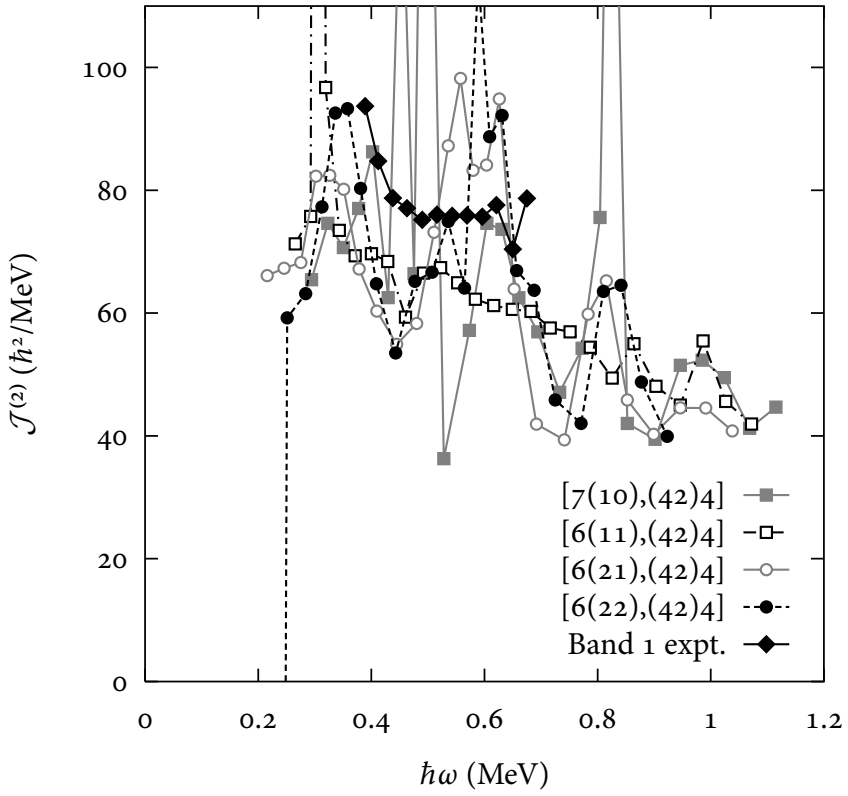

Figure 5.9 Theoretical $\mathcal{J}^{(2)}$ moment of inertia for candidate configurations in ^{154}Er compared with the experimental data for band 1.

configurations are shown in Fig. 5.9, compared with the experimental value. The behaviour of all configurations except [6(11),(42)4] is rather erratic, although they fluctuate around a value close to the experimental one. Conversely, the [6(11),(42)4] configuration varies smoothly and follows the same downward trend as the experimental value, but is ~ 10 $\hbar^2$/MeV too low.

The properties of the four configurations are summarised in Table 5.1. Overall, each configuration has a feature that prevents it from being assigned definitively to band 1. However, the measured Q_t suggests the band belongs to the negative-γ minimum – a puzzling result considering its energetically unfavoured nature.

Configuration	TSD minimum	Q_t (eb)	I_0	$\overline{E}_{CNS} - \overline{E}_{yrast}$ (MeV)	$\overline{E}_{CNS} - \overline{E}_{expt.}$ (MeV)
[7(10),(42)4]	TSD2	10.2	22	1.0	0.36
[6(11),(42)4]	TSD2	10.7	25	1.5	0.31
[6(21),(42)4]	TSD1	8.3	27	0.9	0.04
[6(22),(42)4]	TSD1	9.7	30	2.1	0.17

Table 5.1 Summary of the favoured TSD configurations from CNS calculations. $\overline{E}_{CNS} - \overline{E}_{yrast}$ and $\overline{E}_{CNS} - \overline{E}_{expt.}$ are the average difference between the theoretical energies and, respectively, the yrast band energy and the experimental band 1 energy over the spin range $I_0 + 28$, with I_0 taking the same values as in Fig. 5.7.

5.2.3 Band 3

The measured Q_t of 10 eb suggests that this is a TSD band. The slightly lower value than for band 1 is mirrored by a slightly lower $\mathcal{J}^{(2)}$ moment of inertia. We therefore expect band 3 to belong to one of the remaining favoured TSD configurations given in the previous section. A possible scenario, then, is that band 1 belongs to the [6(11),(42)4] configuration with the higher Q_t, while band 3 belongs to the [7(10),(42)4], with a proton in an $h_{11/2}$ orbital rather than an $i_{13/2}$. However, the latter configuration is generally closer to the yrast line in the spin range considered (Fig. 5.7), contradicting the observed relative intensities of the two bands.

5.2.4 Band 4

The $\mathcal{J}^{(2)}$ moment of inertia of this band is considerably lower than either the SD or TSD bands. As such, it may be a moderately deformed 'TD' (triaxial deformed) band like those observed in ^{152}Dy and ^{153}Ho [89, 91]. Indeed, the $\mathcal{J}^{(2)}$ of the ^{153}Ho TD1 band shown in Fig. 5.3 is very close to that of band 4. The $\mathcal{J}^{(2)}$ of TD1 and TD2 in ^{152}Dy are also close in magnitude, although the former shows a gradual

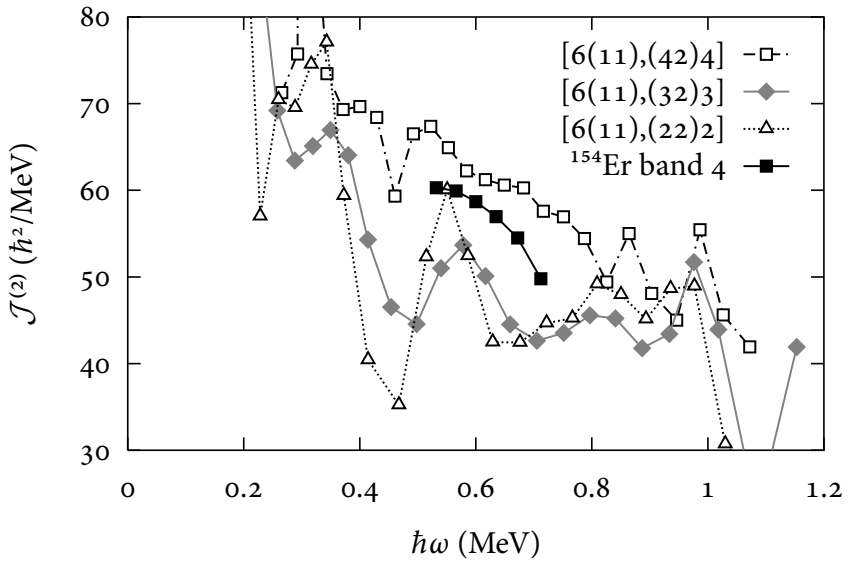

Figure 5.10 The dynamic moment of inertia of band 4 compared with three theoretical configurations.

upward trend and the latter a sudden rise above 0.6 /MeV/$\hbar$, contrary to the gradual decrease observed for band 4.

These bands are believed to be associated with the occupation of only two deformation-driving $i_{13/2}$ orbitals [89], two lower than our favoured TSD configurations and consistent with a lower deformation. Fig. 5.10 compares the $\mathcal{J}^{(2)}$ moment of inertia of band 4 with that of a favoured TSD configuration and similar positive-γ configurations with fewer $i_{13/2}$ neutrons and $N = 4$ holes. We see that the experimental value is intermediate between the two sets of theoretical values. It therefore seems reasonable to suggest that the band 4 configuration is intermediate also, for example [6(11),(42)3].

5.3 Alternative models

We finish by discussing recently published work that attempts to reconcile the large quadrupole moments of the ^{158}Er TSD bands with theory using alternatives to the CNS model. The results can equally be applied to ^{154}Er, with the exception that ^{154}Er does not appear to have a TSD3 minimum.

5.3.1 CRMF

Afanasjev et al. have recenly performed Cranked Relativistic Mean-Field (CRMF) calculations for ^{158}Er [92] in an attempt to explain the large Q_t values observed. These calculations predict positive- and negative-γ TSD configurations analogous to TSD1 and TSD2, although with lower γ deformations of $\pm 10°$, as well as TSD3 configurations with $\gamma \sim 13°$ and near-prolate configurations with $|\gamma| \leq 6°$.

As with CNS calculations, TSD1 configurations have $Q_t \leq 9$ eb and are generally calculated to be lower in energy than TSD2 configurations, but TSD2 is found to compete in energy with TSD1 for certain parameterisations of the theoretical potential.

Overall, the TSD3 configurations, predicted to compete in energy at higher spins, are the favoured interpretation for the ^{158}Er bands, with Q_t values of ~ 11 eb. However, as with the CNS calculations for ^{154}Er, the TSD3 assignment necessitates a much higher spin assignment than is estimated experimentally, with one configuration requiring the highest-spin state to be at $77\,\hbar$ – the highest spin ever recorded.

5.3.2 Tilted-axis cranking

It was mentioned at the beginning of this chapter that we would intuitively expect a classical spinning top with negative γ to be unstable. Using the parameters ε_2 and γ, one is limited to shapes with their rotation axes corresponding to one of their three principle axes and so the possibility that the negative-γ shape might 'tilt over' to positive γ is not addressed. The tilted-axis cranking method [93], on the other hand, permits a reorientation of the rotational axis, allowing the stability of the nuclear shape with regard to such reorientations to be investigated. This method has recently been applied to ^{158}Er by Shi et al. [94].

Using the tilted-axis approach, an increase in γ from its TSD2 value ($-15°$) to its TSD1 value ($22°$) (effectively 'squashing' the nucleus from one to the other), results in two energy minima around these values, just as in the conventional CNS calculations. However, when the magnitude of γ is fixed and the rotational axis allowed to *tilt* from negative to positive γ, a continuous decrease in energy is observed, and so TSD2 is found to be a saddle point rather than a minimum. Thus, according to these calculations, a negative-γ TSD shape is unstable to a reorientation of the rotational axis and would not be observed experimentally.

While configurations with high Q_t (~ 10.5 eb) have been proposed by Shi et al., they are calculated to be significantly higher in energy than lower-Q_t configurations with $Q_t \approx 7.5$ eb. Hence, the Q_t values of ~ 11 eb in ^{157,158}Er and now ^{154}Er are not sufficiently accounted for by the titled-axis method.

Conclusion

We have succeeded in measuring the quadrupole moments of the SD and TSD band in ^{154}Er, together with a tentative value for a third, newly discovered band. A fourth, new band has also been observed with a moment of inertia consistent with a TSD band.

The quadrupole moment of 19.5 eb for the SD band is consistent with theoretical predictions, validating the Doppler-shift attenuation method used to measure the quadrupole moments of the TSD bands in ^{154}Er, as well as those in ^{157,158}Er.

The quadrupole moments of the TSD bands in all three of these nuclei have values of ~ 11 eb. In ^{154}Er, this is consistent with a triaxial shape rotating around its intermediate axis rather than around its short axis as favoured by theoretical predictions. This is also the case with ^{157,158}Er, with configurations from the a more highly deformed, but theoretically unfavoured, positive-γ TSD minimum also being candidates.

However, we should not overlook the fact a number of modifications to the analysis procedure were necessary to produce satisfactory results. Even after these modifications, some problems remain, notably the fact that many $F(\tau)$ points deviate significantly from the fitted Q_t curve. This highlights the difficulty of using the DSAM, which relies on the assumption that the theoretical stopping power of

the target material is correct. We therefore suggest that future experiments using the DSAM, especially those looking at very weakly populated bands, devote some beam time to measuring the stopping power of the target material.

Nevertheless, our results deepen the mystery of the unexpectedly high quadrupole moments measured in erbium TSD bands and show that there is still much to be understood about the structure of nuclei in the ultrahigh-spin regime. Further experiments - or new theoretical developments - will provide the answers, and indeed results are currently being analysed of a DSAM experiment performed by our collaboration to measure the quadrupole moment of the candidate TSD band in ^{160}Yb, which has two more protons than ^{158}Er.

Bibliography

[1] S. M. Polikanov et al., Soviet Physics, JETP **16**, 1016 (1962).

[2] B. M. Nyakó et al., Physical Review Letters **52**, 507 (1984).

[3] A. Bohr and B. R. Mottelson, *Nuclear Structure Volume II: Nuclear Deformations*, World Scientific Publishing Co. Pte. Ltd., Singapore, 1998.

[4] S. W. Ødegård et al., Physical Review Letters **86**, 5866 (2001).

[5] P. Bringel et al., The European Physical Journal A **16**, 155 (2003).

[6] S. Törmänen et al., Physics Letters B **454**, 8 (1999).

[7] G. Schönwaßer et al., Physics Letters B **552**, 9 (2003).

[8] C. X. Yang et al., The European Physical Journal A **1**, 237 (1998).

[9] H. Amro et al., Physics Letters B **506**, 39 (2001).

[10] A. Neußer et al., The European Physical Journal A **15**, 439 (2002).

[11] M. K. Djongolov et al., Physics Letters B **560**, 24 (2003).

[12] A. Aguilar et al., Physical Review C **77**, 1 (2008).

[13] C. Teal et al., Physical Review C **78**, 3 (2008).

[14] N. S. Pattabiraman et al., Physics Letters B **647**, 243 (2007).

[15] K. Lagergren et al., Physical Review Letters **87**, 1 (2001).

[16] E. S. Paul et al., Physical Review Letters **98**, 5 (2007).

[17] J. Ollier et al., Physical Review C **80**, 1 (2009).

[18] X. Wang et al., Physics Letters B **702**, 127 (2011).

[19] C. Schück, M. A. Deleplanque, R. M. Diamond, F. S. Stephens, and J. Dudek, Nuclear Physics A **496**, 385 (1989).

[20] L. A. Bernstein et al., Physical Review C **52**, 1171 (1995).

[21] S. G. Nilsson and I. Ragnarsson, *Shapes and shells in nuclear structure*, Cambridge University Press, Cambridge, 1995.

[22] R. Bengtsson, J. Dudek, W. Nazarewicz, and P. Olanders, Physica Scripta **39**, 196 (1989).

[23] R. F. Casten, *Nuclear Structure from a Simple Perspective*, Oxford Studies in Nuclear Physics, Oxford University Press, New York, 2nd edition, 2000.

[24] T. Bengtsson, Nuclear Physics A **512**, 124 (1990).

[25] S. G. Nilsson et al., Nuclear Physics A **31**, 1 (1969).

[26] R. B. Firestone, *Table of Isotopes Volume II*, Wiley-Inerscience, New York, 8th edition, 1996.

[27] G. Andersson et al., Nuclear Physics A **268**, 205 (1976).

[28] S. E. Larsson, I. Ragnarsson, and S. G. Nilsson, Physics Letters B **38**, 269 (1972).

[29] R. Bengtsson et al., Physics Letters B **57**, 301 (1975).

[30] A. V. Afanasjev and P. Ring, Nuclear Physics A **654**, 647c (1999).

[31] V. M. Strutinsky, Nuclear Physics A **95**, 420 (1967).

[32] I. Ragnarsson, Physics Letters B **264**, 5 (1991).

[33] M. A. Deleplanque, Nuclear Physics A **421**, 339 (1984).

[34] A. Bohr and B. R. Mottelson, *Nuclear Structure Volume I: Single-Particle Motion*, World Scientific Publishing Co. Pte. Ltd., Singapore, 1998.

[35] A. G. Smith et al., Journal of Physics G: Nuclear and Particle Physics **28**, 2307 (2002).

[36] K. Schiffer and B. Herskind, Nuclear Physics A **520**, c521 (1990).

[37] H. Ejiri and M. J. A. de Voigt, *Gamma-Ray and Electron Spectroscopy in Nuclear Physics*, Oxford University Press, New York, 1989.

[38] S. Cohen, F. Plasil, and W. Swiatecki, Annals of Physics **82**, 557 (1974).

[39] D. L. Hillis et al., Nuclear Physics A **325**, 216 (1979).

[40] T. Lauritsen et al., Physical Review C **62**, 1 (2000).

[41] A. Gavron, Physical Review C **21**, 230 (1980).

[42] I. Y. Lee, Nuclear Physics A **520**, c641 (1990).

[43] I. Y. Lee, Progress in Particle and Nuclear Physics **38**, 65 (1997).

[44] C. Beausang and J. Simpson, Journal of Physics G: Nuclear and Particle Physics **22**, 527 (1996).

[45] J. Cresswell and J. Sampson, *MTsort Language - EDOC033*, 2009.

[46] J. Cresswell, *EDOC073 - Event Format [Sorting + Storage]*, 2001.

[47] C. W. Beausang et al., Nuclear Instruments and Methods in Physics Research Section A **364**, 560 (1995).

[48] D. C. Radford, Notes on the use of the program gf3, 2000, `http://radware.phy.ornl.gov/gf3`.

[49] J. R. Taylor, *An introduction to error analysis: the study of uncertainties in physical measurements*, University Science Books, Sausalito, California, 2nd edition, 1997.

[50] P. R. Bevington and D. K. Robinson, *Data Reduction and Error Analysis*, McGraw-Hill, New York, 3rd edition, 2003.

[51] M. S. Caceci, Analytical Chemistry **61**, 2324 (1989).

[52] B. Efron and G. Gong, The American Statistician **37**, 36 (1983).

[53] J. F. Ziegler, J. P. Biersack, and U. Littmark, *The Stopping and Range of Ions in Solids*, Pergamon, New York, 1985.

[54] W. Benenson, J. W. Harris, H. Stocker, and H. Lutz, *Handbook of Physics*, Springer + Business Media, New York, 2006.

[55] E. Moore, private communication.

[56] F. James and M. Winkler, *MINUIT User's Guide*, 2004.

[57] H. Savajols et al., Physical Review Letters **76**, 4480 (1996).

[58] E. Moore, D. Nisius, and R. Janssens, *Lifetime measurements and identical SD bands in the A= 190 and A= 150 regions*, 1996.

[59] X. Wang et al., Physical Review C **75**, 1 (2007).

[60] M. A. Bentley et al., Journal of Physics G: Nuclear and Particle Physics **17**, 481 (1991).

[61] D. Nisius et al., Physics Letters B **392**, 18 (1997).

[62] E. F. Moore et al., Physical Review C **55**, R2150 (1997).

[63] E. F. Moore et al., Zeitschrift für Physik A **358**, 219 (1997).

[64] R. Krücken et al., The European Physical Journal A **5**, 367 (1999).

[65] G. Gürdal et al., Journal of Physics G: Nuclear and Particle Physics **31**, S1873 (2005).

[66] D. J. Hartley et al., Physics Letters B **608**, 31 (2005).

[67] D. Roßbach et al., Physical Review C **66**, 1 (2002).

[68] E. S. Paul et al., Journal of Physics G: Nuclear and Particle Physics **18**, 121 (1992).

[69] R. M. Diamond et al., Physical Review C **41**, 1327 (1990).

[70] M. A. Riley et al., Acta Physica Polonica B **32**, 2683 (2001).

[71] G. Schönwaßer et al., The European Physical Journal A **15**, 435 (2002).

[72] C. A. Ur et al., Physical Review C **60**, 1 (1999).

[73] E. O. Lieder et al., Nuclear Instruments and Methods in Physics Research Section A **607**, 591 (2009).

[74] D. C. Radford, Nuclear Instruments and Methods in Physics Research Section A **361**, 297 (1995).

[75] D. C. Radford, M. Cromaz, and C. J. Beyer, Analysis of high-fold gamma data, in *AIP Conference Proceedings*, edited by C. Baktash, pages 570–580, Aip, 1999.

[76] D. C. Radford, Band-search in levit8r, 1998, `http://radware.phy.ornl.gov/sdb_search.html`.

[77] I. Ragnarsson, private communication.

[78] C. G. Andersson et al., Physica Scripta **24**, 266 (1981).

[79] F. A. Beck et al., Zeitschrift für Physik A Atoms and Nuclei **319**, 119 (1984).

[80] B. Nyakó et al., Physical Review Letters **56**, 23 (1986).

[81] B. Singh, R. Zywina, and R. B. Firestone, Nuclear Data Sheets **97**, 241 (2002).

[82] T. Lauritsen et al., Physical Review Letters **88**, 042501 (2002).

[83] T. Bengtsson, I. Ragnarsson, and S. Åberg, Physics Letters B **208**, 39 (1988).

[84] D. E. Appelbe et al., Physical Review C **56**, 2490 (1997).

[85] W. Satuła, J. Dobaczewski, J. Dudek, and W. Nazarewicz, Physical Review Letters **77**, 5182 (1996).

[86] P. J. Twin et al., Physical Review Letters **57**, 811 (1986).

[87] P. Kleinheinz et al., Zeitschrift für Physik A **290**, 279 (1979).

[88] P. J. Dagnall et al., Physics Letters B **335**, 313 (1994).

[89] D. E. Appelbe et al., Physical Review C **66**, 1 (2002).

[90] H. Schnack-Petersen et al., Nuclear Physics A **594**, 175 (1995).

[91] M. B. Smith et al., Physical Review C **61**, 034314 (2000).

[92] A. V. Afanasjev, Y. Shi, and W. Nazarewicz, Physical Review C **86**, 031304(R) (2012).

[93] S. Frauendorf, Nuclear Physics A **557**, 259 (1993).

[94] Y. Shi et al., Physical Review Letters **108**, 1 (2012).